

AFIT/GE/ENG/99M-04

TE SCATTERING FROM BUBBLES IN RAM

THESIS

JOHN G. COCHRAN, BEE
CAPTAIN, USAF

AFIT/GE/ENG/99M-04

1 19990413 069 3

Approved for public release; distribution unlimited

The views expressed in this thesis are those of the author and do not reflect the official policy or position of the Department of Defense or the United States Government.

AFIT/GE/ENG/99M-04

TE Scattering From Bubbles In RAM

THESIS

Presented to the Faculty of the School of Engineering
of the Air Force Institute of Technology

Air University

In Partial Fulfillment of the
Requirements for the Degree of
Master of Science in Electrical Engineering

John G. Cochran, BEE

Captain, USAF

March, 1999


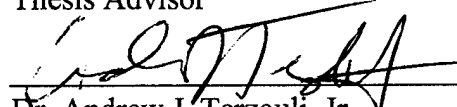
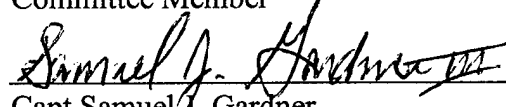
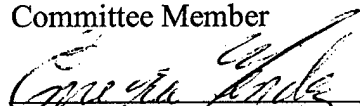
Approved for public release; distribution unlimited

TE Scattering From Bubbles In RAM

John G. Cochran

Captain, USAF

Approved:

 Maj. Peter J. Collins (PhD) Thesis Advisor	<u>10 MAR 99</u> Date
 Dr. Andrew J. Terzouli, Jr. Committee Member	<u>10 Mar 99</u> Date
 Capt Samuel J. Gardner Committee Member	<u>10 MAR 99</u> Date
 Mr. Enrique Mendez Committee Member	<u>10 MAR 99</u> Date

Acknowledgements

There are so many people I need to thank for their help in accomplishing this thesis. First and foremost, I want to thank my parents and grandparents whose constant love and encouragement has permitted me to complete this endeavor. All of my past and future accomplishment are dedicated to them.

Special thanks are necessary for my thesis advisor Maj Pete Collins for his patience and guidance, my sponsor Mr. Enrique Mendez, and committee members Dr. Andy Terzouli and Capt Sam Gardner.

Others who deserve thanks and recognition are my fellow Low Observable's (LO) classmates. Matt Craig, Art Ford, Bob Eigel and Karl Schloer have helped me every step of the way, not only in my thesis research but also in all the related course work. Without them, I never would have made it.

Now it's time to go tee it up!

J. Grayson Cochran

ACKNOWLEDGEMENTS.....	III
LIST OF FIGURES	VI
LIST OF TABLES	VIII
ABSTRACT.....	IX
CHAPTER 1 INTRODUCTION	1-1
1.1 MOTIVATION.....	1-1
1.2 PROBLEM STATEMENT	1-2
1.3 SCOPE	1-3
1.4 APPROACH.....	1-3
1.5 DOCUMENT ROADMAP	1-4
CHAPTER 2 BACKGROUND THEORY.....	2-1
2.1 INTRODUCTION	2-1
2.2 RELATED WORK	2-2
2.3 RADAR ABSORBING MATERIAL (RAM).....	2-5
2.4 MATERIAL CHARACTERIZATION MEASUREMENTS.....	2-7
2.5 RADAR CROSS SECTION FUNDAMENTALS AND MEASUREMENT	2-9
2.6 RADAR IMAGING FUNDAMENTALS.....	2-12
2.7 LINEAR REGRESSION ANALYSIS.....	2-14
2.7.1 <i>Least Squares Estimation (LSE)</i>	2-15
2.7.2 <i>Model Adequacy Checking</i>	2-15
2.7.3 <i>Confidence Intervals</i>	2-23
2.7.4 <i>Model Validation</i>	2-26
2.8 RCS SIMULATION SOFTWARE.....	2-26
2.9 SUMMARY	2-29
CHAPTER 3 METHODOLOGY	3-1
3.1 INTRODUCTION	3-1
3.2 RAM CHARACTERIZATION	3-1
3.2.1 <i>Equipment</i>	3-2
3.2.2 <i>Procedures</i>	3-3
3.2.3 <i>Data</i>	3-4
3.2.4 <i>Uncertainty</i>	3-4
3.3 RCS MEASUREMENTS	3-8
3.3.1 <i>Equipment</i>	3-8
3.3.2 <i>Procedures</i>	3-11
3.3.3 <i>Data</i>	3-18
3.3.4 <i>Uncertainty</i>	3-20
3.4 JRMBOR RCS SIMULATIONS	3-21
3.4.1 <i>Procedures</i>	3-21
3.4.2 <i>Data</i>	3-24
3.5 XPATCHF RCS SIMULATIONS.....	3-24
3.5.1 <i>Procedures</i>	3-24
3.5.2 <i>Data</i>	3-25
3.5.3 <i>Assumptions</i>	3-25
3.6 SUMMARY	3-25
CHAPTER 4 ANALYSIS AND APPLICATIONS	4-1
4.1 INTRODUCTION	4-1
4.2 RAM ANALYSIS	4-1
4.3 RCS ANALYSIS OF MEASURED DATA.....	4-4

4.4 RCS ANALYSIS OF SIMULATED DATA	4-12
4.5 THE PREDICTION EQUATION	4-13
4.6 BUBBLE EFFECTS ON A LOW RCS TARGET	4-29
4.7 SUMMARY	4-36
CHAPTER 5 CONCLUSIONS AND RECOMMENDATIONS.....	5-1
5.1 CONCLUSIONS.....	5-1
5.2 RECOMMENDATIONS	5-2
APPENDIX A.....	A-1
APPENDIX B	B-1
APPENDIX C	C-1
BIBLIOGRAPHY	BIB-1
VITA.....	VITA-1

List of Figures

FIGURE 2-1 NORMAL PROBABILITY PLOTS (A) IDEAL (B) HEAVY-TAILED (C) LIGHT-TAILED (D) POSITIVE SKEW (E) NEGATIVE SKEW	2-18
FIGURE 2-2 PATTERNS FOR RESIDUAL PLOTS (A) SATISFACTORY (B) FUNNEL (C) DOUBLE BOW (D) NONLINEAR.....	2-19
FIGURE 2-3 PLOT OF MSE(P) VERSUS P	2-22
FIGURE 3-1 FOCUSED BEAM ASSEMBLY.....	3-2
FIGURE 3-2 S-PARAMETER DEFINITION FOR A TWO-PORT NETWORK	3-3
FIGURE 3-3 MEASURED RELATIVE PERMITTIVITY	3-5
FIGURE 3-4 MEASURED RELATIVE PERMEABILITY	3-5
FIGURE 3-5 STATED ACCURACY OF THE MAGNITUDE AND PHASE OF HP-8510 S-PARAMETER MEASUREMENTS [10].....	3-6
FIGURE 3-6 AFRL/XPN COMPACT RANGE DESIGN [19].....	3-9
FIGURE 3-7 MRC TESTBODY WITH RAM STRIP.....	3-11
FIGURE 3-8 AN EXAMPLE OF A BUBBLE IN RAM	3-14
FIGURE 3-9 ANOTHER EXAMPLE OF A BUBBLE IN RAM.....	3-14
FIGURE 3-10 PEELED BACK RAM WITH STYROFOAM INSERT	3-15
FIGURE 3-11 DOUBLE CALIBRATION COMPARISON	3-17
FIGURE 3-12 3-D IMAGE PLOT	3-19
FIGURE 3-13 WATERFALL PLOT OF A SINGLE CONFIGURATION	3-20
FIGURE 3-14 JRMBOR TESTBODY GEOMETRY	3-22
FIGURE 4-1 RAM ATTENUATION VERSUS FREQUENCY	4-3
FIGURE 4-2 3-D IMAGE OF RANGE NOISE + CLUTTER.....	4-5
FIGURE 4-3 3-D IMAGE OF CONFIGURATION 1 RUN 2 (4"x8" BUBBLE).....	4-6
FIGURE 4-4 3-D IMAGE OF SCATTERING FROM CUTS IN THE RAM SAMPLE	4-7
FIGURE 4-5 WATERFALL PLOT OF THE VARIOUS CONFIGURATIONS AT 25 DEGREES	4-8
FIGURE 4-6 WATERFALL PLOT OF RANGE NOISE + CLUTTER.....	4-9
FIGURE 4-7 WATERFALL PLOT OF CONFIGURATION 3 RUN 1 (4"x6" BUBBLE).....	4-10
FIGURE 4-8 RCS VERSUS FREQUENCY	4-11
FIGURE 4-9 COMPARISON OF MEASURED RCS AND SIMULATED RCS (JRMBOR).....	4-12
FIGURE 4-10 RESIDUALS VERSUS LOGIT_RCSM PRE-FINAL MODEL	4-18
FIGURE 4-11 RESIDUALS VERSUS LOGIT_RCSM FINAL MODEL	4-18
FIGURE 4-12 HISTOGRAM, QUANTILE, AND OUTLIER, AND NORMAL QUANTILE PLOTS OF THE PRE-FINAL MODEL RESIDUALS, RESPECTIVELY	4-19
FIGURE 4-13 HISTOGRAM, QUANTILE, AND OUTLIER, AND NORMAL QUANTILE PLOTS OF THE FINAL MODEL RESIDUALS, RESPECTIVELY	4-20
FIGURE 4-14 RAM BUBBLE DESIGN POINTS	4-23
FIGURE 4-15 PROPOSED RAM BUBBLE DESIGN POINTS	4-23
FIGURE 4-16 C3R1 (6"x4") COMPARISON OF PREDICTED AND MEASURED RCS	4-24
FIGURE 4-17 C5R1 (5"x4") COMPARISON OF PREDICTED AND MEASURED RCS	4-25
FIGURE 4-18 C1R2 (11"x3.5") COMPARISON OF PREDICTED AND MEASURED RCS	4-26
FIGURE 4-19 PREDICTIVE CAPABILITIES EXAMPLE BY VARYING LENGTHS AND WIDTHS (3°).....	4-28
FIGURE 4-20 PREDICTIVE CAPABILITIES EXAMPLE BY VARYING LENGTHS AND WIDTHS (33°).....	4-29
FIGURE 4-21 COMPARISONS OF THE COHERENT RCS OF AN ALMOND WITH AND WITHOUT BUBBLES	4-30
FIGURE 4-22 COHERENT CHANGES IN dB DUE TO THE BUBBLES.....	4-31
FIGURE 4-23 COMPARISONS OF THE INCOHERENT RCS OF AN ALMOND WITH AND WITHOUT BUBBLES	4-32
FIGURE 4-24 INCOHERENT CHANGES IN dB DUE TO THE BUBBLES.....	4-33
FIGURE 4-25 EFFECT OF A DOMINANT SCATTERER	4-34
FIGURE A-1 CONFIGURATION 1 RUN 1 (4"x 8" BUBBLE).....	A-2
FIGURE A-2 CONFIGURATION 1 RUN 2 (3.5"x 11" BUBBLE).....	A-3
FIGURE A-3 CONFIGURATION 2 RUN 1 (3.5" x 14.5" BUBBLE)	A-4
FIGURE A-4 CONFIGURATION 3 RUN 1 (4" x 6" BUBBLE)	A-5

FIGURE A-5 CONFIGURATION 3 RUN 2 (5" x 7" BUBBLE)	A-6
FIGURE A-6 CONFIGURATION 3 RUN 3 (5" x 7" BUBBLE)	A-7
FIGURE A-7 CONFIGURATION 4 RUN 1 (8" x 8" BUBBLE)	A-8
FIGURE A-8 CONFIGURATION 4 RUN 2 (4" x 16" BUBBLE)	A-9
FIGURE A-9 CONFIGURATION 5 RUN 1 (4" x 5" BUBBLE)	A-10
FIGURE B-1 WATERFALL PLOT OF RANGE NOISE + CLUTTER	B-2
FIGURE B-2 WATERFALL PLOT OF CONFIGURATION 1 RUN 1 (4"x8" BUBBLE)	B-3
FIGURE B-3 WATERFALL PLOT OF CONFIGURATION 1 RUN 2 (3.5"x11" BUBBLE)	B-4
FIGURE B-4 WATERFALL PLOT OF CONFIGURATION 2 RUN 1 (3.5"x14.5" BUBBLE)	B-5
FIGURE B-5 WATERFALL PLOT OF CONFIGURATION 3 RUN 1 (4"x6" BUBBLE)	B-6
FIGURE B-6 WATERFALL PLOT OF CONFIGURATION 3 RUN 2 (5"x7" BUBBLE)	B-7
FIGURE B-7 WATERFALL PLOT OF CONFIGURATION 3 RUN 3 (5"x7" BUBBLE)	B-8
FIGURE B-8 WATERFALL PLOT OF CONFIGURATION 3 RUN 4 (5"x7" BUBBLE)	B-9
FIGURE B-9 WATERFALL PLOT OF CONFIGURATION 4 RUN 1 (8"x8" BUBBLE)	B-10
FIGURE B-10 WATERFALL PLOT OF CONFIGURATION 4 RUN 2 (4"x16" BUBBLE)	B-11
FIGURE B-11 WATERFALL PLOT OF CONFIGURATION 5 RUN 1 (4"x5" BUBBLE)	B-12
FIGURE C-1 WATERFALL PLOT OF THE VARIOUS CONFIGURATIONS FOR 0 DEGREES	C-2
FIGURE C-2 WATERFALL PLOT OF THE VARIOUS CONFIGURATIONS FOR 5 DEGREES	C-3
FIGURE C-3 WATERFALL PLOT OF THE VARIOUS CONFIGURATIONS FOR 10 DEGREES	C-4
FIGURE C-4 WATERFALL PLOT OF THE VARIOUS CONFIGURATIONS FOR 15 DEGREES	C-5
FIGURE C-5 WATERFALL PLOT OF THE VARIOUS CONFIGURATIONS FOR 20 DEGREES	C-6
FIGURE C-6 WATERFALL PLOT OF THE VARIOUS CONFIGURATIONS FOR 25 DEGREES	C-7
FIGURE C-7 WATERFALL PLOT OF THE VARIOUS CONFIGURATIONS FOR 30 DEGREES	C-8
FIGURE C-8 WATERFALL PLOT OF THE VARIOUS CONFIGURATIONS FOR 35 DEGREES	C-9
FIGURE C-9 WATERFALL PLOT OF THE VARIOUS CONFIGURATIONS FOR 40 DEGREES	C-10
FIGURE C-10 WATERFALL PLOT OF THE VARIOUS CONFIGURATIONS FOR 45 DEGREES	C-11

List of Tables

TABLE 3-1 TEST MATRIX (INCHES).....3-13

TABLE 3-2 COMPACT RANGE UNCERTAINTY.....3-21

TABLE 3-3 REPRESENTATIVE SAMPLE OF JRMBOR DATA3-24

TABLE 3-4 REPRESENTATIVE SAMPLE OF ALMOND DATA.....3-25

TABLE 4-1 PRE-FINAL MODEL.....4-16

TABLE 4-2 FINAL MODEL4-17

TABLE 4-3 SUMMARY OF CHANGE IN DETECTION RANGE.....4-35

Abstract

This research looks at various bubble sizes in one particular magnetic RAM (MAGRAM) type, from grazing incidence (0°) to 45° and at a frequency range from 2-18 GHz, TE polarization. The results from the absolute RCS measurement of the various sized RAM bubbles are discussed in terms of a frequency dependent increase in RCS. In the frequency band of interest, 2 –18GHz, a RAM bubble increases the RCS at all angles, from grazing incidence (0°) to 45° . From 10 -18GHz the RAM bubble does not cause an increase in RCS. In general the highest RCS is at 2GHz and tapers down as frequency increases. At near grazing angles the RCS increase due to the bubbles is 10-15dB. At the higher angles, the RCS increase due to the bubbles is 10-20dB. The RCS increase is relative to the noise plus clutter measurement of the range. The range of absolute RCS values for the various bubble sizes can range from -55 dBsm to -25 dBsm. The results of these experiments are captured in a statistical model which provides an estimate of the bubble's dependence on frequency, angle, and size.

TE Scattering From Bubbles In RAM

Chapter 1 Introduction

1.1 Motivation

Low Observable (LO) or Stealth characteristics are of primary concern in the design and operation of most modern U.S. Air Force weapon systems, particularly aircraft, missiles, and munitions systems. The purpose of employing LO technology in today's Air Force is to drastically reduce the radar, laser, infrared, acoustic and visual detectability of weapon systems. Presently, the chief threat to Air Force systems is from adversaries radar networks. Radars are all weather, long range electromagnetic sensors that constitute the bulk of most adversaries air defenses. Subsequently, the main thrust of LO technology is to exploit electromagnetic phenomena to reduce a system's Radar Cross Section (RCS). There are three primary techniques used to reduce a system's RCS. These techniques are platform shaping, active and passive cancellation, and application of radar absorbing material (RAM) to the exterior of the system.

The relative immaturity of the LO aspects on current operational Air Force systems has lead to unforeseen engineering and logistical challenges. One current challenge of interest is the maintainability of RAM applied to the outer skin of LO systems. Challenges facing RAM maintainers are gaps between sheets of RAM, cracks in RAM, and liquid or air bubbles under RAM. The culprits involved in degrading the RAM are the everyday wear and tear from operational use, improper application of RAM by the maintainer and inadequately designed adhesion and putty systems employed by the materials engineers. The reason why degraded RAM is an important issue is that cracks, gaps and bubbles can cause unintended scattering of radar energy into a weapon system's

important threat sectors, thus increasing the likelihood of detection. Therefore, maintainers must spend time and money to repair the degraded RAM and operators must adjust flight schedules to accommodate the needed maintenance.

In the past, the vast majority of LO research was geared toward RCS reduction through shaping designs and development of the "ideal" RAM. Only recently has the LO community started to attack the electromagnetic scattering problems associated with degraded RAM. The RCS measurement and prediction of degraded RAM poses a difficult problem because individual RCS returns from degraded RAM are usually very small. However, the combined effect of several degraded spots can significantly impact a LO system's observability. Thus, maintainers, engineers and operators can use any knowledge about the consequences that degraded RAM has on the weapon systems RCS. An understanding of degraded RAM is important if maintainers, engineers and operators are to make intelligent repair and force structure decisions; saving time, money and increasing operational readiness.

1.2 Problem Statement

Many Air Force weapons systems fielded today and those planned for tomorrow may have potential problems with degraded RAM. In order for engineers and maintainers to make informed decisions about how degraded RAM increases the system's RCS, it is necessary to measure and model the absolute RCS of degraded RAM. Engineers and maintainers can then use the data from the measurements to establish a database that will aid in the development of effect of defect models for deciding when a repair is needed. The primary goals of this research are to, one, identify the absolute RCS of several RAM bubble geometries, and two, develop an empirical model using

linear regression techniques which the maintainer and engineer can use to determine the effect of the RAM bubbles on an LO system's performance.

1.3 Scope

As the goals of this thesis are to measure the absolute RCS of several bubble geometries and then develop a prediction model, certain limiting assumptions are made. The assumptions include investigating a limited aspect angle range ($0^\circ - 45^\circ$), investigating a limited frequency range (2-18 GHz), and investigating only one type of RAM. These assumptions place certain limitations on the final prediction model. This means the prediction model will only predict the RCS of bubble geometries within the range angles and frequencies and only for the particular RAM type studied. However, this research serves as a model for investigating other angles, frequencies, and RAM types.

1.4 Approach

To accomplish these thesis goals, first the electrical properties of the RAM samples are measured using a focused beam measurement system at Air Force Research Laboratory's Signature Technology office (AFRL/XPN) located on Wright-Patterson AFB, OH. The second step is measuring the absolute RCS of various bubble geometries over the angle and frequency range of interest to develop a database of measurements. For this step AFRL/XPN's compact range facility is utilized. The third step is to use a computer model of the bubbles generated with the Jim Rogers' Monstrous Body of Revolution (JRMBOR) software to generate simulated RCS data. The simulated data is used to compare with the measured data for exploring alternative methods for generating

an RCS database of bubble measurements. The fourth step is to analyze the measured data in the time and frequency domains to characterize the absolute RCS of the RAM bubbles. This data is then used along with linear regression techniques to develop an equation relating the variables of bubble geometry, angle, and frequency to the bubble's RCS. The last step is to use a low RCS object (e.g.-NASA almond) to demonstrate a signature perturbation caused by a bubble and the bubble's impact on the object's radar detection range.

1.5 Document roadmap

This thesis contains five chapters covering the research problem, the necessary theoretical overview, the methodologies for gathering RCS data, an analysis of the data, and conclusions with recommendations for future work. Specifically, Chapter II reviews related work, radar absorbing material, materials measurement, RCS fundamentals and measurement, and radar imaging. Furthermore, Chapter II explains the concepts associated with linear regression and the iterative process of using linear regression to generate a prediction model. It also examines the RCS prediction software used in this research to generate simulated data. Chapter III describes the equipment set up, procedures, test matrix, data examples, and error analysis for the data collections. Chapter IV analyzes the results of the data collected in Chapter III, develops the corresponding linear regression model, and demonstrates the effect of a bubble on a low RCS object's signature. Finally, Chapter V summarizes the results and provides suggestions for future research.

Chapter 2 Background Theory

2.1 Introduction

This chapter describes the theory required to understand the basics of this research effort. The information in each section ties to a specific aspect of this research problem. The first two sections provide the uninitiated reader with necessary background information. The related work section, through the literature review process, ensures that this research is not a duplication of effort. The related work section also provides insight into the scattering due to a small change in surface features. This is important because RAM bubbles represent a class of small changes in surface features. The following section on RAM, is necessary since the research problem studied involves extensive measurement and simulation of surface changes in RAM. Therefore, knowledge of the uniqueness and complexity of RAM is necessary for properly applying the measurement and simulation techniques used to generate data for analysis and processing. The final five sections of Chapter II serve to explain the technical aspects of tools used for generating and processing the RCS data needed to solve the research problem. These tools are material measurements, RCS measurements, radar imaging, linear regression analysis, and RCS simulation software. Note that the order of using these tools is important and demonstrates the interdependence of the tool's input's and output's. For instance, the output data from the material measurements is used to characterize the RAM's attenuation and serves as input for the simulation software. The XpatchF software is used for generating data to demonstrate the signature perturbation due to a bubble. The RCS measurements are input into radar imaging techniques that aid in

classifying the physical mechanisms that generate the RCS return. Finally, the RCS measurements build the database needed as an input to the linear regression process of building a prediction model.

2.2 Related Work

The engineering literature reviewed during this research does not contain any previous examples of work on degraded RAM due to bubbles. However, the literature does contain two categories of work related to small changes in surface features. The first category is the work related to electromagnetic scattering from gaps recessed in Perfect Electric Conductor (PEC) and material coated ground planes. The second category is electromagnetic scattering from hemispheres and “bumps” in ground planes.

Most of the literature in the category of gap scattering deals with gaps recessed in a PEC ground plane. The reason for the emphasis in the literature on PEC gaps is that all weapon systems have requirements for internal access. For example, most modern aircraft retract their wheels on take off. This precipitates the need for landing gear doors. The work of Senior [1,2] concentrates on setting up integral equations, solving for the induced current in the gaps and then using that solution to calculate the scattered fields. The results are then compared with other methods for confirmation. The more interesting work is the numerical and measured results accomplished by Dominek [3]. In his paper, Dominek numerically solves for and measures the RCS of a finite length rectangular gap recessed in a finite sized ground plane. The results are summarized here[3:591]:

Virtually all cracks will generate some form of traveling wave, and look angles and crack dimensions of these traveling waves can play a dominant role in the overall scattering. The traveling wave formulations developed herein provide a means to compute the nature of the phase velocity and the attenuation of the traveling wave in the crack, thus allowing one to predict

the angle at which the wave will radiate and to what extent it will attenuate the crack. The measurements performed demonstrate the accuracy of the solutions as well as the capacity for the traveling wave to be a strong scatter.

On the topic of scattering from gaps recessed in a material coated ground plane, two interesting works were reviewed. In Moore's [4] work, a two dimensional gap is analyzed using a Uniform Theory of Diffraction technique for calculating a diffraction coefficient for the gap. In the work by Ling [5], the scattering from a dielectric coated plate with a gap is measured. The measurements are then analyzed in the time and frequency domains with the intent of describing the scattering mechanisms present. The work goes on to suggest that a time-frequency plot is the best tool for identifying the scattering from a traveling wave in RAM.

Two works from The Ohio State University acquired during the literature review have geometries similar to the geometry of the RAM bubbles. The first work, by Dominek [6], is a report on material parameter measurements but contains an analytic formulation and measured data of a PEC hemisphere on a finite PEC ground plane. The second work, by Ryan [7], is a masters thesis that applies a two dimensional Moment Method solution to four PEC "short bumps" on an infinite PEC ground plane. The "short bumps" are modeled as a half cycle cosine, a full cycle cosine, a rectangular box, and an ellipse.

In [6], a 2" diameter hemisphere is mounted on a finite ground plane and measured from 2-18 GHz, 30° of grazing, and TE polarization. The results have two conclusions. The first point is the measured data matches the analytic formulation. The second point is the peak RCS value is at the lowest frequency and the lowest RCS value is at the highest frequency.

The RCS data in [7] is generated using the Moment Method by varying the length and width of the four bump geometries. The results are best summarized from the conclusion section of the thesis [7: 90-91]:

The magnitude of the backscattered field from a bump is dependent on the shape and specific dimensions of the bump as well as the angle of incidence of the plane wave. For low angles of incidence, the total backscattered field is composed of a diffracted field contribution from the front edge and another diffracted field from the back edge of the bump, and the way in which these contributions combine depends on the shape and dimensions of the bump.

For all bump geometries studied, we find that when the length of the bump is held constant, the echo width increases as the height of the bump increases. When the height of the bump is held constant, the backscattered field is a periodic function of the bump length. In addition, for a constant bump length, the 0° - 90° pattern remains basically the same shape as the height of the bump is varied.

The body of work represented by gap scattering lends some insight into modeling and measuring changes in small surface features. The PEC gaps show that small features have the potential for traveling waves to generate a large RCS return. In addition, the idea of viewing time-frequency plots to analyze the scattering from material coated gaps is suggested. The works on “bumps” and hemispheres also indicate that small changes in surface features can increase RCS. Additionally, the combined works on gaps, “bumps,” and hemispheres indicate increases in RCS are a function of angle, frequency and surface feature size. Therefore, when analyzing the RCS of the measured and simulated data in Chapter IV, angle, frequency, and bubble size are considered as possible driving forces for increasing the RCS.

2.3 Radar Absorbing Material (RAM)

With the explosion in the use of radar systems during World War II, one of the by-products was the investigation of the interaction of radio frequency (RF) waves with various materials. The primary interest in how materials interact with RF waves was the idea of using a specially designed material to absorb the RF waves. The motivation for investigating these materials was the need to absorb RF waves to reduce the interference between a radar and surrounding structures and also an attempt to reduce the detectability of aircraft against threat radars [8].

Today there is great interest in designing RAM for application to weapon systems for reducing the total weapon system's RCS. Ideally, RAM should absorb all wavelengths, at any incidence angle and add no weight. Realistically, RAM design is a trade off among many factors including,

- Level of desired attenuation and in the monostatic or bistatic direction
- Frequency and angle absorption bandwidths
- Specular or nonspecular mechanism reduction
- Desired application such as flat or curved surfaces
- Physical characteristics such as weight and thickness
- Susceptibility to environmental conditions
- Cost
- Ease of manufacture
- Ease of maintenance

RAM is usually applied to areas of a weapon system identified as "hot spots." These areas, usually leading and trailing edges and engine ducts, are where shaping alone

does not adequately reduce the RCS. RAM works by using electrically lossy materials, such as carbon compounds or magnetically lossy materials such as ferrite's, to convert the incident RF energy into heat. The intrinsic material properties engineers manipulate to design RAM are relative permittivity (ϵ_r) and relative permeability (μ_r). Permittivity describes the interaction of a material with an electric field. Permeability describes the interaction of a material with a magnetic field. It is through these properties that the interaction of electromagnetic waves with materials is characterized in terms of reflection, transmission, propagation, and attenuation factors. Additionally, the intrinsic material properties are not constant. The intrinsic properties can change with frequency, temperature, pressure, molecular structure, and are sometimes linear or non-linear, homogeneous or non-homogeneous, isotropic or non-isotropic, lossless or lossy. Mathematically, the material properties are represented by:

$$\epsilon_r = \epsilon'_r + i\epsilon''_r \quad (2.1)$$

$$\mu_r = \mu'_r + i\mu''_r \quad (2.2)$$

where the real part accounts for the energy storage capacity and the imaginary part accounts for the loss component [9].

RAM is classified into two broad categories, Electric RAM (ERAM) and Magnetic RAM (MAGRAM). In weapons system's applications, RAM comes in a thin multilayer ERAM sheet, a thin MAGRAM sheet, or a magnetic paint. For this research project a particular type of thin metal-backed MAGRAM is used that is designed to attenuate the non-specular RCS returns. Non-specular returns are caused by edge and tip diffraction, surface traveling waves, and creeping waves.

2.4 Material Characterization Measurements

The first experimental procedure in this research effort is to generate data by measuring the material properties (ϵ_r and μ_r) of the RAM sample. These measurements are needed to characterize the RAM's ability to attenuate incident RF energy. In addition, the measurements are needed as inputs to the RCS simulation software programs, JRMBOR and XpatchF.

Today scientist and engineers have many different methods for measuring materials intrinsic properties. Three of the most prominent methods are transmission line techniques, admittance tunnels, and free space methods. Transmission line techniques insert small samples into test fixtures that are sections of a transmission line. Knott [9:362] states that transmission line techniques "allow an accurate evaluation of material properties because of the well documented soundness of the theory on which the measurements are based." Precise sample fabrication is the major drawback of transmission line techniques.

An alternative to the transmission line technique is the admittance tunnel. The admittance tunnel allows for measurement of a larger sample and therefore eases sample fabrication requirements. The admittance tunnel is not without its disadvantages. Chief among these is the fact the transmit antenna illuminates the sample holder with a significant portion of its radiated power. This difficulty is addressed by another free space method, the focused beam technique.

However, Shultz points out several advantages of the focused beam technique when compared to the admittance tunnel. The focused beam's advantages are "a smaller minimum sample size, virtual elimination of edge illumination, and utilization from 2-

100 GHz with proper feed horns [10:2].” Additionally, Afsar [11:188] states freespace techniques like “guided techniques, single- or double-pass measurements are suitable for very-high-loss materials (such as RAM).” Therefore, due to the advantages of the focused beam system over the admittance tunnel and the ease of sample fabrication (just cutting the RAM to proper length), the focused beam system was selected for the materials measurements.

The AFRL/XPN focused beam system uses large dielectric lens to focus electromagnetic energy onto a material sample. The beam has a very flat phase front over the sample, while the Gaussian beam profile reduces contamination due to the sample holder. The system uses a Hewlett Packard-8510 network analyzer to measure S-parameter transmission and reflection data. The S-parameter data, S_{11} and S_{21} , are then inserted into the Nicolson-Ross-Weir algorithm that solves for permittivity and permeability [10].

The reflection coefficient (Γ) and the transmission coefficient (T) are related to the S-parameters through the X term.

$$X = \frac{S_{11}^2 - S_{21}^2 + 1}{2S_{11}} \quad (2.3)$$

$$\Gamma = X \pm \sqrt{X^2 - 1} \quad (2.4)$$

$$T = \frac{S_{11} + S_{21} - \Gamma}{1 - (S_{11} + S_{21})\Gamma} \quad (2.5)$$

$$\frac{1}{\Lambda^2} = -\left(\frac{1}{2\Pi t} \ln(T) \right) \quad (2.6)$$

After solving for Γ , T and a third parameter Λ , permeability and permittivity are solved for explicitly.

$$\mu = \frac{2\Pi}{\Lambda\sqrt{k_0^2 - k_c^2}} \left(\frac{1+\Gamma}{1-\Gamma} \right) \quad (2.7)$$

$$\varepsilon = \frac{1}{\mu k_0^2} \left(\frac{4\Pi^2}{\Lambda^2} + k_c^2 \right) \quad (2.8)$$

Where k_c is the cutoff wavenumber and is equal to zero for free-space techniques, t is the thickness, and k_0 is the wavenumber in freespace [10].

2.5 Radar Cross Section Fundamentals and Measurement

The second experimental procedure in the research effort is measuring the RCS of various RAM bubble geometries. The RCS measurements are the primary means of solving the research problem. The RCS data is analyzed for determining the absolute RCS of the bubbles. Furthermore, the RCS measurements develop a database that is used as input for the Linear Regression Analysis process of building an empirical equation for predicting bubbles RCS. Before discussing RCS measurements, the idea of RCS is defined.

Pulsed radars transmit short bursts of radio frequency (RF) wave's that impinge upon targets creating reflected and diffracted waves. A fraction of these reflected and diffracted waves can return to the radar receiver. If this return is strong enough, the radar can obtain range, azimuth and elevation information, therefore allowing the radar to track the target. The target's return or echo is the Radar Cross Section (RCS) and is highly

dependent upon frequency of illumination, range, azimuth, elevation, orientation and target geometry.

Knott [9:64] defines RCS as “a measure of power scattered in a given direction when a target is illuminated by the incident wave and is normalized so the incident wave’s power density at the target does not depend on distance from the target to the radar.” The formal IEEE definition [12] is that RCS is a “measure of the reflective strength of a target defined as 4π times the ratio of the power per unit solid angle scattered in a specified direction to the power per unit area of a plane wave incident on the target from a specified direction.” Mathematically [12]:

$$\sigma = \lim_{r \rightarrow \infty} 4\pi r^2 \left| \frac{\bar{E}_{scattered}}{\bar{E}_{incident}} \right|^2 \quad (2.9)$$

where r is the distance from the radar to the target. $\bar{E}_{scattered}$ and $\bar{E}_{incident}$ are defined later in this section.

An alternative and perhaps more physically motivated definition is that “RCS represents the equivalent aperture surface area of a target that captures a certain amount of power from the incident plane wave and would produce the correct scattered field at the radar receiver if the target radiated the captured power isotropically [13:29].” The reason for discussing these various RCS definitions is to explain that RCS is the figure of merit used for indicating how detectable a target is to a radar system.

The next question is how do engineers actually measure the RCS of a target. For this thesis research, all RCS signature measurements were performed in an indoor chamber called a compact range. The purpose of a compact range is to simulate a uniform plane wave over a very short distance. Simulating a plane wave is accomplished

by bouncing radar waves off a parabolic reflector that creates the desired planar wave front. In order to obtain an accurate measurement, the compact range must meet three criteria. The first criterion is that the incident wave is an infinite plane wave. The second criterion is that the only scattering measured is from the target in free space and not the chamber. The third criterion is that the target is in the far field to eliminate any distance dependencies. RCS engineers use seven methods in an attempt to meet the above criteria [9]:

1. Pyramidal and wedge shaped RAM cover the room to reduce stray energy
2. Vector background subtraction is employed to reduce clutter
3. Specially shaped target mounting pedestals are used to reduce clutter
4. Noise is reduced by pulse integration
5. A reflector system is used to simulate large distances by producing a plane wave
6. Software gating is used to process out target and mounting pedestal interactions
7. Hardware gating is implemented to isolated the scattered field from the target

The final point regarding RCS measurement is that RCS is an indirect measurement. The radar receiver captures reflected power not the actual reflected field. To avoid this problem a comparison method is used. The method compares the measured magnitude and phase of the target to the magnitude and phase of a known target, usually a sphere or cylinder, and coherently subtracts out the range clutter. The resulting

equation for RCS is [13]:

$$\sigma = 4\pi \left| \frac{\bar{E}_{target} - \bar{E}_{targetbackground}}{\bar{E}_{calibration} - \bar{E}_{calibrationbackground}} (\bar{E}_{calibrationexact}) \right|^2 \quad (2.10)$$

The “E” terms in Equations (2.9) and (2.10) refer to an electric or E-field. An E-field is a spatial distribution of time varying electric charge. The fields are represented mathematically in complex number notation or “phasor” notation. An alternative notation is expressing the field values in terms of In-phase (I) and Quadrature (Q) components. The I and Q representation is same as the complex number representation.

2.6 Radar Imaging Fundamentals

Before introducing the topic of radar imaging, it is important to understand different formats engineers use to view RCS data. The RCS data types fall into two classifications: frequency or RCS domain data and time or image domain data. Frequency domain data is primarily useful for viewing global target features (e.g.- specular scattering). Time domain data is useful for observing local target features (e.g.- non-specular scattering). Ling [5:1148] succinctly contrasts the two classifications:

It is well recognized that electromagnetic signals backscattered from a target contain information useful for classifying and identifying the target. Target characteristics are commonly extracted by analyzing the signal in either the time or the frequency domain. For example, the natural resonance's of a target are manifested in the frequency domain as sharp, discrete events and can be attributed to the unique global features of the target. Similarly, scattering centers are manifested in the time domain as distinct time pulses and can be related to local features on the target.

The primary data formats in this document are RCS versus frequency plots and RCS versus down range and aspect angle images (3-D Images). These data formats are used extensively in Chapter III and Chapter IV for analyzing data.

Radar imaging is a useful analysis tool for understanding scattering from complex targets. The main objective of radar imaging is to locate “hot spots” on a target and then attribute a particular RCS mechanism with each “hot spot”. For the purpose of this

research, radar images are analyzed to ensure measurement returns are actually from the RAM bubble targets and not from another source in the range.

The formal IEEE [12] definition for a radar image is “a spatial distribution of a physical property such as radiation, electric charge, conductivity, or reflectivity mapped from another distribution of either the same or another physical property.” Dean Mensa [14:1] defines a radar image as “spatial distribution of reflectivity corresponding to the object. A collection of reflection coefficients assigned to a three-dimensional array partitioning the object space.” The technique for measuring radar image data is best described by Knott [9:154]:

The fundamental requirement for imaging is to obtain a scattering response that is a function of body location. This is done by causing the relative phase to change in both down and cross range. Down range phase change is accomplished experimentally by sweeping the frequency that changes the relative down range position (phase) of the scattering centers. Cross range phase variation is accomplished by rotating the body. In an electromagnetic sense, we stretch the body in phase (time delay) so that we can reconstruct the physical scattering locations via the Fourier transform. Experimentally, the only way to move scattering centers down range is to vary the number of wavelengths in a down range direction; that is change the frequency.

As powerful and useful as radar imaging is, there are some limitations and hazards associated with its use. The primary limitations are resolution and image smearing. Down range resolution increases with increased frequency bandwidth and is related through the equation:

$$\Delta r = \frac{c}{2\Delta f} \quad (2.11)$$

Where r is resolution, c is the speed of light and Δf is the frequency bandwidth. Cross range resolution increases by increasing the angular bandwidth. However, imaging over large angle band will cause the image to smear and defocus [9].

The one big hazard with using image data is associating image intensity with absolute RCS. An absolute RCS measurement is only attributable to one frequency versus angle with units of dB relative to a square meter (dBsm). Whereas, an image is created by using a Fourier transform, from the frequency domain to the time domain, around a center frequency and center angle with measurements over a band of frequencies and angles. The units used for an image plot are only relative dB. When imaging, the Fourier transform tends to average the data around the specified center frequency and angle. Summarizing, frequency domain data gives an absolute response versus the image or time domain data, which gives an average response [15].

2.7 Linear Regression Analysis

Linear Regression Analysis is a statistics technique used to discover relationships and model interactions among multifactor data. It is a method for fitting curves to data points and then using statistical theory to analyze the properties of the curve fit. Linear Regression models are used for describing structures in data, parameter estimation, prediction and control [16]. The next few paragraphs are intended to summarize the process of Linear Regression Analysis and explain the associated statistics. Linear Regression Analysis is used in this thesis to meet the goal of producing a prediction equation relating RCS to angle, frequency, and bubble geometry. Once a prediction equation is developed, one can use the equation's predictive capabilities to gain further insight into underlying relationships in the RCS data.

2.7.1 Least Squares Estimation (LSE)

SAS-JMP is the software package used to develop the prediction equation. SAS-JMP uses LSE to generate the prediction equation. Therefore, a basic understanding of LSE is important. Equation (2.12), representing a population model, is an example of an equation produced from linear regression analysis.

$$y = \beta_0 + \beta_1 x + \varepsilon \quad (2.12)$$

The dependent variable is y , the independent variable is x , and β_0 and β_1 are the unknown parameter coefficients in the regression model. The primary objective of linear regression is to estimate the unknown parameter coefficients using the method of LSE. According to Montgomery [16:9], LSE estimates " β_0 and β_1 so that the sum of squares of the difference between the observation y_i and the straight line is a minimum." Equation (2.13) is a sample model, a subset of the population model.

$$y_i = \beta_0 + \beta_1 x_i + \varepsilon_0, \quad i = 1, 2, 3, \dots, n \quad (2.13)$$

The statistical error (ε_0) is the parameter that accounts for the failure of the model to perfectly fit the data.

2.7.2 Model Adequacy Checking

After a model is fit to the data using LSE a "quality analysis" of the model is performed to characterize how good the model fits the data. This "quality analysis" is model adequacy checking and is an iterative process of analyzing the residuals and summary statistics tables associated with the model. After the analysis the analyst must decide if the model is appropriate or decide if the model needs modification.

A residual is the difference between an actual measured data point used to develop the model and the value that is modeled for that data point. Mathematically:

$$e_i = y_i - \hat{y}_i = y_i - (\hat{\beta}_0 + \hat{\beta}_1 x_i) \quad (2.14)$$

Where ε_i is the i^{th} residual. Montgomery [16] explains that one can view residuals as realizations of the model errors or a measure of the variability not explained by the model. Residuals (e_i) estimate the statistical error (ε_0) in Equation (2.13). The reason behind performing residual analysis is to evaluate if the model has violated any of the major assumptions needed in linear regression. The five major assumptions are [16]:

- 1) The relationship between y and x is linear
- 2) The error term has zero mean
- 3) The error term has constant variance
- 4) The errors are uncorrelated
- 5) The errors are normally distributed

While small violations of these assumptions are usually tolerable, there is a hazard associated with large violations. The hazard is reduced confidence in the hypothesis testing and confidence intervals. Hypothesis testing is a logical argument process used to compare data to standard statistical distributions. Confidence intervals are intervals around a parameter estimate that has a given probability of containing the true value of the parameter.

The two primary plots used in residual analysis are the normal quantile plot and a plot of the residuals versus the dependent variable y. The normal quantile plot is a visual method for checking the normality assumption, where large violations decrease the

confidence associated with the statistical tests and predictions associated with the model. Normal quantile plots are “designed so that the standard normal cumulative distribution will plot as a straight line [16:59].”

Normally distributed data usually does not plot as a perfect straight line.

However, substantial departures from a straight line can indicate some non-normality in the error. This could mean that there are outliers skewing the data fit or some interaction's are missing in the model. Figure 2-1 shows some examples of the normal probability plots. Figure 2-1(a) is an example of an acceptable normal probability plot. The other figures are examples of normal probability plots that violate the normality assumption. However, these cases are often acceptable. The statistical testing is “robust” to departures from normality if the error distribution is symmetric and unimodal (i.e.-a distribution with one peak). Figure 2-1(d)&(e) plot positive and negative skews respectively and may indicate some non-linearity effects.

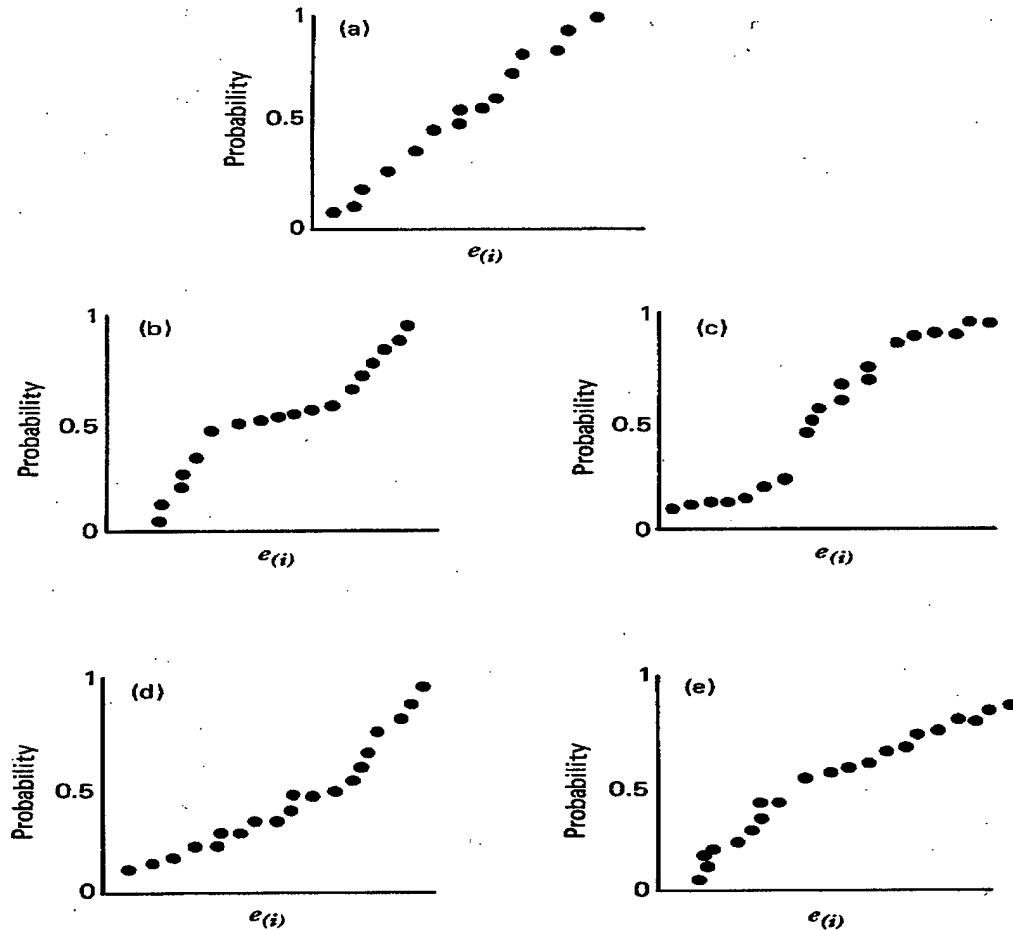


Figure 2-1 Normal probability plots (a) ideal (b) Heavy-tailed (c) Light-tailed (d) Positive skew (e) Negative skew

Another visual method for detecting a departure from the linear regression assumptions is to plot the residuals against the fitted values \hat{y}_i . With a perfect fit, this is a straight-line plot at zero; however, a symmetric rectangular dispersion of values around zero is also acceptable. Departures from a symmetric rectangular dispersion can indicate that there is some non-constant variance in the error terms, a violation of the third assumption, or some nonlinearity, which indicates a need for adding more regressors [16]. Figure 2-2 presents some examples of residual plots. Figure 2-2(a) is an example of a good residual plot because of the symmetric rectangular distribution. Figure

2-2(b)&(c) are examples of nonconstant variance in the error terms and Figure 2-2(d) indicates some nonlinearity effects indicating a need for adding regressors to the model.

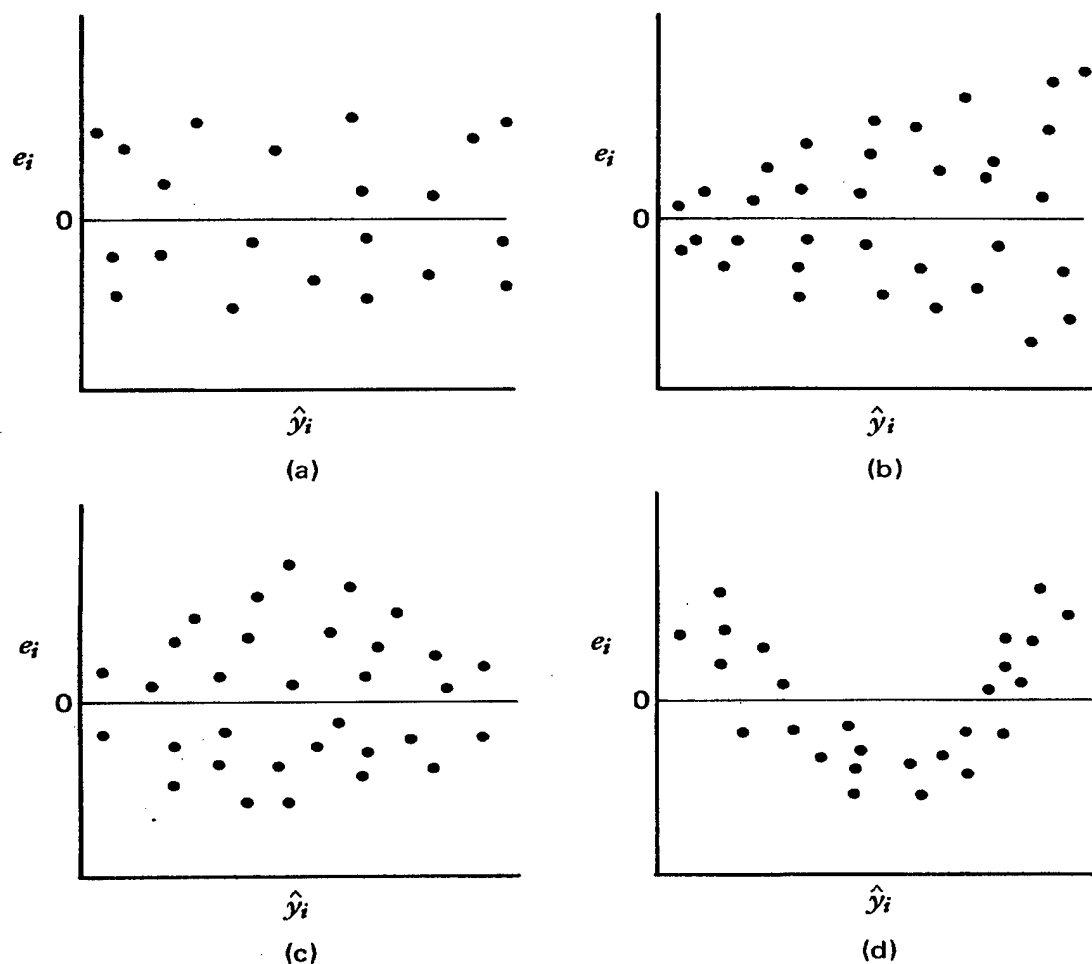


Figure 2-2 Patterns for residual plots (a) Satisfactory (b) Funnel (c) Double bow (d) Nonlinear

After detecting violations of the assumptions, there are several methods for dealing with the violations. The first is to look for outliers and, if needed, discard them. Outliers are data points off by themselves in the plots and represent some extreme observation. "Discarding 'bad' values is desirable because least squares pulls the fitted equation towards the outlier as it minimizes the residual sum of squares. However, we

emphasize that there should be strong nonstatistical evidence that the outlier is a ‘bad’ value before it is discarded [16:70].”

Another method for dealing with violations is to look at transforming the data. Sometimes transforming the data is appropriate and necessary if a linear fit, the first assumption, is deemed as inappropriate. Adding in polynomial terms to the regression equation may also help reduce any curvature in the residuals.

Once the residuals analysis is complete, more insight into the model is gained by delving into the summary statistics tables. Statistics tables are used to show the global model properties and aid the analyst in selecting the proper model variables. The tradeoffs involved in variable selection are including enough regressors to fully describe the data set versus the need to keep the model variance as small as possible with the constraint that the model variance increases with the number of regressors [16]. There are many different types of statistics tables generated from SAS-JMP. The two used in this thesis are the Summary of Fit and Parameter Estimates table.

The primary use of the Summary of Fit table is for evaluating the global properties of the variables in the model. The statistics in the Summary of Fit table are the Coefficient of Determination or R^2 , adjusted R^2 , mean square error (MSE), mean of response, and number of observations.

R^2 is the proportion of variation around the mean due to the independent variables. Mathematically:

$$R^2 = \frac{SS_R}{S_{yy}} = 1 - \frac{SS_E}{S_{yy}} \quad (2.15)$$

where S_{yy} is the corrected sum of squares for y_i , SS_R is the regression sum of squares, and SS_E is the error sum of squares. R^2 is in the interval from 0-1 with values close to one meaning that most of variability is accounted for in the model. The analyst should view R^2 because cautiously arbitrarily increasing the number of variables will automatically increase R^2 . The major use of R^2 is to compare one model to another model. A model with a higher R^2 is generally better than a model with a lower R^2 .

The adjusted R^2 (\bar{R}^2) is similar to R^2 except it is slightly modified to attempt to account for an increased number of independent variables added to the model.

Mathematically:

$$\bar{R}^2 = 1 - \left(\frac{n-1}{n-p} \right) (1 - R^2) \quad (2.16)$$

where p is the number of variables and n is the number of samples. \bar{R}^2 will not necessarily increase with an increased number of regressors in the model. A penalty is paid for increasing p . \bar{R}^2 only decreases if R^2 is reduced significantly as p increases.

The final statistic of interest from the Summary of Fit table is the residual error or root mean square error. The behavior of the MSE is shown in Figure 2-3.

Mathematically:

$$MSE = \frac{SS_E}{n-p} \quad (2.17)$$

“The eventual increase in the MSE occurs when the reduction in SS_E from adding a regressor to the model is not sufficient to compensate for the loss of one degree of freedom in the denominator of Equation (2.16) [16:251].”

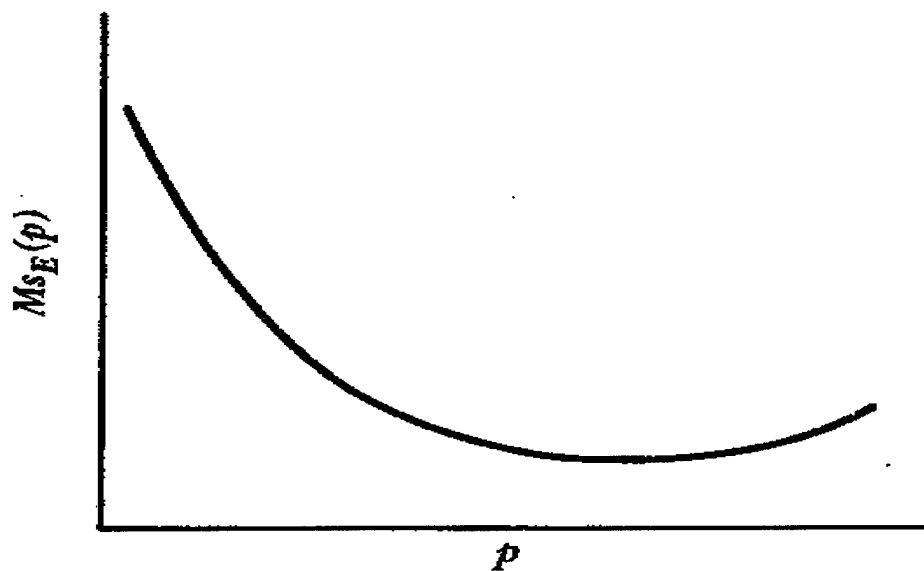


Figure 2-3 Plot of $MSE(p)$ versus p

After looking at the MSE data, the next question is what individual independent variables or regressors are important for the model. Are there any regressors that are not significant in the model and can be removed? Remember, it is important to have the smallest number of regressors possible to reduce the model variance. The Parameter Estimates table is a summary of testing for the significance of each individual regressor.

Consider the model:

$$y = \beta_0 + \beta_1 x_1 + \beta_2 x_2 + \varepsilon \quad (2.18)$$

In order to answer the question "Is this model superior to Equation (2.12)?", one simply needs to test the hypothesis $H_0: \beta_2 = 0$ versus the alternative $H_a: \beta_2 \neq 0$. If, in fact, $\beta_2 = 0$, under assumptions one through five, the least squares estimate of β_2 , $\hat{\beta}_2$ has a known statistical distribution. In repeated sampling, the statistic:

$$t_0 = \frac{\hat{\beta}_2}{se(\hat{\beta}_2)} \quad (2.19)$$

will have a students t-distribution. This distribution has a mean of zero and is symmetric about zero. Large values of t_0 would be unusual, if, in fact, $\beta_2=0$. Thus, one rejects H_0 in favor of H_a if $|t_0| > t_{\alpha/2, n-3}$, where $t_{\alpha/2}$ is the $(1-\alpha/2)(100\%)$ -tile of the t-distribution [16].

2.7.3 Confidence Intervals

Once all of the model adequacy checking is accomplished and the final regression model is built, confidence intervals are constructed to measure the overall quality of the regression. Confidence interval estimates of the independent variable coefficients (β_0 and β_1) and the variance are built with the width of the interval showing the quality of the regression. Of course, the narrower the width of the confidence intervals indicates a better overall regression fit. The interpretation of this interval is that if, in repeated random samples, a large number of such intervals are constructed, $100(1-\alpha)$ percent of them will contain the true value of the unknown parameter. $1-\alpha$ is defined as the confidence coefficient, so to have a 95 percent confidence interval, one would select $\alpha=0.05$. The $100(1-\alpha)$ percent confidence interval on the slope β_1 in Equation (2.12) is distributed according to the t distribution function and in the interval:

$$\hat{\beta}_1 - t_{\alpha/2, n-2} \sqrt{\frac{MS_E}{S_{xx}}} \leq \beta_1 \leq \hat{\beta}_1 + t_{\alpha/2, n-2} \sqrt{\frac{MS_E}{S_{xx}}} \quad (2.20)$$

Similarly for the intercept β_0 :

$$\hat{\beta}_0 - t_{\alpha/2, n-2} \sqrt{MS_E \left[\frac{1}{n} + \frac{\bar{x}^2}{S_{xx}} \right]} \leq \beta_0 \leq \hat{\beta}_0 + t_{\alpha/2, n-2} \sqrt{MS_E \left[\frac{1}{n} + \frac{\bar{x}^2}{S_{xx}} \right]} \quad (2.21)$$

where the standard error of the slope β_1 and the intercept β_0 are:

$$se(\hat{\beta}_1) = \sqrt{\frac{MS_E}{S_{xx}}} \quad (2.22)$$

$$se(\hat{\beta}_0) = \sqrt{MS_E \left[\frac{1}{n} + \frac{\bar{x}^2}{S_{xx}} \right]} \quad (2.23)$$

The standard error is used as a measure of how precisely the slope and intercept are estimated. *One important note about confidence intervals is that they are not prediction intervals for future observations (y_0).* The $100(1-\alpha)$ percent prediction interval for a future observation at some x_0 is [16]:

$$\hat{y}_0 - t_{\alpha/2, n-2} \sqrt{MS_E \left[1 + \frac{1}{n} + \frac{(x_0 - \bar{x})^2}{S_{xx}} \right]} \leq y_0 \leq \hat{y}_0 + t_{\alpha/2, n-2} \sqrt{MS_E \left[1 + \frac{1}{n} + \frac{(x_0 - \bar{x})^2}{S_{xx}} \right]} \quad (2.24)$$

where $\hat{y}_0 = \hat{\beta}_0 + \hat{\beta}_1 x_0$, represents the prediction equation. Additionally, the prediction interval at x_0 is always wider than the confidence interval at x_0 because the prediction interval accounts for both the errors from the prediction equation and error in future observations.

More generally, if one considers the linear regression model:

$$y = \beta_0 + \beta_1 x_1 + \beta_2 x_2 + \dots + \beta_p x_p + \varepsilon \quad (2.25)$$

$$y = \bar{X}^T \bar{\beta} + \varepsilon \quad (2.26)$$

where $\bar{x}^T = (1, x_1, x_2, \dots, x_p)$, $\bar{\beta}^T = (\beta_0, \beta_1, \dots, \beta_p)$. If one observes several instances of y , $\bar{y} = (y_1, y_2, \dots, y_n)^T$ along with corresponding $\bar{x}_i^T = (1, x_{i1}, x_{i2}, \dots, x_{ip})$, the sample based model of Equation (2.26) is given by:

$$\bar{y} = X\bar{\beta} + \bar{\varepsilon} \quad (2.27)$$

where $X = (\bar{x}_1, \bar{x}_2, \dots, \bar{x}_n)^T$ and $\bar{\varepsilon} = (\varepsilon_1, \varepsilon_2, \dots, \varepsilon_n)$. The least squares estimate of $\bar{\beta}$ is:

$$\hat{\bar{\beta}} = (X^T X)^{-1} X^T \bar{y} \quad (2.28)$$

where $\hat{\bar{\beta}}^T = (\hat{\beta}_0, \hat{\beta}_1, \dots, \hat{\beta}_p)$. The errors associated with this estimate are:

$$e = \bar{y} - \hat{\bar{y}} = y - X\hat{\bar{\beta}} \quad (2.29)$$

The sum of squared error is $SSE = \bar{e}^T \bar{e}$ and $MSE = SSE / (n - p - 1)$. Under the assumption that the errors are identically and independently normally distributed with zero mean and variance (σ^2) then:

$$\hat{\bar{\beta}} \approx N_{p+1}(\bar{\beta}, (X^T X)^{-1} \sigma^2) \quad (2.30)$$

letting $\Sigma = (X^T X)^{-1} \sigma^2$ then $\text{var}(\hat{\bar{\beta}}) = \Sigma_{ii}$ and $\text{cov}(\hat{\beta}_i, \hat{\beta}_j) = \Sigma_{ij} = \Sigma_{ji}$ the statistic

$$t_i = \frac{\hat{\beta}_i}{se(\hat{\beta}_i)} \quad (2.31)$$

where $se(\hat{\beta}_i) = \sqrt{\Sigma_{ii} MSE \sigma^{-2}}$ are distributed according to a t-distribution with $(n-p-1)$

degrees of freedom and we reject $H_0: \beta_i = 0$ versus $H_a: \beta_i \neq 0$ if $|t_0| > t_{\alpha/2, n-p-1}$. The standard

error of an estimated $y_0 = X_0^T \beta$ the point $\bar{X}_0^T = (1, X_{01}, X_{02}, \dots, X_{0p})$ is:

$$s.e.(\hat{y}_0) = (MSE[1 + \bar{X}_0^T (X^T X)^{-1} \bar{X}_0])^{1/2} \quad (2.32)$$

where $\hat{y}_0 = \bar{X}_0^T \hat{\beta}$ and a $(1-\alpha)(100\%)$ confidence interval for y_0 is [16]:

$$\hat{y}_0 \pm t_{\alpha/2, n-p-1}(s.e.(\hat{y}_0)) \quad (2.33)$$

In Chapter IV, the prediction intervals are plotted around each bubble RCS prediction to show what the 95% prediction confidence level is.

2.7.4 Model Validation

The goal of model validation is to decide if the regression model built, using linear regression analysis, will properly operate when given to the user. Model validation is different than the model adequacy-checking goal of ensuring the model is properly fit to the data. There are three model validation-testing techniques used to evaluate a model's usability. The first is "analysis of the model coefficients and predicted values including comparison with prior experience, physical theory, and other analytic models or simulation results [16:425]." Next, is collecting new data to investigate the model's predictive performance. Finally, there is the option of using data splitting. Data splitting sets aside portions of the original data for use in investigating the model's predictive performance [16]. For this thesis, the data splitting technique is utilized to properly validate the model.

2.8 RCS Simulation Software

There are two needs for using RCS simulation software tools. The first need is to generate simulated data to compare with measured data for exploring alternative methods for generating an RCS database. The second need is to generate E-field values

(magnitude and phase information) from a well-characterized low RCS body (e.g.-NASA almond). The E-field values are needed so E-field data from a measured RAM bubble can be coherently added to the almond. The process of adding the fields simulates an almond with a bubble on it. Comparisons of the almond are then made with and without the bubble to demonstrate the effect of the bubble on the almond's RCS signature and the associated change in radar detection range.

The universe of electromagnetic prediction software is divided into three areas; high frequency methods, low frequency methods and hybrid methods. The high frequency methods are an approximate formulation of Maxwell's Equations that use numerical methods requiring the dimensions of the scattering object or "body part" to be greater than the wavelength of the incident field. High frequency methods assume each body part acts independently relative to each other and are therefore useful for predicting specular and diffracted terms [9]. Conversely, low frequency methods are used when the dimensions of the body parts are on the order of or smaller than a wavelength. Low frequency methods represent an exact formulation of Maxwell's Equations, and therefore account for the influence of each of the targets body parts relative to all the other body parts. Thus, all of the various RCS return phenomenology is accounted for, i.e.- specular, edge diffractions, traveling waves, creeping waves, and shadowing [9]. The major tradeoff between high frequency and low frequency methods is speed versus accuracy. Hybrid methods, as the name implies, are hybrid combinations of high and low frequency methods designed to take advantage of each technique while avoiding their individual weaknesses. As hybrid methods are not used in this research, they are not discussed further.

The first need for RCS software is to simulate the measured RCS data to compare with the measurements. If the simulations compare well with the measurements, then simulations could serve as an alternative or complementary means for building an RCS database. Because the RAM bubbles are on the order of a wavelength and non-specular features are important to account for, the simulation of the RCS measurements of a RAM bubble requires the use of a low frequency method. The software selected to simulate the RCS measurement of bubbles in RAM is Jim Rogers Monstrous Body of Revolution (JRMBOR) moment method code. JRMBOR is a Moment Method code that uses surface integral equations to compute a single frequency monostatic or bistatic solution from a BOR [17]. The Moment Method is a numerical technique that breaks a linear operator equation into a system of linear equations that approximates the solution to the linear operator equation. The numerical solution to the equations represents an approximate solution to the exact formulation [9].

The other need for RCS simulation software is to generate the field values of a low RCS target, in this case, the NASA almond. Ideally, actual measured data of a RAM covered Almond is necessary. However, fabricating a RAM covered almond target is impractical and simulated data using XpatchF was a sensible option. Imbedded in the XpatchF software is an almond input file that is used as a test case. The file is easily modified for a RAM coating.

XpatchF [18:1] is a high frequency RCS prediction software package. The software is based on the Shooting & Bouncing Ray (SBR) technique and is thoroughly explained in the introduction section:

In SBR, a dense grid of rays is shot from the radar direction toward the target. Rays are traced according to geometrical optics theory as they

bounce around within the target. This tracing includes the effects of polarization, ray divergence factor, and layered material transmission or reflection. At the point where a ray exits the target, a physical optics integration is done to calculate the scattered far field from the target. Thus, in using SBR single and multiple bounce contributions are accounted for by geometrical or physical optics theory.

2.9 Summary

This chapter overviewed the necessary theory and tools used in this thesis to generate and analyze RCS data. Understanding the theory and tools is necessary to properly apply them in the measurement and analysis aspects of this research effort. Specifically, the literature review concluded that small surface features can increase a target's RCS and are a function of angle, frequency and geometry. The RAM section introduced the material properties (relative permeability and relative permittivity) and explained the complexity of RAM. The material measurement section discussed the focused beam system used to measure the RAM's material properties. The RCS fundamentals and measurement section defined RCS and reviewed the technique used to measure the RAM bubble's RCS. The linear regression analysis section detailed the least squares estimation method and the iterative process of building a prediction equation. Finally, the RCS simulation software section provided an overview of electromagnetic code prediction theory and two software tools used to calculate RCS data. In the next chapter we turn our attention to describing the equipment set up, procedures, test matrix, data examples, and error analysis for the data collections.

Chapter 3 Methodology

The methodology chapter is divided into four sections. The first section explains the material measurements data collection. The second section, the most important part of this research, details measuring the RCS of various sized bubbles in RAM. The third section discusses the use of JRMBOR to produce simulated RCS data from a RAM bubble. The final section describes the process for simulating the E-field values of the low RCS almond target.

3.1 Introduction

Chapter II provided the necessary knowledge to understand the basic theory and techniques used in this chapter to generate data. The purpose of Chapter III is to explain the equipment setup, procedures, data, and uncertainty analysis of the data collection tasks involved in this research effort. The methodology section is important to understand so the proper inference and conclusions are drawn in the data analysis and applications chapter.

3.2 RAM Characterization

The purpose of material measurements is to generate data for use in characterizing the RAM's attenuation. The data also serves as an input for the simulation software. The material measurement data is generated by measuring the material's complex relative permittivity and relative permeability over the frequency range from 4-18 GHz. Ideally, measurements down to 2 GHz are needed. However, the system is constrained on the low end at 4 GHz.

3.2.1 Equipment

As discussed in the material measurement section of chapter II, the focused beam system was chosen for the materials data collection. The focused beam system consists of a boom arch assembly, a Hewlett-Packard (HP) 8510 network analyzer, standard transmission line connections and an external personal computer. The boom arch assembly is shown in Figure 3-1. The essential features of the boom arch assembly are the antenna horns and large dielectric lenses on either side of the sample holder. The horns and lenses are adjustable and the sample holder is mounted on a rotator. The physical size of the boom arch assembly is roughly 12' long, 2' wide and 4' tall.

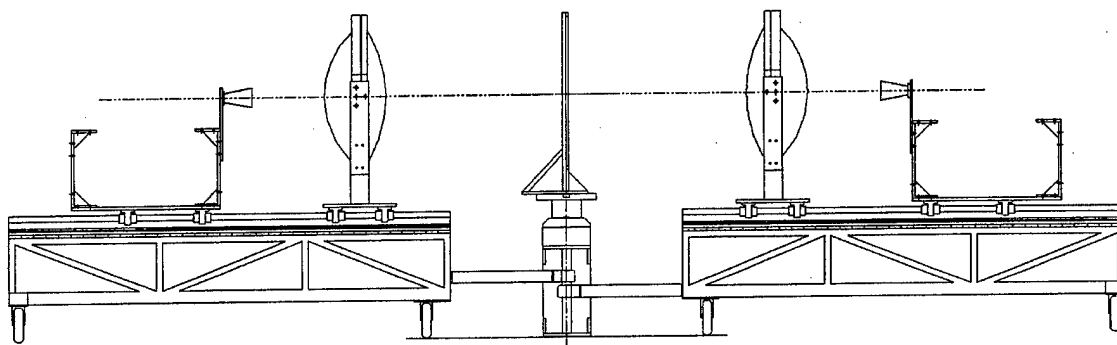


Figure 3-1 Focused Beam Assembly

The other major piece of equipment in the focused beam system is the HP 8510 network analyzer. The HP 8510 displays the measured data in terms of the complex scattering matrix parameters S_{11} and S_{21} [10]. These parameters are defined in Figure 3-2 for a two port device.

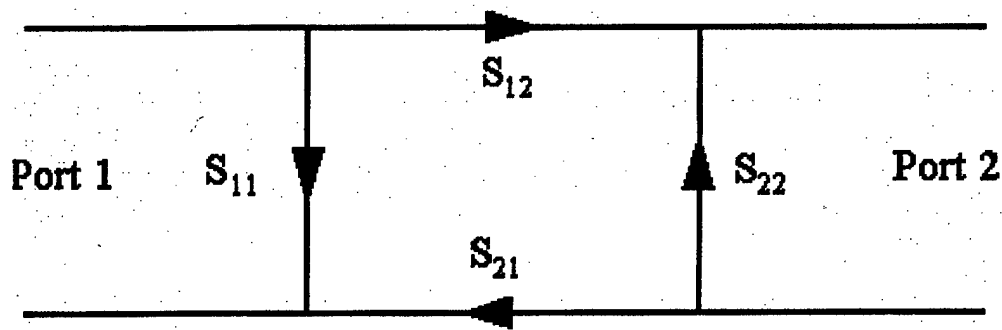


Figure 3-2 S-Parameter Definition for a Two-Port Network

3.2.2 Procedures

The first step in the materials characterization procedure was to cut the RAM into a 2'x2' piece, strip the metal backing off and then use double sided tape to adhere the RAM sample to the 2'x2' sample holder frame. The next step was to use a micrometer to measure the RAM's thickness at the center of the sample. The thickness was recorded to be 0.093".

After the thickness was measured, the focused beam system was used to take a calibrated measurement of the RAM at normal incidence. The S_{11} data was calibrated by ratioing the S_{11} raw data from the sample with the S_{11} of a metal plate, effectively a short. Similarly, the S_{21} data was calibrated by ratioing S_{21} raw data with the S_{21} of an empty sample holder, effectively an open.

$$S_{11}^{cal} = \frac{S_{11}^{sample}}{S_{11}^{short}} \quad (3.1)$$

$$S_{21}^{cal} = e^{-i\gamma_0 t} \frac{S_{21}^{sample}}{S_{21}^{open}} \quad (3.2)$$

$$\gamma_0 = \sqrt{k_0^2} \quad (3.3)$$

Note the phase correction term (γ_0) in Equation 3.2. This term corrects for the extra length in the sample path caused by the sample thickness [10].

3.2.3 Data

After the calibrated S_{11} and S_{21} measurements were taken, the next step was to use a MATLAB routine implementing the Nicolson-Ross-Weir algorithm, outlined in chapter II, to calculate the relative permittivity and relative permeability. Figure 3-3 and Figure 3-4 are plots of the real and imaginary parts of the relative permittivity and relative permeability for 4-18 GHz. On each plot the top line is the real part and the bottom line is the imaginary part. One feature of the plots to notice is the error bars associated with the measurement. The error analysis section that follows demonstrates that the error is well characterized and therefore only one measurement of the RAM sample was necessary.

3.2.4 Uncertainty

The factors that contribute to the uncertainty are associated with the HP 8510, the transmission lines and connections, the sample and focused beam limitations (e.g.- deviations from a plane wave at the sample, multipath noise, etc). The focused beam limitations were not characterized by AFRL/XPB and therefore are not discussed. The limitations of the HP 8510 are expressed in Figure 3-5 and accounted for in the uncertainty analysis software.

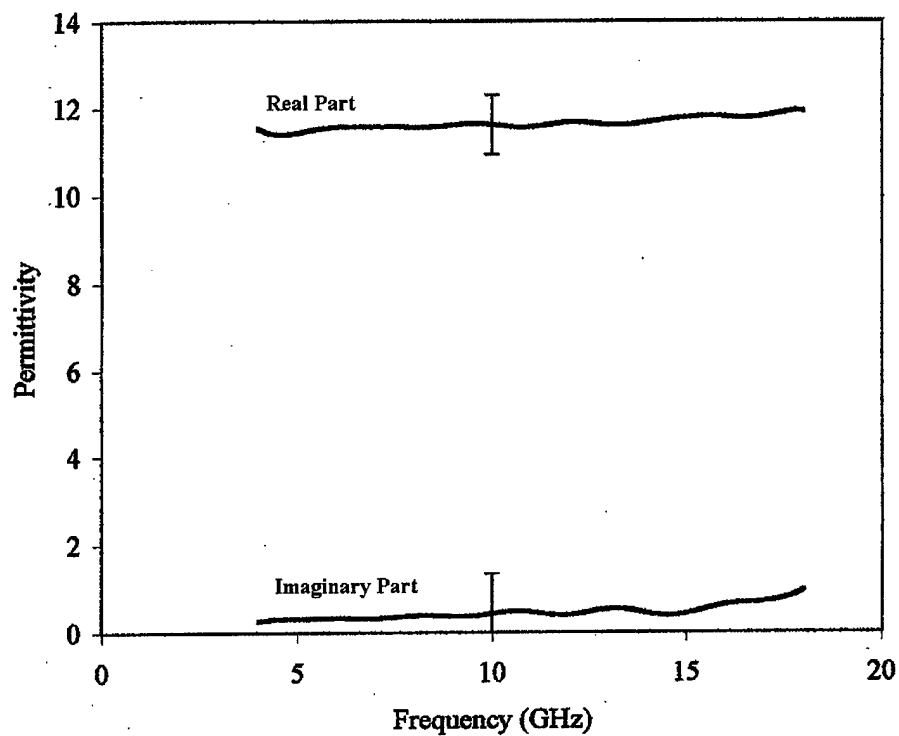


Figure 3-3 Measured Relative Permittivity

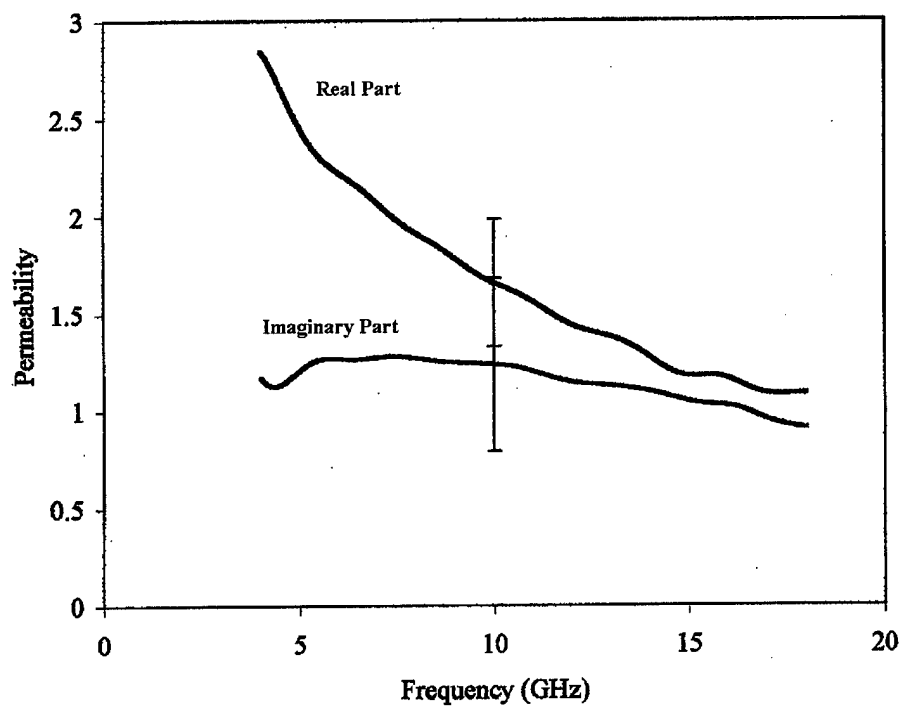


Figure 3-4 Measured Relative Permeability

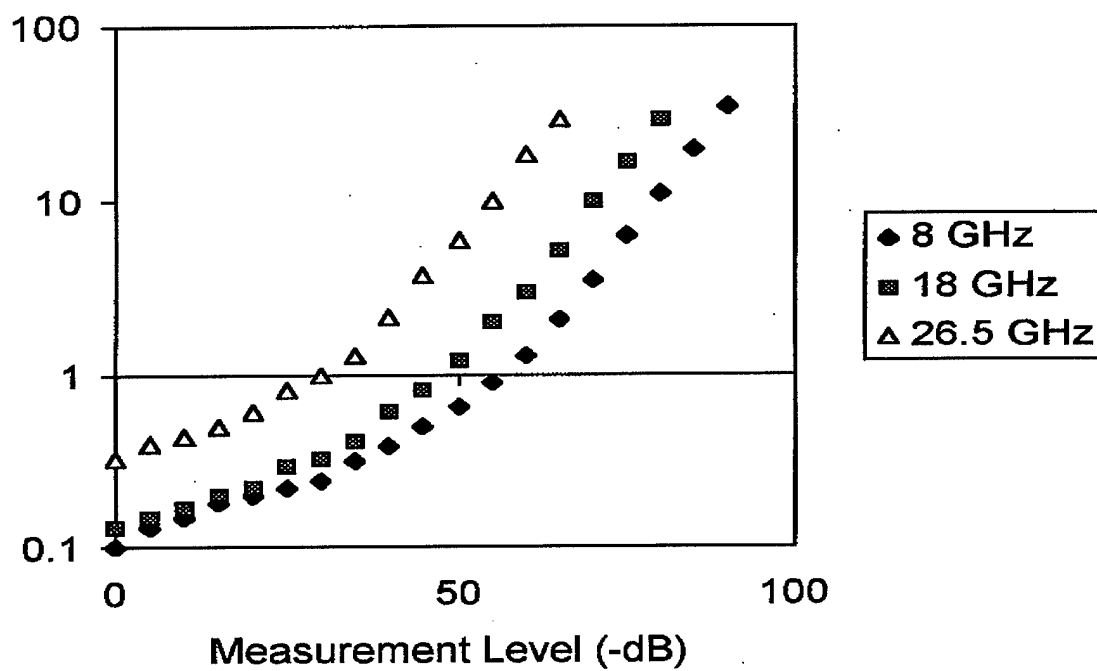
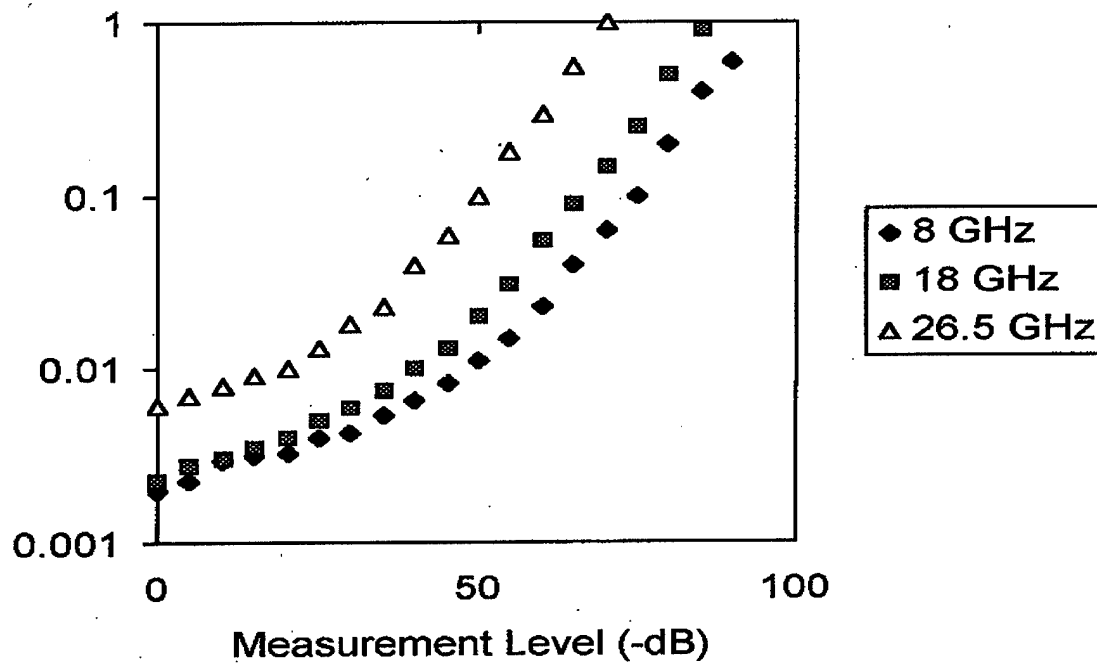


Figure 3-5 Stated Accuracy of the Magnitude and Phase of HP-8510 S-parameter Measurements [10]

The transmission line errors are caused by the various junction mismatches in the system. The S parameter calibration procedures and a 1ns-time domain gate are implemented to eliminate most of the transmission line errors. Errors in the sample come from two sources. The first is in the micrometer measurement of the thickness. The error associated with the thickness measurement is less than 0.5 mils. The other sample error source is the flatness of the sample when positioned in the focused beam system for measurement. The sample flatness error can cause an error in the phase and is expressed in Equation (3.4) where δL is the sample position uncertainty and γ_0 is defined in Equation (3.3).

$$\delta\Theta = \gamma_0 \delta L \quad (3.4)$$

Each of the errors contributes to the error in the magnitude and phase of the scattering parameters and sample thickness. Equations (3.5) and (3.6) summarize the total error in the relative permittivity and relative permeability measurements [10].

$$\delta\epsilon = \sqrt{\left(\frac{\delta\epsilon}{\delta|S_{11}|} \delta|S_{11}|\right)^2 + \left(\frac{\delta\epsilon}{\delta\Phi_{11}} \delta\Phi_{11}\right)^2 + \left(\frac{\delta\epsilon}{\delta|S_{21}|} \delta|S_{21}|\right)^2 + \left(\frac{\delta\epsilon}{\delta\Phi_{21}} \delta\Phi_{21}\right)^2 + \left(\frac{\delta\epsilon}{\delta t} \delta t\right)^2} \quad (3.5)$$

$$\delta\mu = \sqrt{\left(\frac{\delta\mu}{\delta|S_{11}|} \delta|S_{11}|\right)^2 + \left(\frac{\delta\mu}{\delta\Phi_{11}} \delta\Phi_{11}\right)^2 + \left(\frac{\delta\mu}{\delta|S_{21}|} \delta|S_{21}|\right)^2 + \left(\frac{\delta\mu}{\delta\Phi_{21}} \delta\Phi_{21}\right)^2 + \left(\frac{\delta\mu}{\delta t} \delta t\right)^2} \quad (3.6)$$

Where $\delta\epsilon$ and $\delta\mu$ represent the total error in the relative permittivity and relative permeability measurements, respectively.

3.3 RCS Measurements

The RCS measurement of various sized RAM bubbles is the “heart and soul” of this thesis project. Without having measured RCS data and experienced the process and problems associated with experimentation, this project would have lacked the insight gained from living with the real world problems associated with bubbles in RAM. The RCS measurements build a database used in Chapter IV for developing a prediction model. In addition, the measured data is analyzed in Chapter IV to characterize the absolute RCS of a bubble in RAM.

3.3.1 Equipment

AFRL/XPN’s compact range was a perfect fit for this thesis work because of its specialized mission and strengths in highly experimental, one-of-a-kind RCS measurements. The primary reasons for using AFRL/XPN’s range are the range’s measurement capabilities. These capabilities include the sensitivity to measure a small RCS target, the desired frequency range coverage (e.g.-2-18 GHz), and the measurement speed.

The compact range uses a Gregorian dual reflector/dual chamber design. The main reflector has a full blended, rolled edge parabolic design. The subreflector, located under the main chamber floor, is a serrated edge elliptical reflector. The AFRL/XPN compact range design is depicted in Figure 3-6.

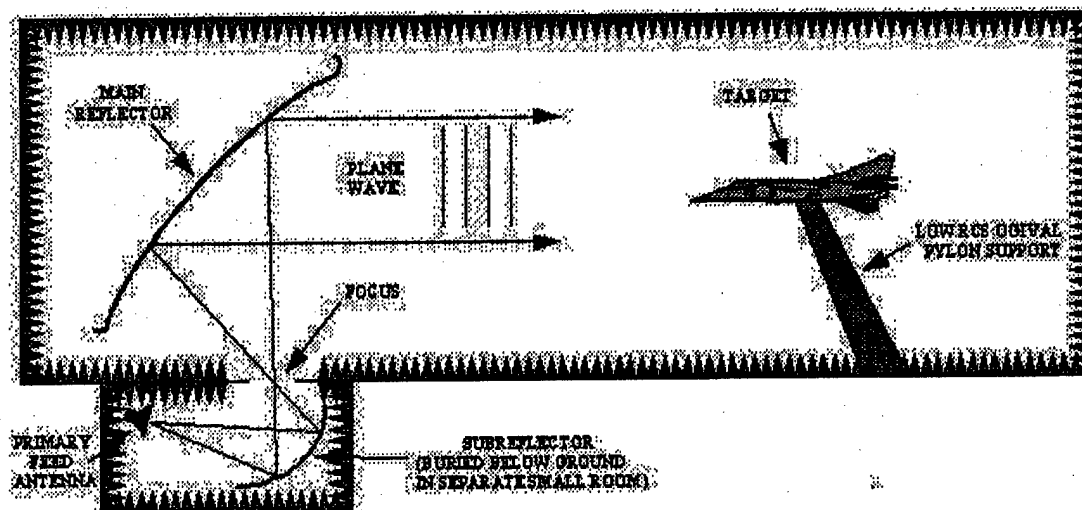


Figure 3-6 AFRL/XPN Compact Range Design [19]

The philosophy behind a dual reflector system is that compared to a single reflector system it produces a uniform plane wave with very little amplitude taper or ripple, almost zero phase variation, a virtually zero cross-polarization component, and no feed blockage or feed spillover [13].

Some specifications for the compact range are:

- Main Chamber: 96' (length) X 59' (width) X 45' (height)
- Main Reflector: 38' X 38', parabolic
- Sub-Reflector: 19' X 10', ellipsoidal
- Quiet Zone: 25' (length) X 20' (width) X 15' (height)
- Amplitude Ripple: < 0.2 dB
- Amplitude Taper: < 0.25 dB
- Cross Polarization: < -35 dB to -40 dB
- Temperature: 70° ± 1.5° Fahrenheit

The compact range uses a Lintek 5000 radar system that provides continuous frequency coverage from 0.8-18.0 GHz and 26.0-36.0 GHz, each with a single antenna. Other capabilities are pulsed IF or pulsed CW mode, dual receive channels, and variable integration's. The variable integration allows for a tradeoff of speed versus sensitivity based on range time and target RCS level requirements [19].

The last major piece of equipment needed for the RCS measurement testing is a testbody. A testbody is a platform used to mount a test article on; in this case, the test article is the RAM with and without bubbles. Figure 3-7 is a picture of the testbody designed by Mission Research Corporation (MRC). The MRC testbody is 8'(long) x 4'(wide), and useful for measurements from grazing (0°) incidence out to about 85° . It is important for the testbody to have a very low RCS return so that it does not mask the return of the test article mounted on it. Figure 3-7 depicts the RAM strip with a bubble as the test article. One other noteworthy feature of the testbody, not depicted in Figure 3-7, is a creeping wave suppression technique on the testbody's backside. The technique is a tapered hole cut in the testbody and filled with bulk absorber material. The gradual taper allows the attached surface waves to propagate into the absorber material with very little reflection.

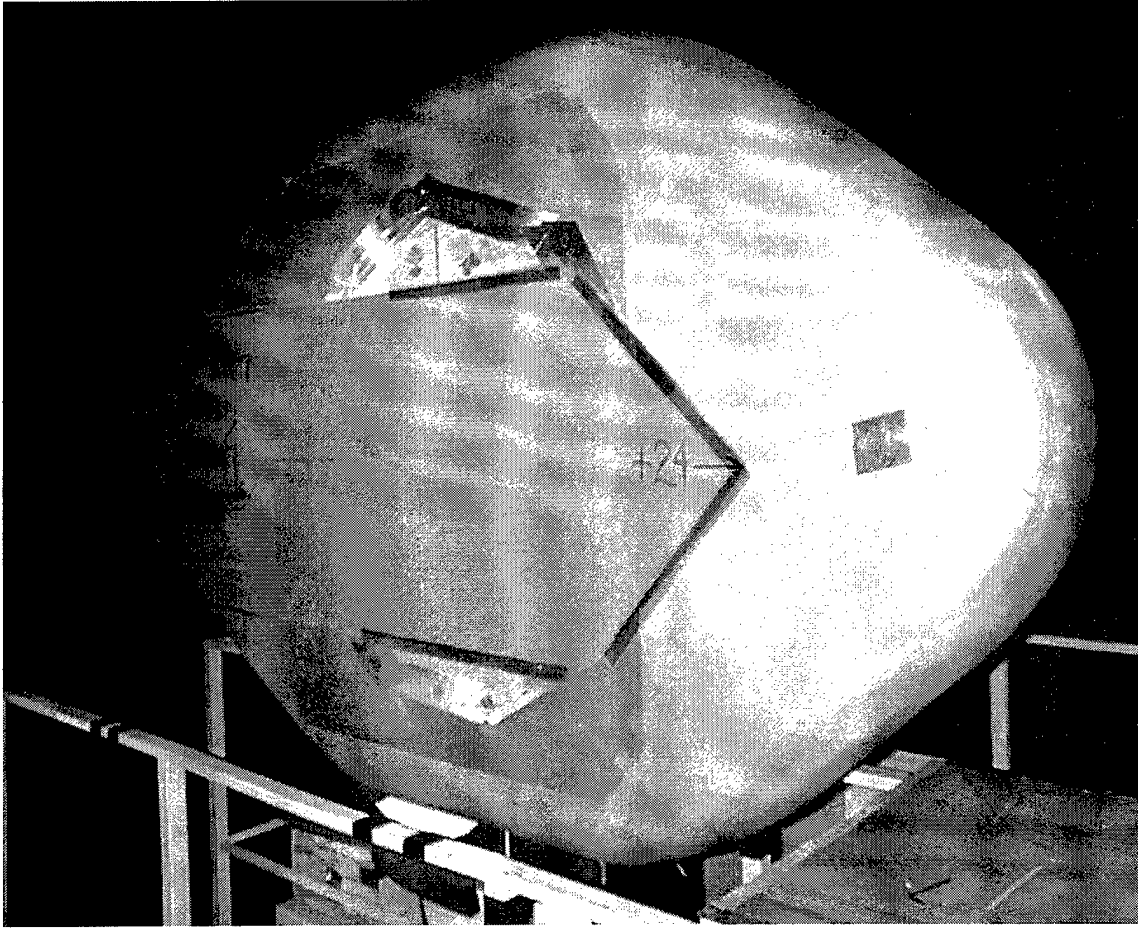


Figure 3-7 MRC Testbody with RAM Strip

3.3.2 Procedures

The procedures followed to measure the RCS of the various sized bubbles are straightforward. In the simplest terms, one “fills in the blanks” of Equation (3.7).

$$\sigma = 4\pi \left| \frac{\bar{E}_{target} - \bar{E}_{targetbackground}}{\bar{E}_{calibration} - \bar{E}_{calibrationbackground}} (\bar{E}_{calibrationexact}) \right|^2 \quad (3.7)$$

“Fill in the blanks” means taking four measurements. The fifth term, $\bar{E}_{calibrationexact}$, is determined from a theoretical solution. In this case, it is the theoretical solution for a squat cylinder. The following list defines the four measured terms:

- $\bar{E}_{calibration}$: a measurement of the squat cylinder mounted on the pylon
- $\bar{E}_{calibrationbackground}$: a measurement of just the pylon
- \bar{E}_{target} : a measurement of the testbody with a bubble
- $\bar{E}_{targetbackground}$: a measurement of the testbody without a bubble

Understanding the premise of Equation (3.7) is the most important measurement concept of this thesis. Equation (3.7) mathematically represents the absolute RCS of the RAM bubbles. In Equation (3.7), the process of vector subtracting \bar{E}_{target} and $\bar{E}_{targetbackground}$ produces \bar{E}_{bubble} . The vector subtraction allows, for the most part, the removal of the effects of the testbody. Therefore, the final measured RCS value (σ) is the absolute RCS of the bubble. Several other important factors to understand about the measurement procedures are the angle and frequency band of each measurement, test matrix, how the bubble is physically fabricated and data quality control.

Each \bar{E}_{target} and $\bar{E}_{targetbackground}$ measurement was taken over an angle band in azimuth the from grazing incidence (0°) to 45° in 0.5° increments and a frequency band from 2 to 18 GHz in 20 MHz increments. The measurement increments were dictated by AFRL/XPN for data quality purposes. In addition, due to the relatively small signature from the bubbles, 16324 integrations were performed over each frequency increment to reduce range clutter and noise. Each \bar{E}_{target} and $\bar{E}_{targetbackground}$ measurement took approximately forty-five minutes to perform, not including setup time. The $\bar{E}_{calibration}$ and $\bar{E}_{calibrationbackground}$ measurements were taken over a frequency band from 2 to 18 GHz in 20 MHz increments and only at one incidence angle due to 360° symmetry. Additionally,

the calibration measurements were only taken once per day, whereas each \bar{E}_{target} and

$\bar{E}_{targetbackground}$ measurement was taken for each configuration setup.

The idea behind the original test matrix was to measure three different sized bubbles (small, medium, and large) three times each over the angle and frequency bands of interest. There was also a desire to measure polarization's, TE and TM. However, after analyzing the first few measurements it was determined that the TM case was not of interest because it did not produce a significant return.

In the paragraph above, the word original was used in reference to the test matrix because, like most experimental endeavors, test matrices change. The reason why the test matrix changed was producing three bubbles exactly the same size and shapes three different times was impossible. The reason why producing repeatable bubbles was impossible is difficult to explain. In the simplest terms, metal-backed RAM is not stretchable and therefore very hard to work with. In reality, measurements were taken of ten various size and shaped bubbles, some of which are "similar". Table 3-1 summarizes the test matrix.

Table 3-1 Test Matrix (inches)

Configuration	length	width	height	area	volume	perimeter	Category
Bkg4	0.00	0.00	0.00	0.00	0.00	0.00	N/a
c1r1	8.00	4.00	0.25	32.00	4.00	24.00	medium
c1r2	11.00	3.50	0.25	38.50	4.81	29.00	large
c2r1(c2hh)	14.50	3.50	0.25	50.75	6.34	36.00	large
c3r1	6.00	4.00	0.25	24.00	3.00	20.00	small
c3r2	7.00	5.00	0.25	35.00	4.38	24.00	medium
c3r3	7.00	5.00	0.25	35.00	4.38	24.00	medium
c3r4	7.00	5.00	0.25	35.00	4.38	24.00	medium
c4r1	8.00	8.00	0.25	64.00	8.00	32.00	large
c4r2	16.00	4.00	0.25	84.00	10.50	40.00	large
c5r1	5.00	4.00	0.25	20.00	2.50	18.00	small

At this point, a few pictures are necessary to illustrate the variability in the bubble geometry.

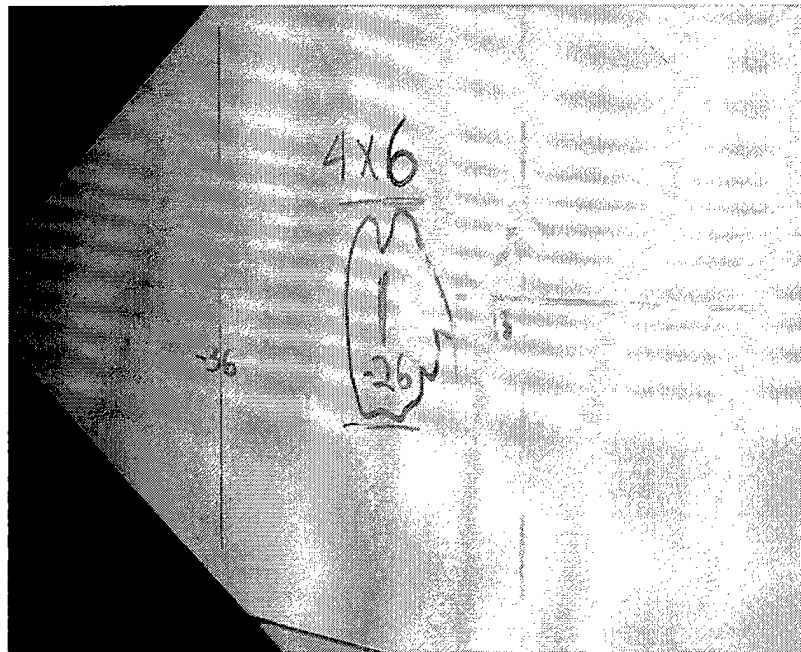


Figure 3-8 An Example of a Bubble in RAM

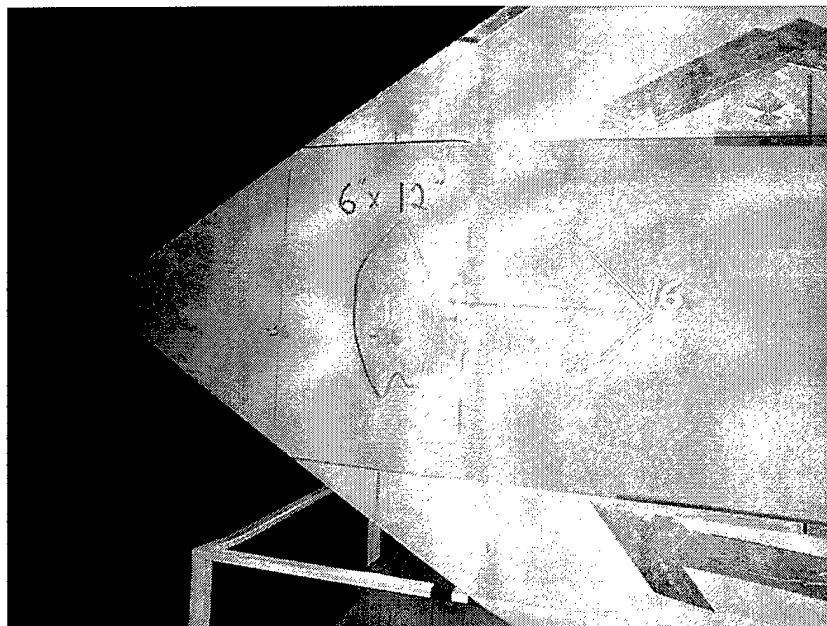


Figure 3-9 Another Example of a Bubble in RAM

In Figure 3-8 and Figure 3-9, it is easy to see the variability and randomness in size and shape of the RAM bubbles. The variability and odd bubble shapes are caused by a combination of the amount of spray tack used for adhesion and the metal backing on the RAM. The metal backing makes it impossible to reproduce the same bubble, therefore each bubble is unique. While on the topic of the variability in the bubble geometries, it is necessary to also explain how the bubbles were induced under the RAM.

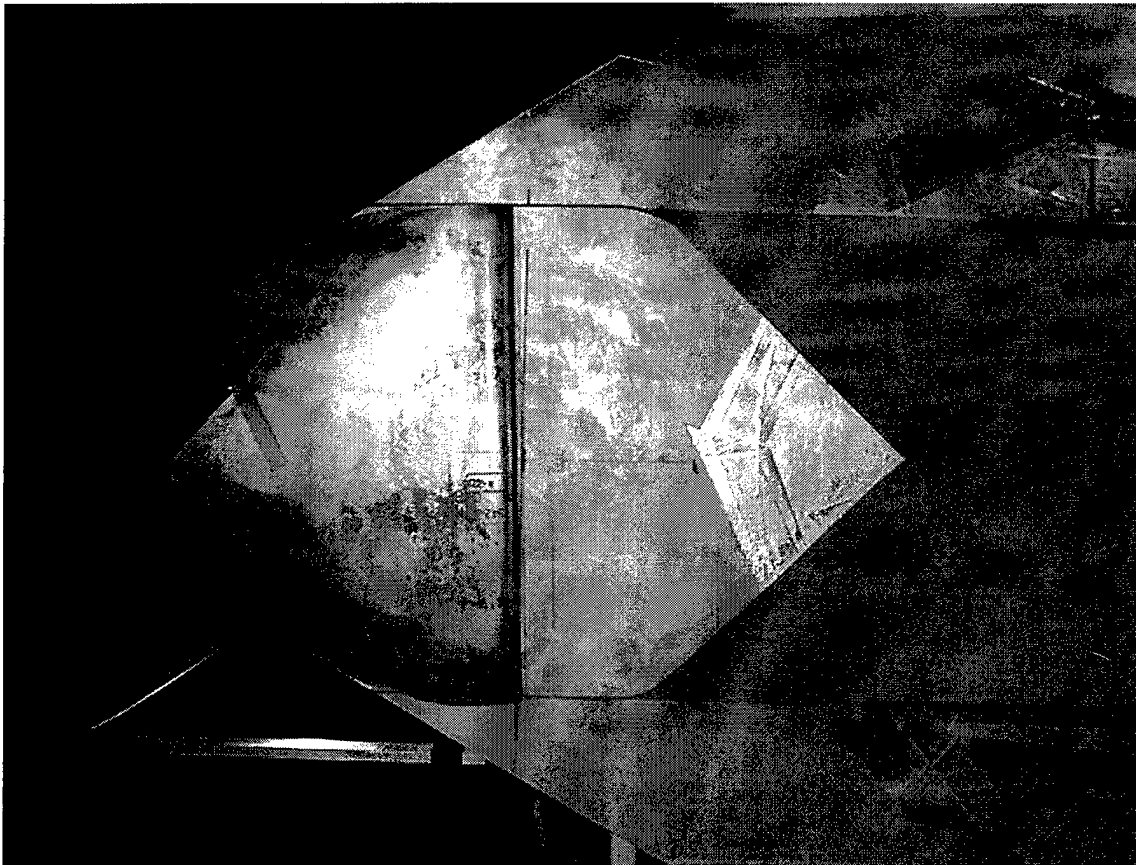


Figure 3-10 Peeled Back RAM with Styrofoam Insert

Figure 3-10 illustrates how a bubble was induced in the RAM. $\frac{1}{4}$ " thick pieces of styrofoam were glued to the testbody and then the RAM was glued down over the styrofoam. Four different sized pieces of styrofoam were used, 1"x1", 2"x2", 4"x4" and

2"x6". Furthermore, the RAM sheet was cut in the middle to ease the bubble insertion process. Notice the shiny metal back of the RAM.

In the preceding paragraphs, the procedures used to collect RCS data was discussed and may have come across as a relatively easy task. However, the equipment and procedures used were very delicate and very sensitive to perturbations. Therefore, it was important to perform data quality evaluation to ensure all aspects of the measurement procedures were performed properly. The two primary methods used to ensure data quality were performing a daily "double calibration" and analyzing the raw collected data after each measurement was completed and before another measurement was started.

The first method to ensure data quality is to perform a daily "double calibration." The procedure is a straightforward idea to understand. The target measurement in Equation (3.7) was replaced with a second, different sized, calibration cylinder [20].

$$\sigma = 4\pi \left| \frac{\overline{E}_{cal primary} - \overline{E}_{cal primary background}}{\overline{E}_{cal sec ondary} - \overline{E}_{cal sec ondary background}} \overline{E}_{cal sec ondary exact} \right|^2 \quad (3.8)$$

Next, the "double calibration" measured RCS is compared with the exact theoretical RCS of the primary calibration object. Figure 3-11 is an example of the measurement and the comparison. Note in Figure 3-11 the black plot is the exact solution, the blue plot is the measured data and the red plot is the range noise + clutter. The blue plot almost exactly matches the black plot. This indicates that the system was working properly.

The second method used to ensure data quality was to continuously analyze the raw measured data. Unfortunately, this is an ill-defined task because of the plethora of

factors to look for. However, a short list can serve as a beginning point for the features an experienced range engineer looks for:

- Data drop outs
- Subtractability
- Noise floor increase
- Scattering center locations in predicted areas

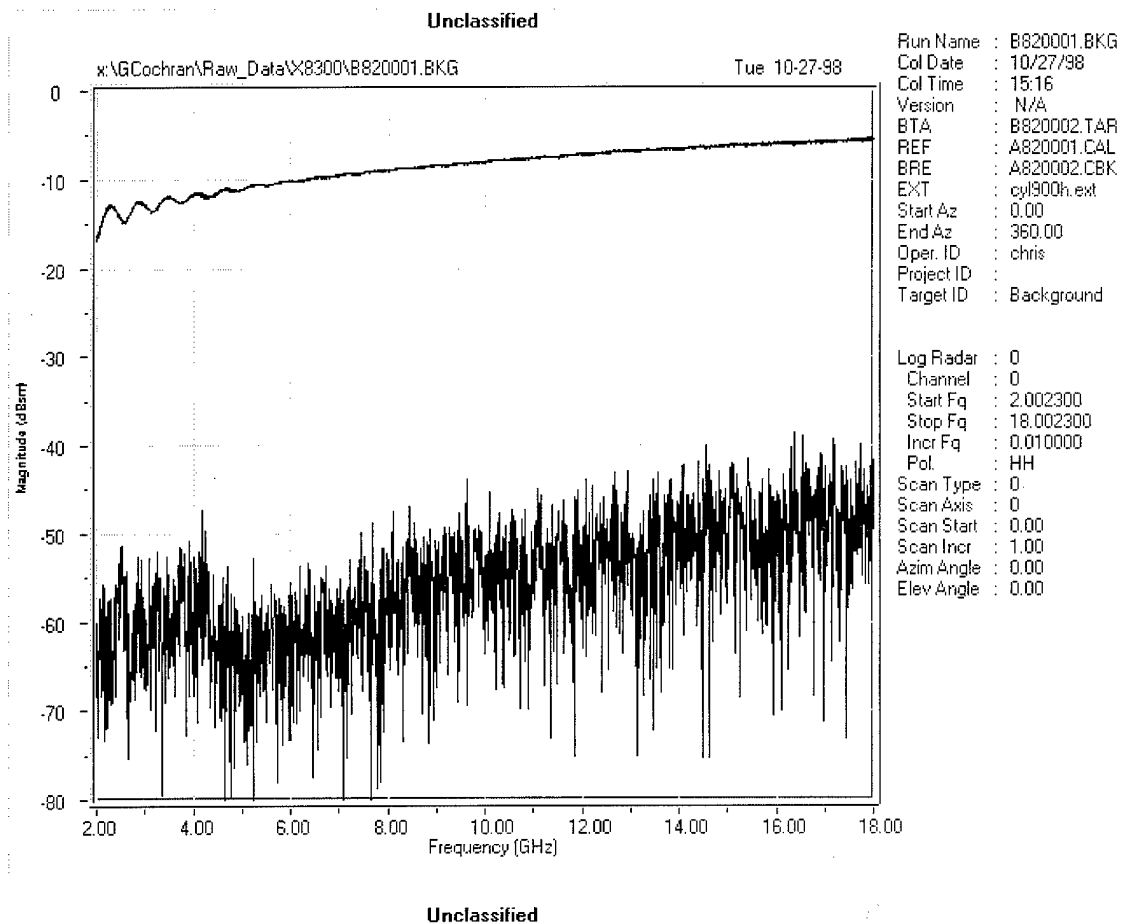


Figure 3-11 Double calibration comparison

3.3.3 Data

The raw data provided by the collection system for each measurement is divided into three columns. The first column is the azimuth angle. The second and third columns are the real (I) and imaginary (Q) channel data. The frequency is folded into the azimuth angle starting with 2 GHz and incrementing in 20 MHz steps to 18 GHz. Overall, each data set has 72090 rows of data with 801 rows of I and Q data for each frequency and angle. The RCS, in dBsm is then calculated using Equation (3.9) [19].

$$RCS = 10 \log_{10} |I^2 + Q^2| \quad (3.9)$$

Once the raw data was collected, two different software tools were used to generate the final data product. The first is a postprocessing package by Compuquest, used to generate 3D image plots. The other software tool is a MATLAB routine, written by Alan Buterbaugh of MRC, used to generate waterfall frequency plots of each configuration at specific angles and waterfall frequency plots of one angle for all configurations. Figure 3-11, Figure 3-13, and Figure 3-14 are examples of each data product. In chapter IV, these data products are used for analysis purposes.

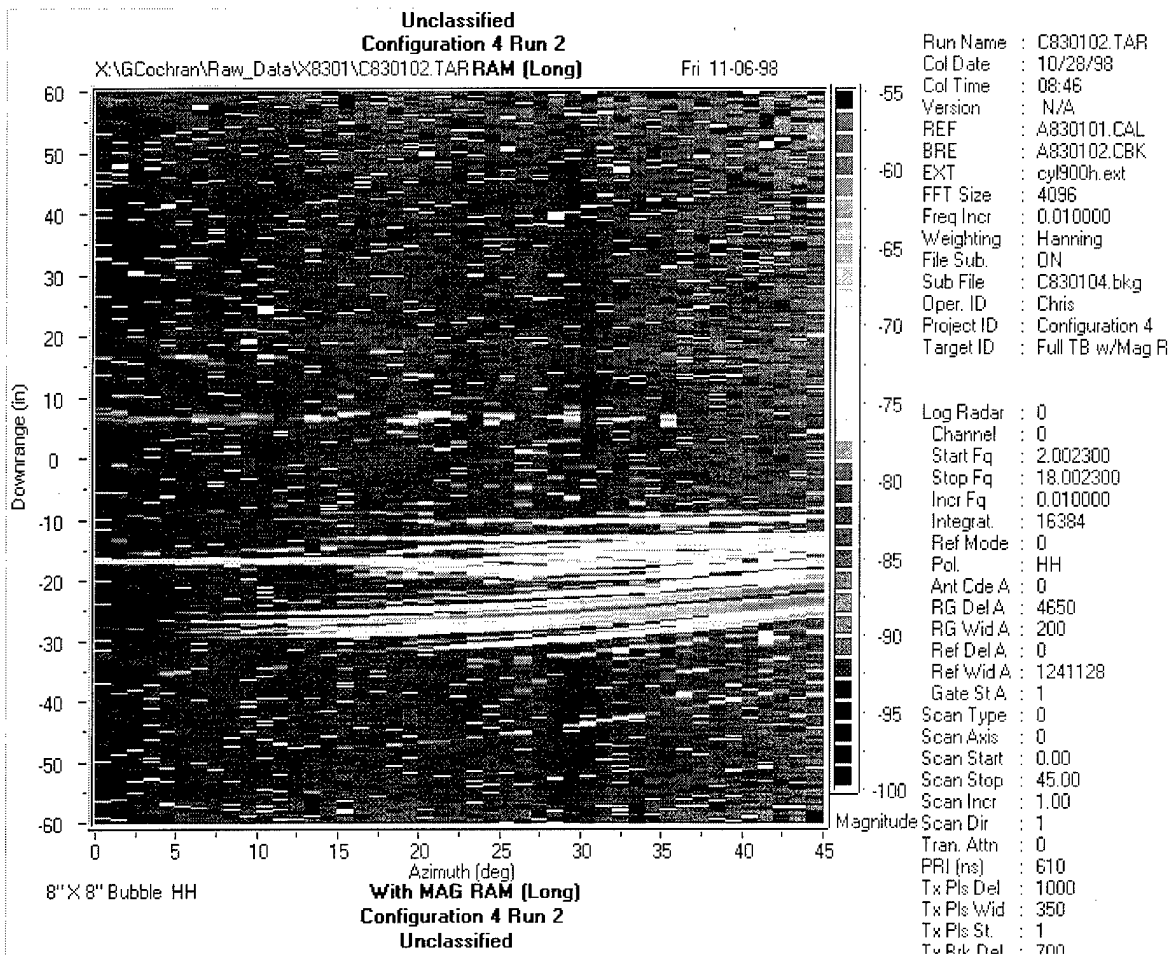


Figure 3-12 3-D Image Plot

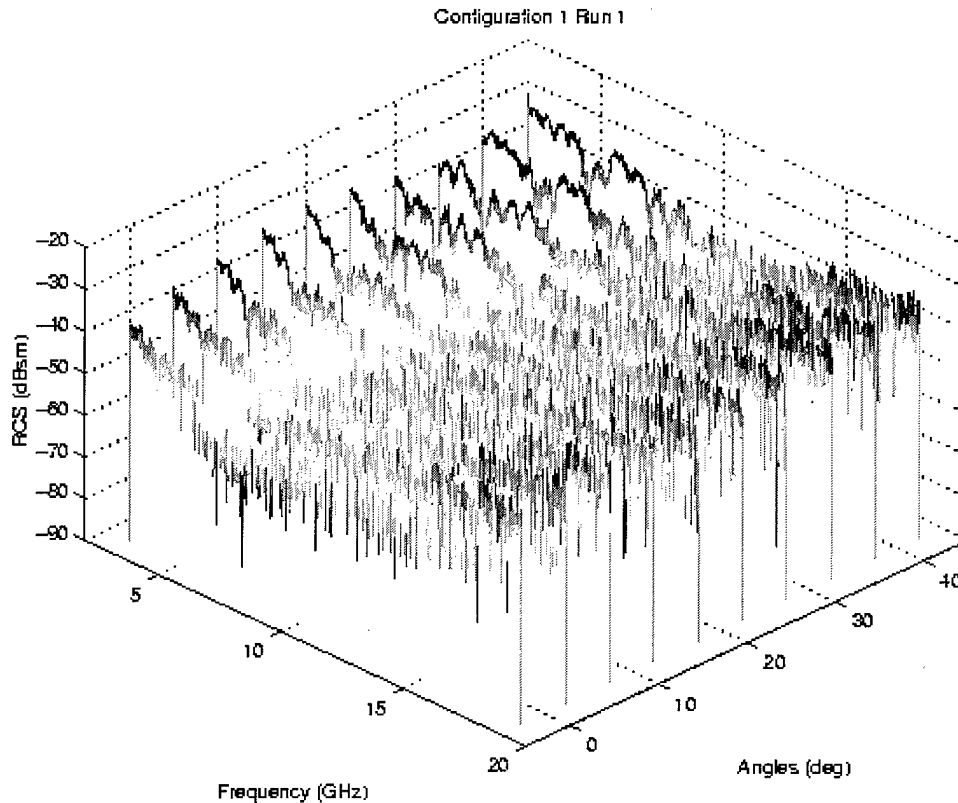


Figure 3-13 Waterfall Plot of a Single Configuration

3.3.4 Uncertainty

In Chapter II, the RCS measurement section discussed the three criteria necessary to obtain a meaningful measurement and seven methods used to achieve those criteria. In the real world, it is difficult to meet these criteria and therefore there is a certain amount of uncertainty in each measurement. AFRL/XPN has conducted an in depth range characterization [19] and Table 3-2 summarizes the most significant range uncertainties. For the purposes of this thesis, the total RCS uncertainty is approximately 1 dB.

Table 3-2 Compact Range Uncertainty

Target Uncertainty	dB
Average Illumination	neg
Background-Target Interactions	0.1
Cross Polarization	neg
Drift	0.08
Frequency	neg
Integration	neg
IQ Imbalance	neg
Near Field	neg
Noise Background	1
Nonlinearity	neg
Range	neg
Target Orientation	neg
Calibration Target	neg

3.4 JRMBOR RCS Simulations

The JRMBOR software was used to generate simulated RCS data. The purpose of the simulated data was to make a comparison with the measured data in order to explore the possibility of building a database of simulations. The JRMBOR software is a moment method code used for calculating monostatic and bistatic RCS for bodies of revolution [17]. The software is written in Fortran 90 and the simulations were run on the AFIT's network of Sun Sparc 20 workstations.

3.4.1 Procedures

As with the materials and RCS measurements, the procedures for running the simulations in JRMBOR are straightforward. The user's manual outlines the procedures for building an input file [17]. The highlights of building an input file are selecting the

proper moment method parameters, building the geometry input, and calculating the surface impedance.

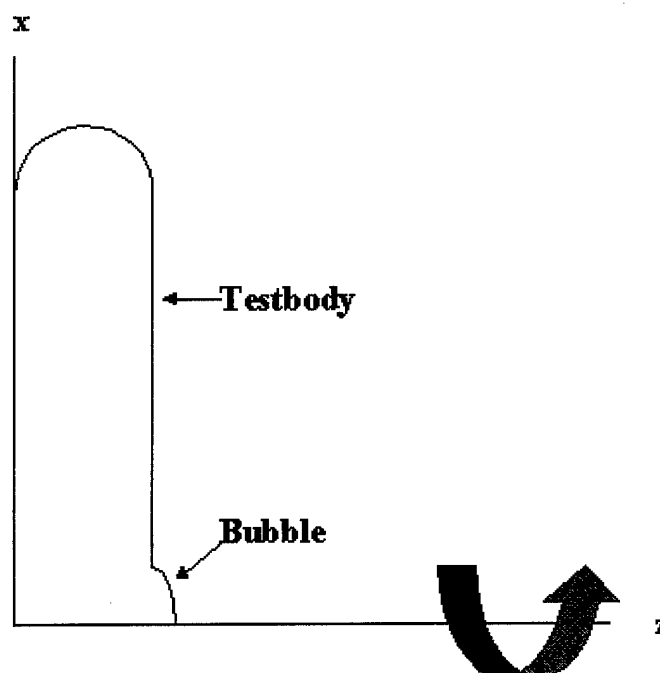


Figure 3-14 JRM BOR Testbody Geometry

Building the geometry was an easy task after deciding what the geometry should look like. The geometry input was specified two dimensionally in terms of lines and arcs relative to a xz axis system. JRM BOR then “rotates” the geometry around the z-axis to form a body of revolution (BOR). Ideally, the selected geometry should model the MRC testbody used for the actual measurements, however, and this was impractical. Therefore, a simpler testbody geometry was created. The testbody created for the simulations was a two-meter diameter disk, $\frac{1}{4}$ meter thick with a $\frac{1}{8}$ -meter radius of curvature. Specifying an appropriate arc on the front of the testbody created the bubble. The bubble was specified to be $\frac{1}{4}$ ” high and 8” in diameter (see Figure 3-14).

The final task in creating the input file was to calculate an appropriate surface impedance to account for the RAM coating. A physical layer of RAM was not modeled

in the geometry because JRMBOR has difficulty handling very thin RAM layers. In order to approximate the measured RAM coating, a surface impedance (Z_s) was calculated using a formula provided by Knott [9]:

$$\eta = \sqrt{\frac{\mu_r}{\epsilon_r}} \tanh(-ik_0 d \sqrt{\mu_r \epsilon_r}) \quad (3.10)$$

$$Z_s = 377(\eta) \quad (3.11)$$

One of the limitations of the JRMBOR software is that depending on the hardware platform and input frequency, it can take a long time to calculate RCS values. The runtimes ranged from 8 hours to two weeks. Therefore, only a very limited data set was collected. The data set consisted of one angle setting (25° off grazing) at six separate frequencies. The frequency range was 2-7 GHz in 1 GHz steps. This frequency range was selected because it is the range where the interesting response is in the measured data. Also since job runtime increases with frequency the lower frequencies provided reasonable runtimes

Another limitation of the JRMBOR software is that it will not accept a vector value for the surface impedance. Therefore, since surface impedance varies as a function of frequency, 12 separate job files were created. Two files were created for each frequency and surface impedance, with one file representing the case of a testbody with a bubble and the other file representing the case of a testbody without a bubble. Additionally, the material measurements were from 4-18GHz; therefore, it was necessary to linearly approximate the relative permittivity and relative permeability values from 2-4GHz.

3.4.2 Data

After all of the data was generated, the E-field values from each file, 2-7GHz respectively, were vector subtracted to produce E-field values for the bubble. Table 3-3 contains a representative sample of values (2 GHz points) for the simulated absolute RCS of the bubble. The bubble row represents the vector subtraction of the E-field values (I and Q data) for the testbody with and without the bubble. Using Equation (3.9), the RCS values in dBsm were calculated.

Table 3-3 Representative Sample of JRMBOR Data

	I	Q	RCS (dBsm)
Testbody with bubble	0.4921	-0.5121	-2.97
Testbody without bubble	0.4888	-0.5044	-3.07
Bubble	0.0033	-0.0077	-41.54

3.5 XpatchF RCS Simulations

Like JRMBOR, the XpatchF software was used to generate simulated RCS data. The E-field values (I and Q data) from the low RCS NASA almond were needed. These values were needed for demonstrating an RCS signature perturbation caused by a bubble. In Chapter IV, the almond's E-field values are coherently and incoherently added to a RAM bubble's E-field values to effectively produce an almond with a bubble on it.

3.5.1 Procedures

Generating the E-field values from the almond required a slight modification to the pre-built input file. The first modification required adding a layer of RAM to the PEC almond. The layer was specified in terms of thickness, relative permeability, and relative permittivity. The second modification was moving the almond's phase center so that it matched the phase center of the measured bubbles.

Once the modifications were made, the input files were run on the Silicon Graphics machines in AFIT's Hawkeye lab. The data collected was the nose-on RCS of the almond. The frequency range was from 2-10 GHz in 0.5 GHz steps for a total of 17 data points.

3.5.2 Data

The output of XpatchF was the E-field values for the almond testbody. Table 3-4 provides a representative sample for the 2 GHz case.

Table 3-4 Representative Sample of Almond Data

I	Q	RCS(dBsm)
0.0000004815	0.002594	-51.72

3.5.3 Assumptions

The material measurements were from 4-18GHz; therefore, it was necessary to linearly approximate the relative permittivity and relative permeability values from 2-4GHz.

3.6 Summary

Four distinct data sets were generated in this thesis. The first data set is the material properties (μ_r and ϵ_r) of the RAM. The second data set is the measured RAM bubble RCS database of 10 different configurations and pertinent noise + clutter measurements. The third is the simulated RAM bubbles generated from the JRMBOR software. The last data set is the E-field values for the NASA-almond testbody. For each data set, the equipment, procedures, data examples and uncertainty/assumptions were discussed.

Chapter 4 Analysis and Applications

The primary purpose of this chapter is to analyze the measured RCS data and then use the data to build an application. The application is a linear regression model that predicts the RCS of bubbles in RAM. The chapter is divided into five sections. The first section analyzes the material properties showing the attenuation caused by the RAM. The second section is an RCS analysis of the measured data to characterize the absolute RCS of the RAM bubbles. The third section compares the results of the JRMBOR simulation with the measured RCS data. The fourth section presents the process of building a linear regression model from the measured RCS database and then uses the model for further analysis of the RAM bubbles. The fifth section demonstrates the effects of a RAM bubble on a low RCS target. This demonstration shows the detrimental effects of a RAM bubble on the RCS signature and radar detection range of the target.

4.1 Introduction

Chapter IV is the culmination of the combined measurement and simulation efforts of Chapter III. The analysis contained in Chapter IV provides solutions to the problems posed in Chapter I. Chapter IV also explores other avenues of the research process by analyzing the RAM's attenuation, simulated results of JRMBOR, and demonstrating the bubble's effects on a target's signature. In Chapter IV, only selected data sets are analyzed with the full sets of data available in the appendices.

4.2 RAM Analysis

The primary objective of RAM is to attenuate incident RF energy and therefore reduce the RCS return of the object. The amount of RF energy attenuated is quantified

by calculating the Return Loss (RL). The RL is a measure of the RAM's attenuation ability and provides insight into evaluating the RAM's performance over a range of frequencies. Insight into the RAM's performance is necessary for fully analyzing the measured RCS results.

According to Knott [9], the procedure for calculating the RL of a normally incident wave onto a flat metal surface coated with a layer of dielectric is to first calculate the normalized input impedance, η ,

$$\eta = \sqrt{\frac{\mu_r}{\epsilon_r}} \tanh(-ik_0 d \sqrt{\mu_r \epsilon_r}) \quad (4.1)$$

where μ_r and ϵ_r are the relative permeability and permittivity respectively, k_0 is the free space wavenumber, and d is the material thickness. The normalized input impedance is inserted into Equation (4.2) to calculate the reflection coefficient.

$$RL = \frac{\eta - 1}{\eta + 1} \quad (4.2)$$

Finally, the reflection coefficient is converted to decibels by Equation (4.3).

$$|RL|(dB) = 20 \log_{10} |RL| \quad (4.3)$$

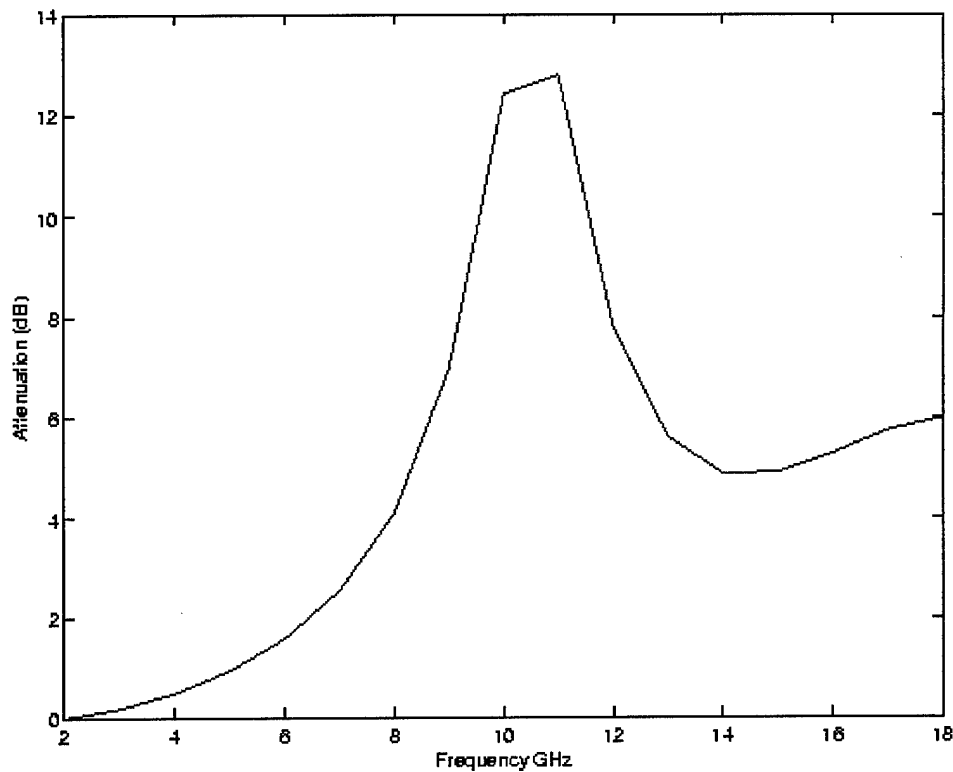


Figure 4-1 RAM Attenuation Versus Frequency

Figure 4-1 depicts the frequency behavior of the RAM used in this thesis. The RAM has maximum attenuation at approximately 11 GHz and optimum performance in the band from 8-12 GHz. The smallest attenuation is at the lower frequencies, 2-6 GHz. From this plot, one might expect the RAM bubble to have a higher RCS at the lower frequencies and a low RCS at the higher frequencies. However, it is necessary to view the data in the 2-4 GHz range cautiously because those data points were linearly approximated from the measured data.

4.3 RCS Analysis of Measured Data

One of the two primary goals of this research was to characterize the absolute RCS of bubbles in RAM. The purpose of this section is to analyze the measured RCS data. The analysis explains the amplitude of the scattering as it varies with frequency. This is accomplished by analyzing the waterfall plots of RCS versus frequency and the 3-D image plots. However, before drawing any conclusions from the measured data it is necessary to first justify that legitimate data was recorded. In other words, ensuring the measured data is the RCS return from the RAM bubbles and not from some other source on the testbody or in the range.

Ensuring the data was measured properly is accomplished by answering several questions, including:

1. What is the noise + clutter floor of the range?
2. Is the bubble scattering in the expected location in the images?
3. Are there any other scattering centers in the images?

By analyzing Figure 3-11, Figure 4-2, Figure 4-3, and Figure 4-4, these questions are answered. Figure 4-2 is an image plot of the range noise. This plot was generated by taking two back to back measurements of an undisturbed testbody.

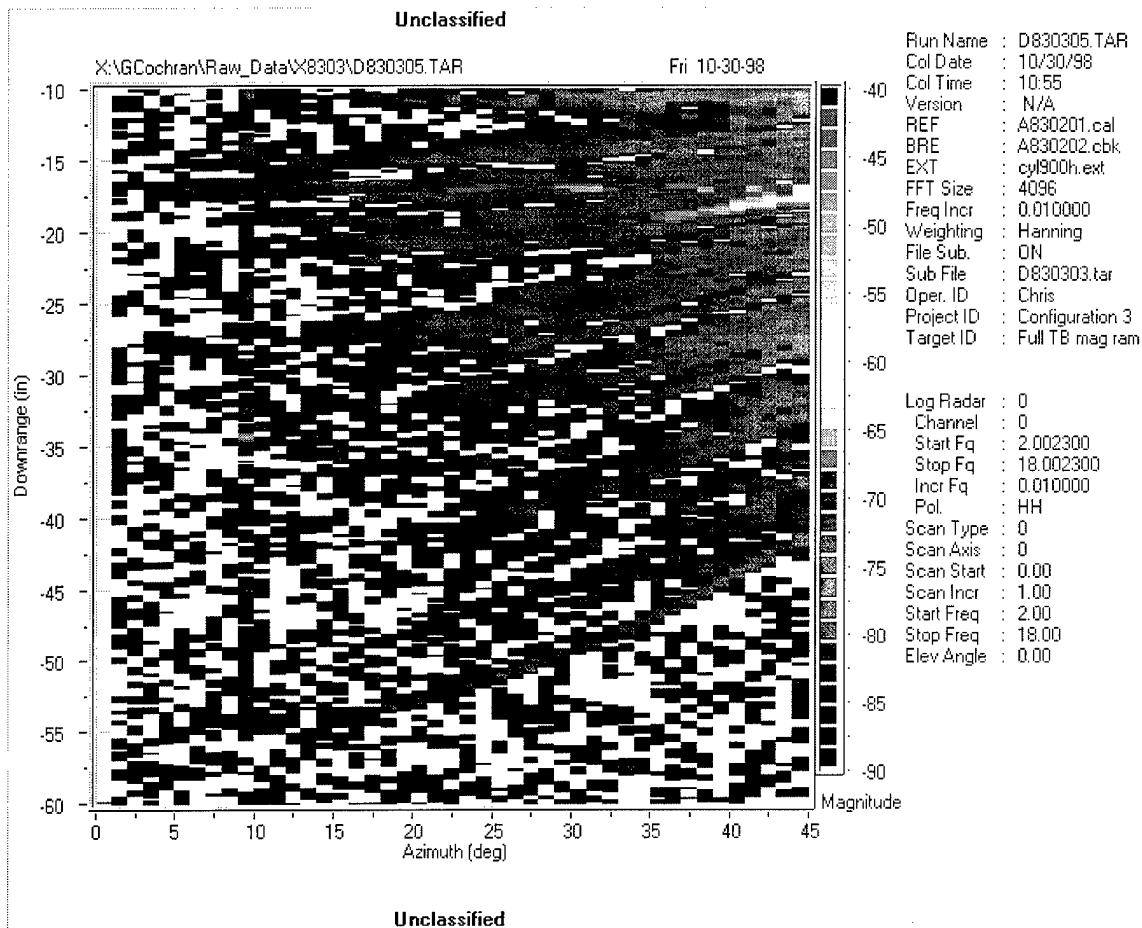


Figure 4-2 3-D Image of Range Noise + Clutter

The first question is answered by analyzing Figure 3-11. The bottom of Figure 3-11 is a frequency plot of the range noise + clutter level. Skolnik [21:470], defines clutter as “an unwanted radar echo.” In this case, the clutter is caused by imperfections in vector subtraction and back wall reflections that are not fully gated out. The range noise + clutter level is the limit of the measurement system and from Figure 3-11 that limit is approximately -65 dBsm at 2 GHz and approaches -45 dBsm at 18 GHz. This means detecting a target below these values is not possible. Figure 4-2 is the time domain counterpart to Figure 3-11 and shows where the noise and clutter does not

subtract out perfectly. The noise + clutter range for the image plots is approximately -70 to -75 dB.

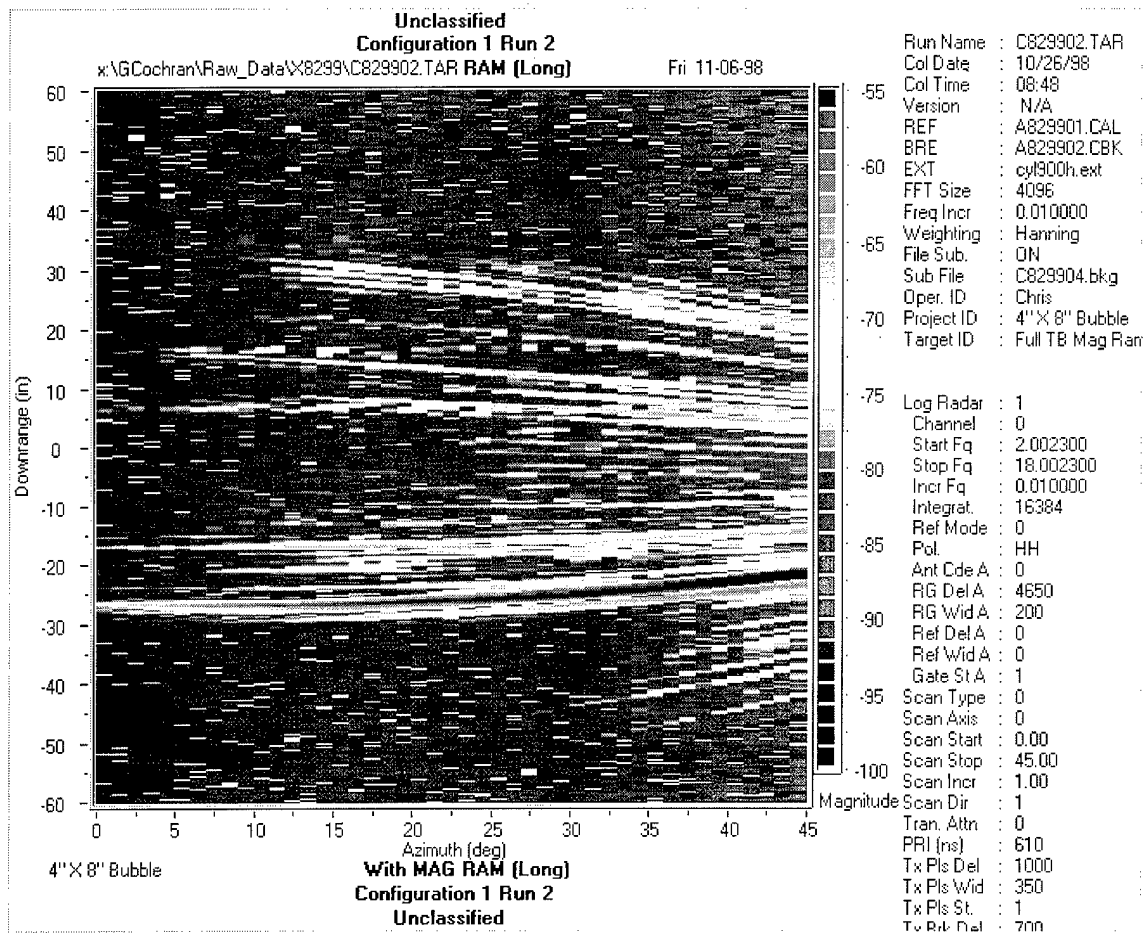


Figure 4-3 3-D Image of Configuration 1 Run 2 (4"x8" bubble)

The second question is answered analyzing Figure 4-3. The largest intensity (dark orange and black lines) is approximately -26" downrange. This is the expected bubble location and is verified in Figures 3-7 and 3-8. These figures show the center of each bubble is located -26" from the center of the testbody.

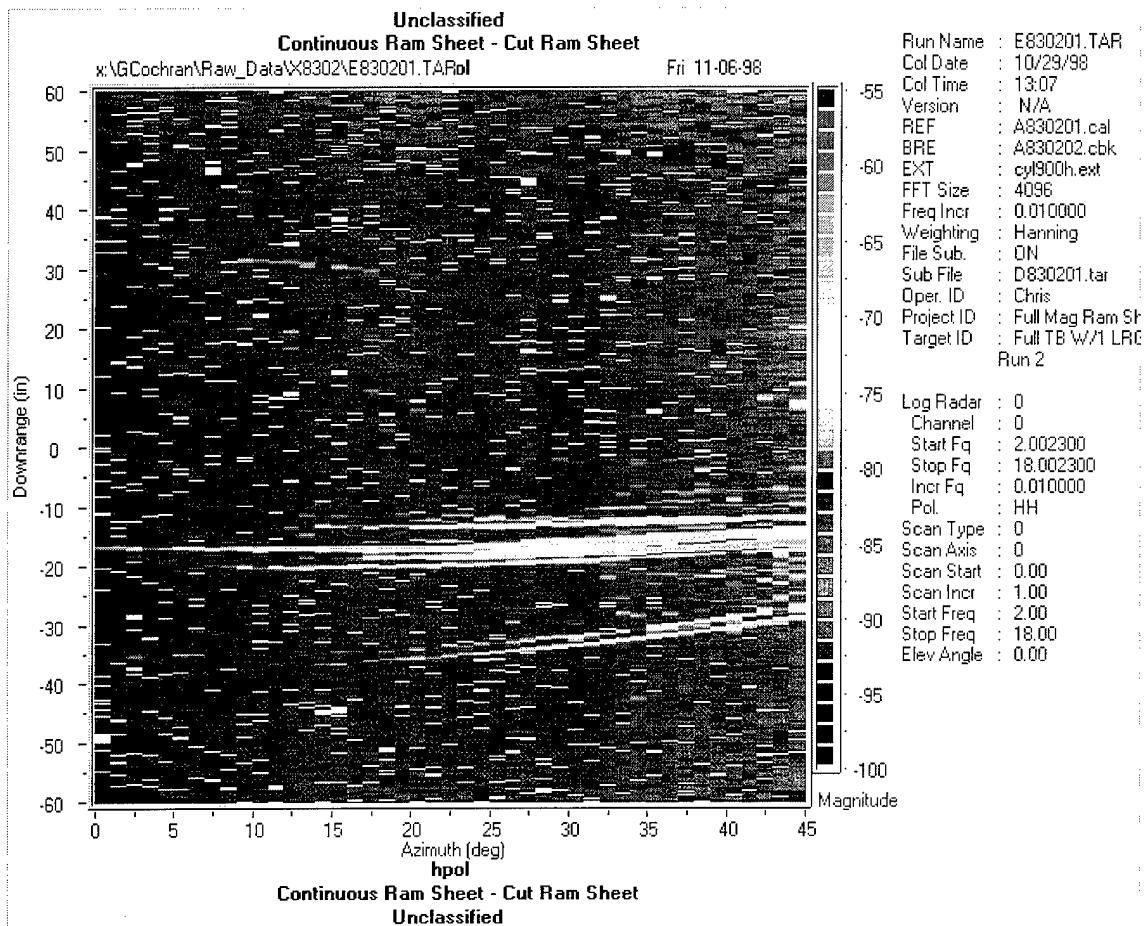


Figure 4-4 3-D Image of Scattering from Cuts in the RAM sample

The third question is answered by explaining what the yellow intensity streaks are in Figure 4-3 and Figure 4-4. Figure 4-4 is a measurement of the return from imperfectly realigning the edges of the cut when the RAM is peeled back to insert a bubble. From Figure 4-4 the return caused by peeling the RAM is approximately -70 to -75 dB, which is in the noise + clutter range. Therefore, the return caused by peeling the RAM is classified as clutter. This conclusion allows one to answer the third question. The other scattering centers, if any, are at the range noise + clutter level and are not detectable.

The above analysis gives confidence that the measured data is the RCS of the bubbles and not unwanted signals from the range. Consequently, the frequency domain

waterfall plots represent the absolute RCS of the bubbles in RAM. Analysis of the waterfall plots will explain the amplitude of the scattering as it varies with frequency.

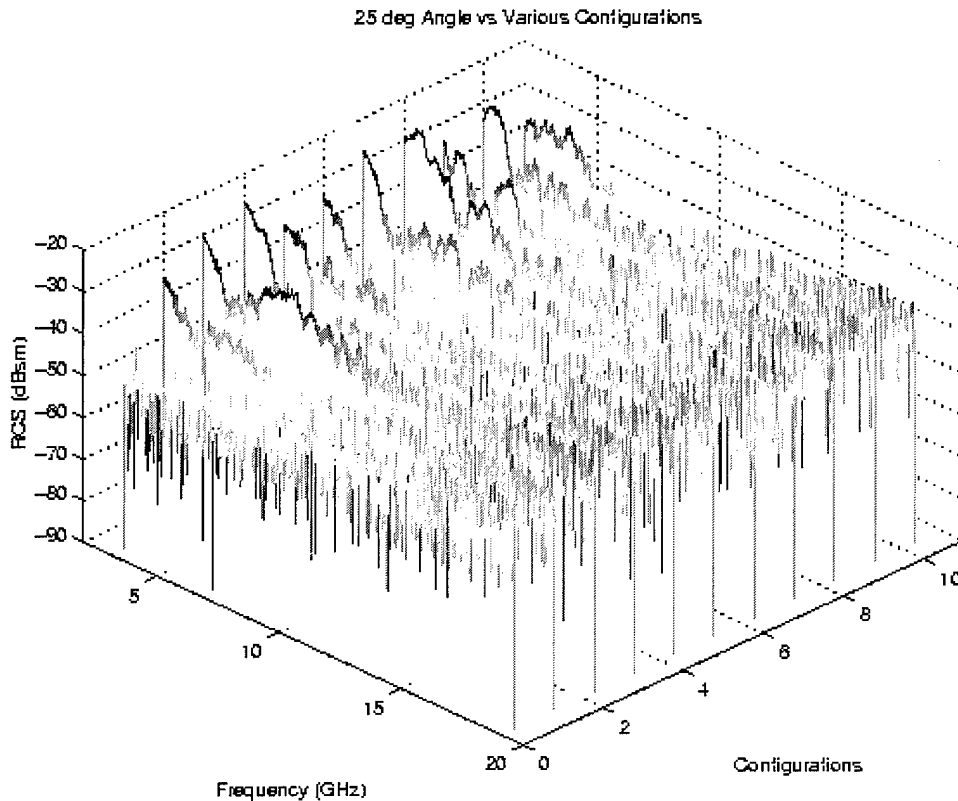


Figure 4-5 Waterfall plot of the Various Configurations at 25 degrees

Figure 3-7 and Figure 3-8 depicts the non-uniformity and complexity of the geometry of the RAM bubbles. The purpose of Figure 4-5 is to demonstrate the uniqueness in RCS of each RAM bubble configuration. The uniqueness is a function of the non-uniformity and complexity of the bubble geometry and the inherent variability of RCS measurements. The configurations are plotted according to Table 3-1. For instance, on all the waterfall plots the return of configuration 1 corresponds to Bkg4 (the range noise + clutter) and configuration 10 corresponds to c5r1 (Configuration 5 Run 1).

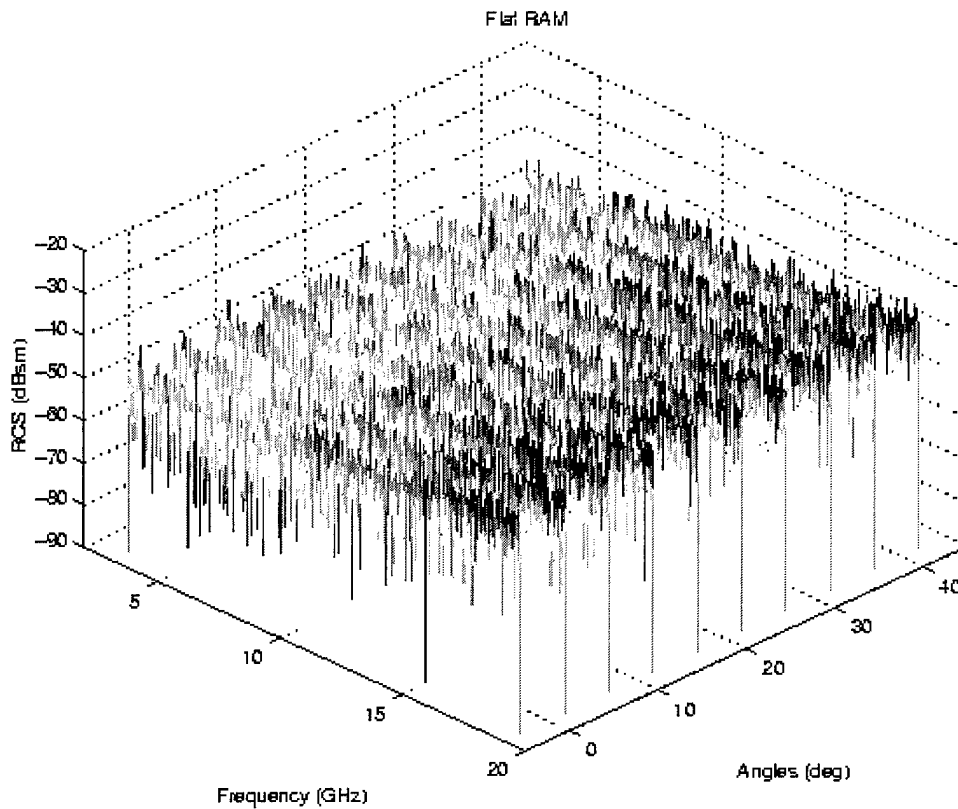


Figure 4-6 Waterfall Plot of Range Noise + Clutter

Figure 4-6 is a frequency domain plot of the range noise + clutter levels and is the frequency domain counterpart to Figure 4-2. Figure 4-6 serves as a baseline for demonstrating the effects of a bubble in RAM. Figure 4-7 is a plot of the RCS versus frequency for Configuration 3 Run 1. By comparing Figure 4-6 and Figure 4-7, the effects of the bubble are obvious.

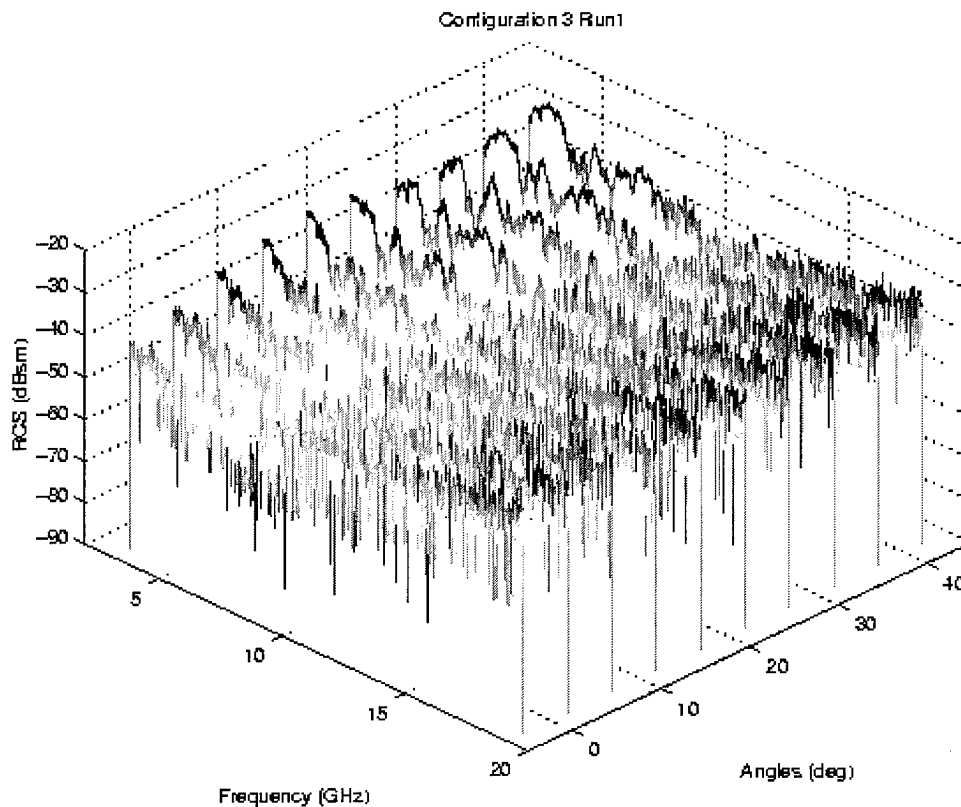


Figure 4-7 Waterfall plot of Configuration 3 Run 1 (4"x6" bubble)

In terms of angle dependence, Figure 4-7 shows how a RAM bubble increases the RCS at all angles, from grazing incidence (0°) to 45° . At near grazing angles the RCS increase due to the bubbles is 10-15 dB. Additionally, the RCS increases as the angle increases away from grazing incidence. At the higher angles, the RCS increase due to the bubbles is 10-20 dB. The RCS increase is relative to the noise plus clutter measurement of the range. The range of absolute RCS values for the various bubble sizes can range from -55 dBsm to -25 dBsm.

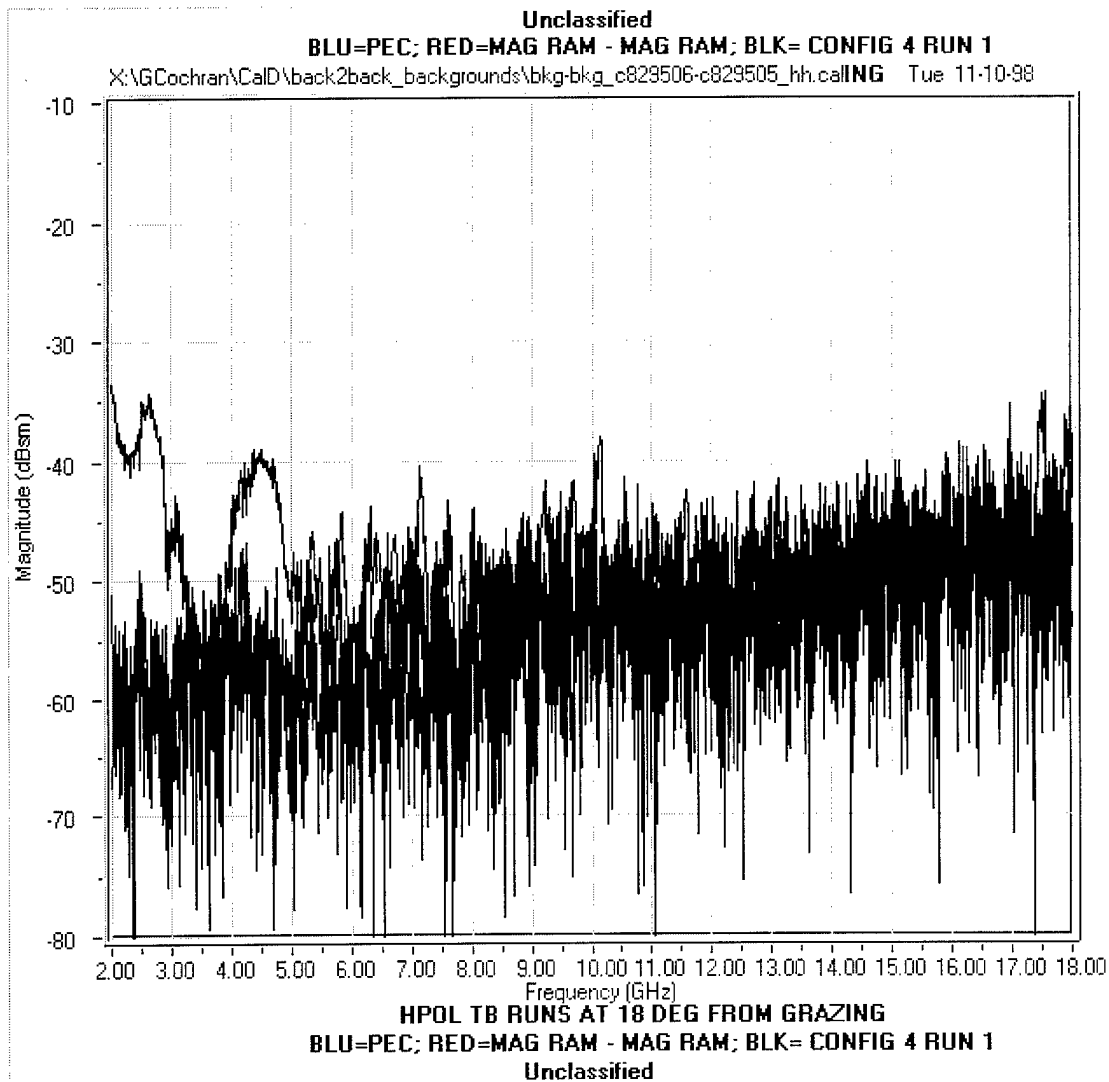


Figure 4-8 RCS Versus Frequency

In terms of frequency dependence, the highest RCS is at 2-3GHz and tapers down as frequency increases. This result corresponds with the conclusions from the RAM attenuation analysis. In addition, at all angles, by 10GHz the bubble RCS matches the range noise + clutter level. Figure 4-8 provides an example of this effect. Therefore, from 10-18GHz it is impossible to speculate on the bubble RCS because it is in the noise + clutter. The only conclusion to draw regarding the bubble RCS at higher frequencies is that it is not higher than the noise + clutter level.

4.4 RCS Analysis of Simulated Data

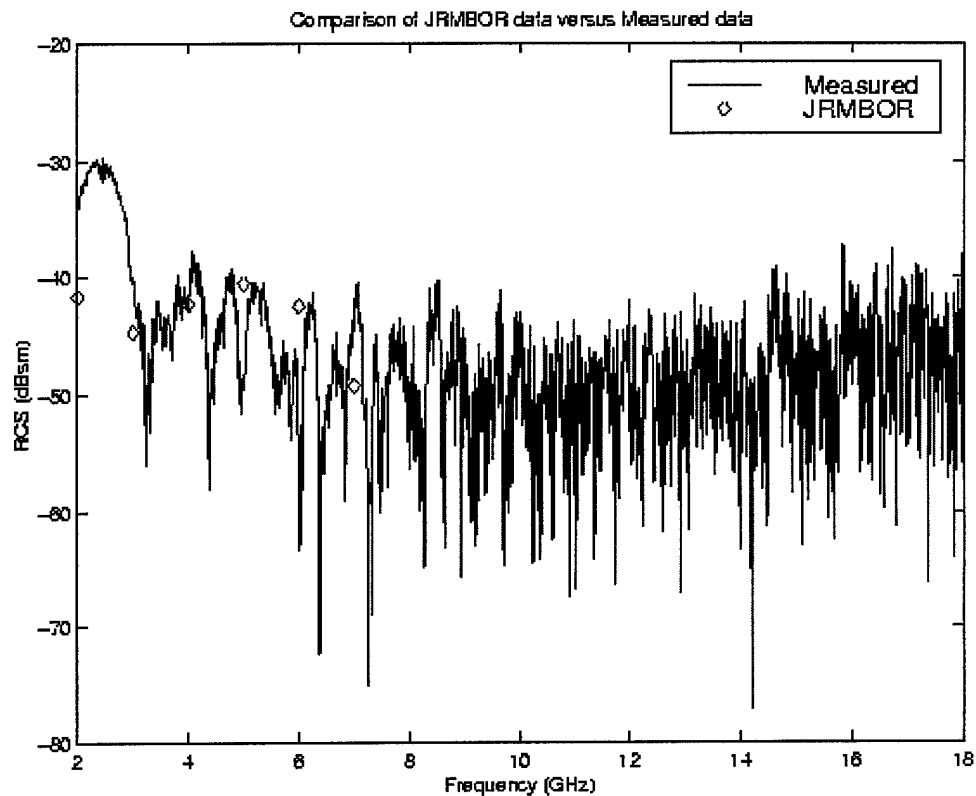


Figure 4-9 Comparison of Measured RCS and Simulated RCS (JRMBOR)

The simulation of a RAM bubble was a secondary goal of this thesis. The simulations were necessary to pursue all available avenues of research. Simulating the RAM bubbles permits the opportunity for exploring the viability of using simulations as an alternative to measuring data. If the simulations match the measurements then simulations could serve as a data generation capability if measurement facilities are not available. Simulations could also serve as a complementary method ensuring the measurements were performed properly. Finally, simulations could give insight to what one might expect before measurements are performed and precise control over geometry. Figure 4-9 is a comparison of the measured and simulated RCS data for approximately

the same size bubble (8"x8") at 25° off grazing incidence. Six points represent the simulated data. These points are from 2-7GHz in 1GHz increments. The simulated data approximately matches the measured data. The one data point to scrutinize is at 2GHz. There are several possible explanations for why the 2 GHz simulated point does not come close to matching the 2 GHz measured point. The explanations highlight the differences between the measurement and simulation configurations. The material measurements were from 4-18 GHz; therefore, it was necessary to linearly approximate the relative permittivity and relative permeability values for 2-4 GHz. It is possible the linear approximation is an incorrect approximation for those values. Another possibility for the difference is that the simulated testbody was entirely covered in RAM whereas the MRC testbody was only partially covered with a RAM strip. The final possibility is that the 2GHz simulation happened to fall on a null in the field that produces a small return.

In Figure 4-9 the majority of the simulated points approximately match the measured points. This lends credibility to using JRMBOR as a tool for generating simulated data. Before using simulations as an actual data generation tool, further testing is recommended. One specific recommendation is to resample at a higher rate between 2-4 GHz. This might give further information needed to explain why the 2 GHz point does not match. Additionally, if JRMBOR is used as a tool for generating large data sets, a much faster computer is needed to make the collection effort efficient, particularly at higher frequencies.

4.5 The Prediction Equation

The second primary goal of this thesis is to build an empirical based RAM bubble RCS prediction equation with inputs of angle, frequency and bubble geometry. A subset

of the measured RCS database serves as an input to the linear regression process for generating the prediction equation. The purpose of this section is to describe the iterative process of building the prediction equation and then validate the equation's prediction ability by comparing predictions to measured data. Finally, the equation is used as a tool to analyze the relationship between bubble RCS and bubble length and width.

Building a prediction equation is an iterative process of defining a model of independent variables, "fitting" the model to determine parameter estimates and residuals, and then analyzing the parameter estimates and residuals. The reason for the iterative process is to build the best possible model.

Before starting this process, a data file is built containing the measured data in terms of RCS, angle, frequency, and bubble geometry for each configuration. The data file consists of only a subset of the entire measured RCS database. Using the entire database was unnecessary and impractical. Also, the granularity in theta is justified due to the primarily linear relationship to RCS. Additionally, data not used to fit the model is needed to perform proper model validation. The data file consists of each configuration in terms of frequency from 2-10GHz in 20 MHz increments, and angle from 0°-45° in 5° increments. The RCS analysis section determined that only range noise + clutter was in the 10-18 GHz range. Therefore, those frequencies were excluded. This data file was input into the Linear Regression software package SAS-JMP.

In the process of determining the final model, many trial models were built. Additionally, the response variable (RCS) was transformed several times. The first transformation is from dBsm to square meters, then to meters and finally to a logistic transform. The logistic transform (logit_rcsm) is:

$$\text{logit_rcsm} = -\ln\left(\frac{p}{1-p}\right) \quad (4.4)$$

$$p = \frac{\text{rcs}}{\max(\text{rcs}) + \delta} \quad (4.5)$$

where *rcs* is the RCS in meters and δ is a small value to allow $0 < p < 1$. The logistic transform is used to undo a flooring effect in the data and therefore helps to stabilize the model's variance [16].

To evaluate the final model a comparison of appropriate model statistics and model adequacy checking plots is made with the pre-final model. The model statistics compared are the R^2 , Root Mean Square Error (RMSE), and the parameter estimates. The model adequacy checking plots compared are the residuals versus Logit_rcsm, histogram of residuals, quantile and outlier box plot of residuals, and normal quantile plots of residuals.

In Table 4-1 and Table 4-2 R^2 is the Coefficient of Determination and lies in the interval from 0-1. R^2 is a measure of the variability accounted for in the model and is used to compare one model to another. An R^2 of one would mean that all of the variability of the data is accounted for in the model. Therefore, the higher a model's R^2 value the better it fits the data. In this case, the pre-final model's $R^2 = 0.541619$ whereas the final model's $R^2 = 0.584151$. This is one indication that the final model is a better model than the pre-final model. The adjusted R^2 (\bar{R}^2) is similar to R^2 except it is slightly modified to attempt to account for an increased number of independent variables added to the model.

Table 4-1 Pre-final Model

Response: logit_rcsm				
Summary of Fit				
RSquare	0.541723			
RSquare Adj	0.541619			
Root Mean Square Error	0.813516			
Mean of Response	2.742826			
Observations (or Sum Wgts)	87998			
Parameter Estimates				
Term	Estimate	Std Error	t Ratio	Prob> t
Intercept	1057.0512	41.07153	25.74	<.0001
theta	0.0120187	0.003142	3.83	0.0001
theta*sqrt_ome	-0.011064	0.001283	-8.63	<.0001
length	-0.707597	0.015516	-45.61	0.0000
theta*length	-0.000535	0.000581	-0.92	0.3573
sqrt_ome*length	0.2567819	0.006334	40.54	0.0000
theta*sqrt_ome*length	-0.001367	0.000237	-5.76	<.0001
width	-1.012877	0.028192	-35.93	<.0001
theta*width	-0.007128	0.001056	-6.75	<.0001
sqrt_ome*width	0.3721523	0.011509	32.34	<.0001
theta*sqrt_ome*width	0.0004182	0.000431	0.97	0.3321
length*width	0.1903429	0.004728	40.26	0.0000
theta*length*width	-0.000322	0.000177	-1.82	0.0687
sqrt_ome*length*width	-0.070232	0.00193	-36.39	<.0001
theta*sqrt_ome*length*width	0.0005326	0.000072	7.37	<.0001
sqrt_omegabin	-2915.882	113.8796	-25.60	<.0001
sqrt_ome*sqrt_ome	3305.5932	129.7964	25.47	<.0001
sqrt_ome*sqrt_ome*sqrt_ome	-1966.597	77.86346	-25.26	<.0001
sqrt_ome*sqrt_ome*sqrt_ome*sqrt_ome	648.39286	25.93898	25.00	<.0001
sqrt_ome*sqrt_ome*sqrt_ome*sqrt_ome*sqrt_ome	-112.439	4.551906	-24.70	<.0001
omegabin3	8.017896	0.328896	24.38	<.0001

The estimates column is also an important factor to understand. The estimate is the unknown parameter coefficient (β) generated by the LSE process. A large estimate indicates the parameter is a highly significant contributor in the model whereas a lower estimate indicates the parameter is a less significant contributor in the model. The term column represents the independent variables used to fit the model and the response (logit_rcsm) represents the dependent variable.

Table 4-2 Final Model

Response: logit_rcsm				
Summary of Fit				
RSquare	0.584151			
RSquare Adj	0.584064			
Root Mean Square Error	0.740437			
Mean of Response	2.716641			
Observations (or Sum Wgts)	86412			
Parameter Estimates				
Term	Estimate	Std Error	t Ratio	Prob> t
Intercept	1001.471	37.61553	26.62	<.0001
theta	0.0093725	0.002179	4.30	<.0001
theta*sqrt_ome	-0.009974	0.000903	-11.05	<.0001
length	-0.717204	0.007652	-93.73	0.0000
sqrt_ome*length	0.2595045	0.003274	79.25	0.0000
theta*sqrt_ome*length	-0.001492	0.000044	-34.12	<.0001
width	-0.934972	0.017868	-52.33	0.0000
theta*width	-0.010025	0.000499	-20.09	<.0001
sqrt_ome*width	0.3383834	0.007452	45.41	0.0000
theta*sqrt_ome*width	0.0017801	0.000215	8.29	<.0001
length*width	0.1808437	0.002333	77.51	0.0000
sqrt_ome*length*width	-0.065963	0.000998	-66.08	0.0000
theta*sqrt_ome*length*width	0.0003642	0.000013	27.30	<.0001
sqrt_omegabin	-2775.993	104.2937	-26.62	<.0001
sqrt_ome*sqrt_ome	3162.6282	118.867	26.61	<.0001
sqrt_ome*sqrt_ome*sqrt_ome	-1890.566	71.3051	-26.51	<.0001
sqrt_ome*sqrt_ome*sqrt_ome*sqrt_ome	626.17049	23.75367	26.36	<.0001
sqrt_ome*sqrt_ome*sqrt_ome*sqrt_ome*sqrt_ome	-109.0511	4.168351	-26.16	<.0001
omegabin3	7.8072637	0.30118	25.92	<.0001

The Prob>|t| value in the parameter estimates table is also important to analyze. If a particular term's Prob>|t| is >0.0001 then that term is not a significant factor in the model and therefore warrants deletion. The final model has two fewer terms than the pre-final model, which reduces the residual's variance. The reduction in variance is observed in the model root mean square error (RMSE). The final model's RMSE is lower than the pre-final model's RMSE.

The next step in the iterative model building process is to observe the behavior of the residuals. Residuals are defined as the difference between the actual measured data point used to develop the model and the value that is modeled for that data point. Montgomery [16] explains that one can view residuals, as realizations of the model errors

or a measure of the variability not explained by the model. The first comparison to make is Residuals versus Logit_rscm plots of the final model and the pre-final model.

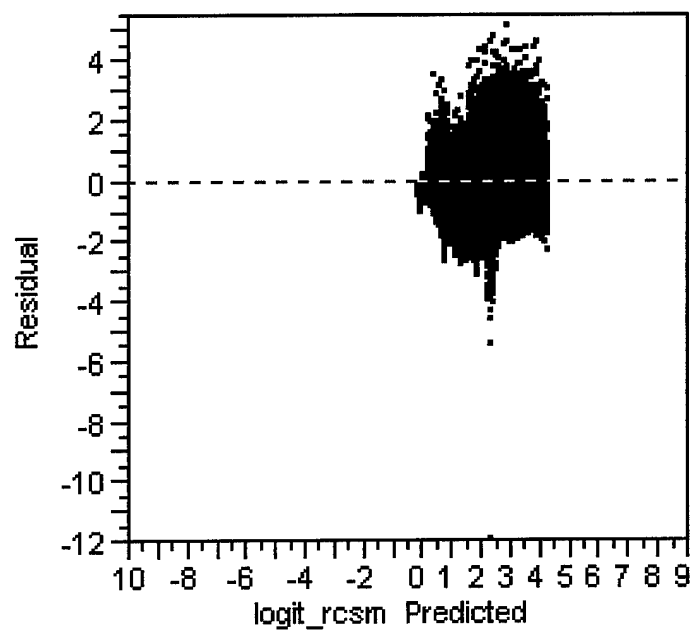


Figure 4-10 Residuals versus Logit_rscm Pre-final Model

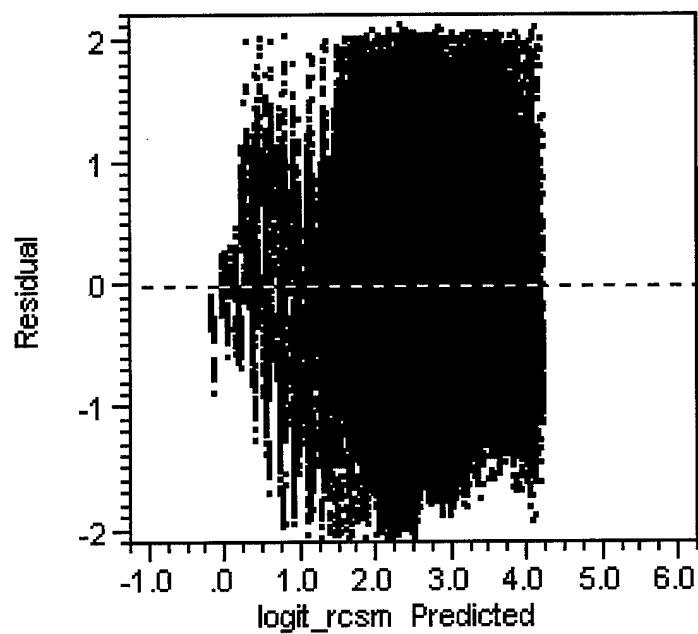


Figure 4-11 Residuals versus Logit_rscm Final Model

Comparing Figure 4-10 and Figure 4-11, Figure 4-10 does not have as much symmetry as the pattern in Figure 4-11. This indicates some nonconstant variance of the residuals in the pre-final model. Nonconstant variance is a violation of one of the basic assumptions that allow for statistical inference.

The next step involved in the residuals analysis is to analyze the histogram of residuals, quantile and outlier box plot of residuals, and normal quantile plots of residuals. These plots help to check the assumptions about the errors in the model.

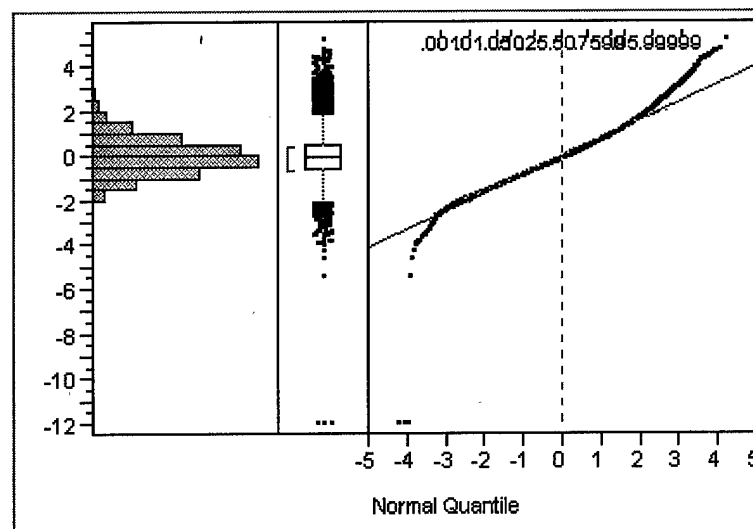


Figure 4-12 Histogram, Quantile, and Outlier, and Normal Quantile Plots of the Pre-final Model Residuals, Respectively

Figure 4-12 explains the behavior of the pre-final model residuals. The first feature to notice is that the histogram of residuals plot is not very normal. The second feature is the large number of outlier's (shaded areas on top and bottom) on the quantile and outlier plot. The final feature is the tails on the normal quantile plot. If the residuals came from a normal distribution, we would expect the normal quantile plot to be linear.

One method used for dealing with outliers is to discard them. This is an iterative process within itself. The procedure followed for dealing with outliers for this model was to use Equation (4.6) as a decision aid in identifying the outlier points.

$$\text{ignore if } |e_i| > 2.5\sqrt{MSE} \quad (4.6)$$

The translation of Equation (4.6) is that it defines an outlier as any residual value that is greater than 2.5 standard deviation away from the residuals mean.

A total of 1586 of data points were identified as outliers and excluded. This represents only 1.8% of the total data. The outliers were extreme observations in the range of -60dBsm to -90 dBsm. This does not mean that all the points in that range were excluded, only those points that were identified as outliers.

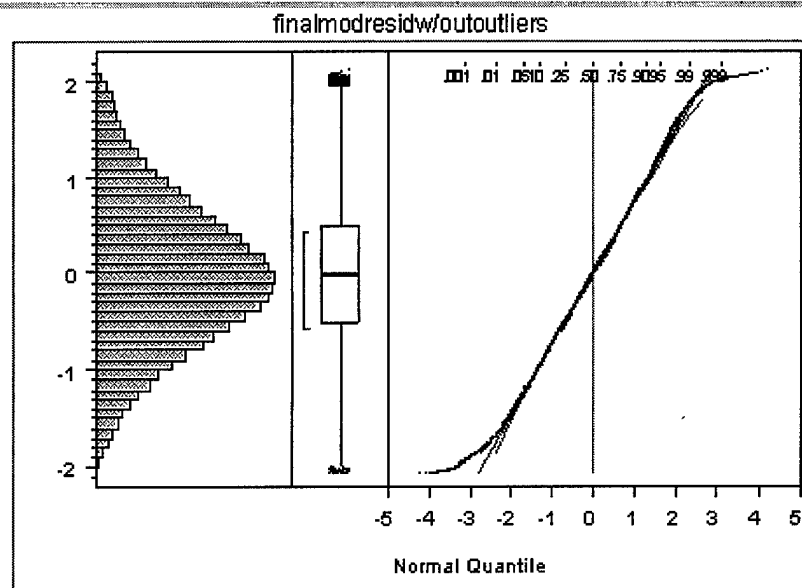


Figure 4-13 Histogram, Quantile, and Outlier, and Normal Quantile Plots of the Final Model Residuals, Respectively

After the outliers were identified and excluded and the two insignificant terms in the pre-final model were deleted the final model was generated. Table 4-2 represents the final model. Comparing Figure 4-10 and Figure 4-11, Figure 4-11 has a symmetric pattern indicating more constant variance. Also, this indicates a lack of independence of the residuals from the independent variables. In addition, the comparison of Figure 4-12 to Figure 4-13 illustrates the effect of excluding the outlier points. The final models histogram of residuals is fairly symmetric and although not perfectly normal, the hypothesis testing procedures for the parameter estimates and predictions are robust against violations of normality if the error distribution is symmetric and unimodal. In practical terms, this is a very good fit. Additionally, there are a reduced number of outliers on the Quantile and Outlier plot. The Normal Quantile plot is slightly less curved. These results allow one to conclude that a good model has been produced.

One point not discussed in the previous analysis of the prediction equation is the width of the confidence interval's (C.I.). The C.I.'s width is approximately 20 dB or ± 10 dB on either side of the predicted values. The C.I. width is another method for accessing a model's predictive performance, with narrower C.I.'s being better than wide C.I.'s. The C.I.'s width is a function of the variability in the data. Some of the sources of the variability in this data are from inaccuracies in the physical measurement of the bubbles length and width, non-uniformity of the bubble shapes, and the inherent variability in the RCS measurement process.

There are three possible techniques to produce narrower C.I.'s, which in turn will also produce a better prediction equation. The first technique is to better control the bubble geometry and characterize the variability in physical measurement of the length

and width. The second technique is to apply the concepts of designed experiments. The third technique is to perform more in depth statistical sleuthing with the LRA tools. Used alone, each of these techniques should help decrease the C.I.'s and produce a better regression model. However, it is recommended that all these techniques be used in concert to produce the best possible prediction model.

Reducing the physical variability and non-uniformity in the bubble geometry is a difficult task, however, through trial and error one should be able to produce a fairly symmetric and uniform bubble. One idea is, instead of using styrofoam pieces to produce a bubble, drill a hole on the backside of the testbody and use a screw to "push" the RAM into a bubble. Another idea for dealing with the physical variability is to characterize the variability. This could be accomplished by repeated measurement of the bubble length and width before and after each RCS measurement. Therefore, one could calculate an uncertainty factor (standard deviation) associated with the length and width.

The process of experimentation is a basic tool of the scientific method and in experimentation a response is measured as various factors are systematically changed, while other factors are held constant. The final goal of experimentation is to determine how the different factors affect the response. Experimental design is the process of determining the fewest number of measurements needed to gain the desired data. In this experiment, the only adjustable variables are the bubble length and width. In this experiment the length and width factor design points are depicted in Figure 4-14.

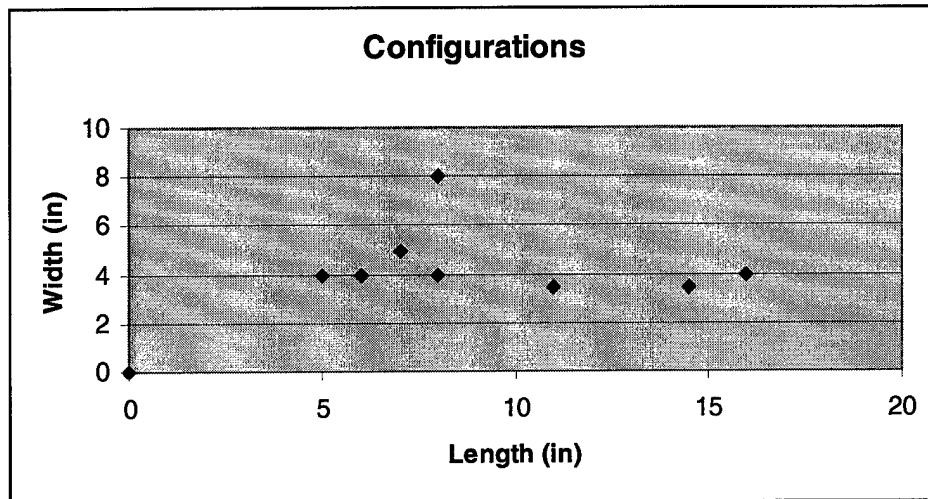


Figure 4-14 RAM Bubble Design Points

Almost all of the width variables are 4". A better-designed experiment would cover a broader range of length and width combinations. An example of a better-designed experiment is shown in Figure 4-15. Of course, the biggest obstacle in achieving these design points is actually producing bubbles of those sizes in the RAM.

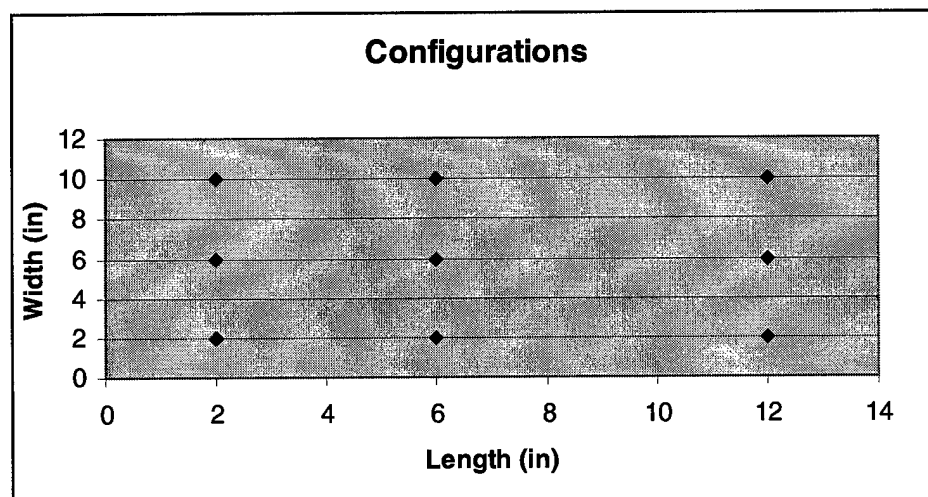


Figure 4-15 Proposed RAM bubble Design Points

The last technique recommended to decrease the C.I.'s and possibly produce a better regression equation is to modify the approach taken to generate the prediction

equation. The present model, Equation (4.7), was fit to all of the measured configurations. Another approach could be to fit a model for a subset of the configurations. In other words, fit a model for "small" bubbles, fit another model for "medium" bubbles, and fit another model for "large" bubbles. Some other ideas are to "smooth" or average the data, fit a model over a narrower range of frequencies, or fit a model over a narrower range of angles. The next step is to validate the model.

The goal of model validation is test the predicative ability of the model. Model validation accesses the strengths and weaknesses of a model. Model validation is different than the model adequacy-checking goal of ensuring the model is properly fit to the data.

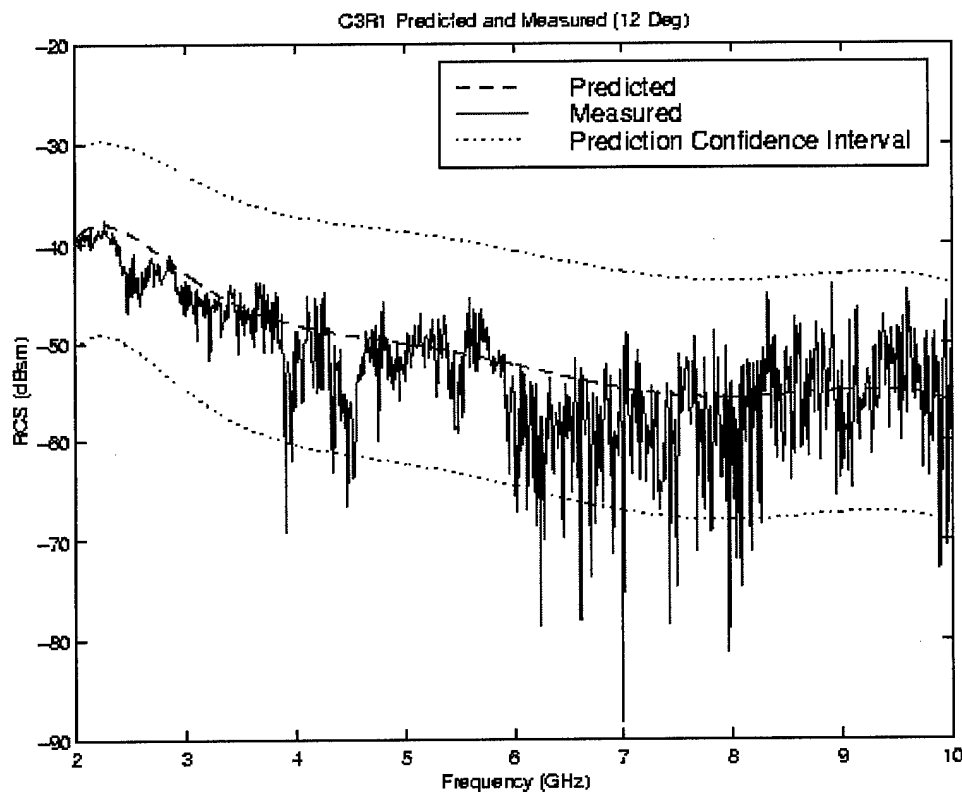


Figure 4-16 C3R1 (6"x4") Comparison of Predicted and Measured RCS

The Final model's equation is composed of the 18 terms and associated estimate in Table 4-2. The full equation is reiterated here in Equation (4.7).

$$\begin{aligned}
 -\ln\left(\frac{1-p}{p}\right) = & 1001.471 + 0.0093725\theta - 0.009974\theta\sqrt{\omega} - 0.717204L + 0.2595054L\sqrt{\omega} \\
 & - 0.001492\theta L\sqrt{\omega} - 0.934972W - 0.010025\theta W + 0.3383834\sqrt{\omega}W + 0.0017801\sqrt{\omega}W\theta \\
 & 0.1808437LW - 0.065963LW\sqrt{\omega} + 0.0003642\sqrt{\omega}LW\theta - 2775.993\sqrt{\omega} + 3162.6282\omega \\
 & - 1890.566\omega^{3/2} + 626.17049\omega^2 - 109.0511\omega^{5/2} + 7.8072637\omega^3
 \end{aligned}
 \tag{4.7}$$

To predict a bubble RCS in dBsm, all of the data is transformed out of the logistic transform to RCS in meters, then squared, and then put in dBsm.

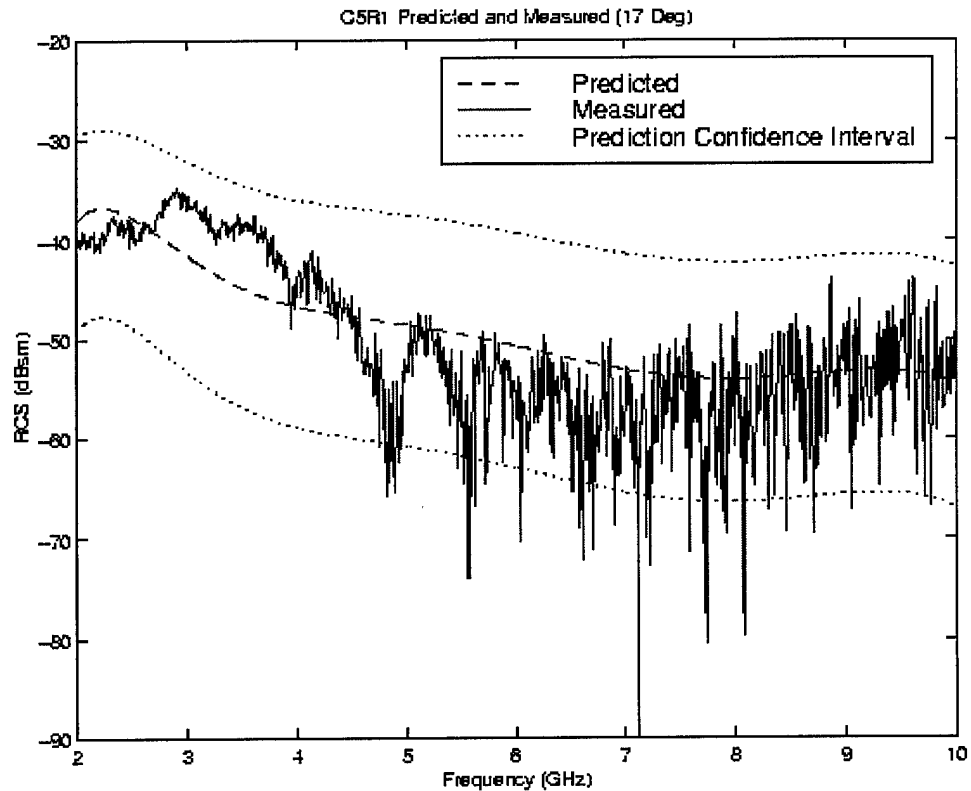


Figure 4-17 C5R1 (5''x4'') Comparison of Predicted and Measured RCS

The model was validated on data not used to build the model (e.g.- angles not divisible by five). In other words, the validation data is “fresh” data for the model. Figure 4-16, Figure 4-17 and Figure 4-18 are representative plots generated while performing model validation tests. The plots compare the measured and predicted values along with the predicted value’s prediction confidence intervals. The prediction confidence interval is the interval around the prediction that has a 95% probability of containing the true value. The underlying reason for the wide intervals on these predictions is the extreme variability in the higher frequency data.

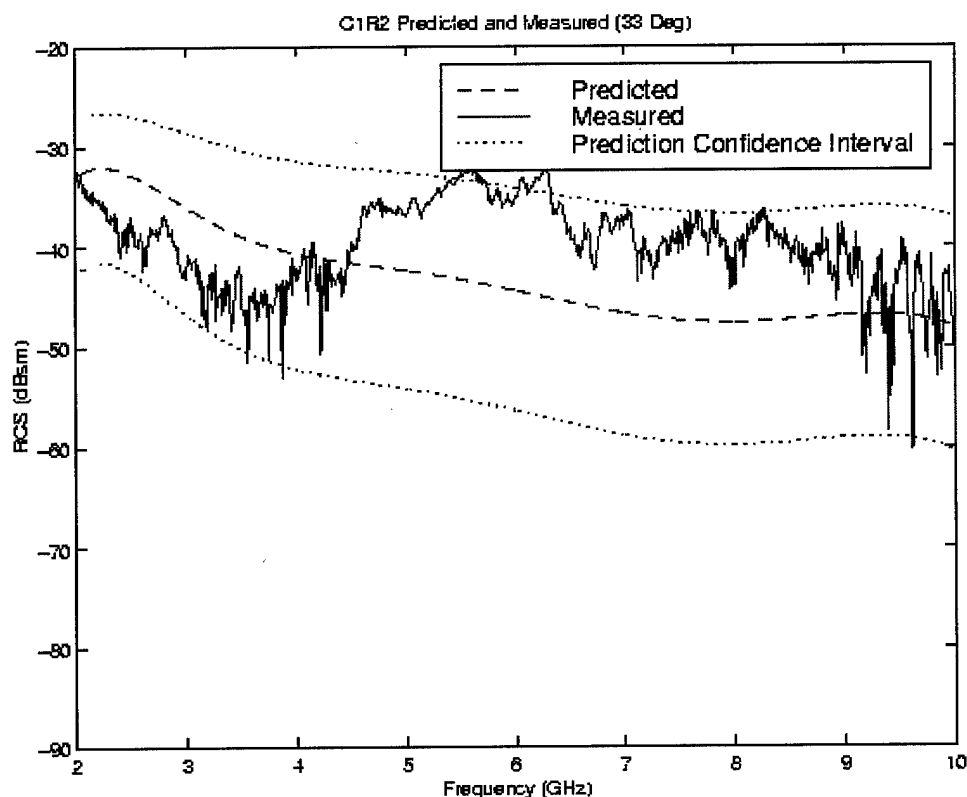


Figure 4-18 C1R2 (11"x3.5") Comparison of Predicted and Measured RCS

In the process of validating the final model, only one inadequacy was noticed. The model tends to give poor predictions for bubbles with long lengths (lengths > 10"). An example of not predicting a long length value well is shown in Figure 4-18. By comparing, Figure 4-18 to Figure 4-16 it is apparent that Figure 4-18 is not a strong fit whereas Figure 4-16 is a very strong fit. Figure 4-17 is an example of an average fit. A possible reason why long length values do not fit well is that only a few configurations used as data for building the prediction equation have long lengths. Therefore, one is *extrapolating*. Conversely, most of the configurations had a length value in the range of 4"-6" and the prediction equation responds strongly to those values as input. When we try to predict in these ranges one is *interpolating*.

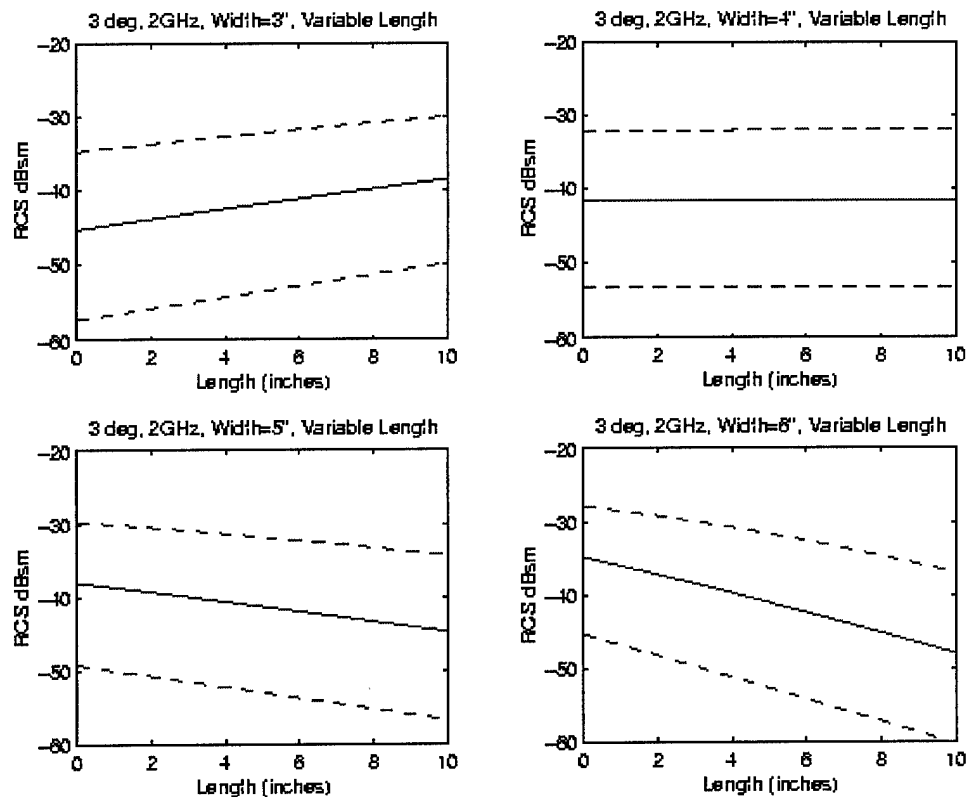


Figure 4-19 Predictive Capabilities Example by Varying Lengths and Widths (3°)

With the prediction equation built and validated, one can use it to gain insight into relationships in the bubble RCS data. Figure 4-19 and Figure 4-20 are examples of a demonstration of the model's predictive ability. The length and width relationships are explored by varying the length from 0"-10", varying the width from 3"-6" and fixing frequency and angle, 2 GHz and 3° respectively. Figure 4-19 shows the width variable is the dominant factor. For a 3" width, RCS increases with increasing length. For a 4" width, RCS remains constant with increasing length. For 5" and 6" bubbles, RCS decreases as length increases. Figure 4-20 shows similar results but for a 33° angle.

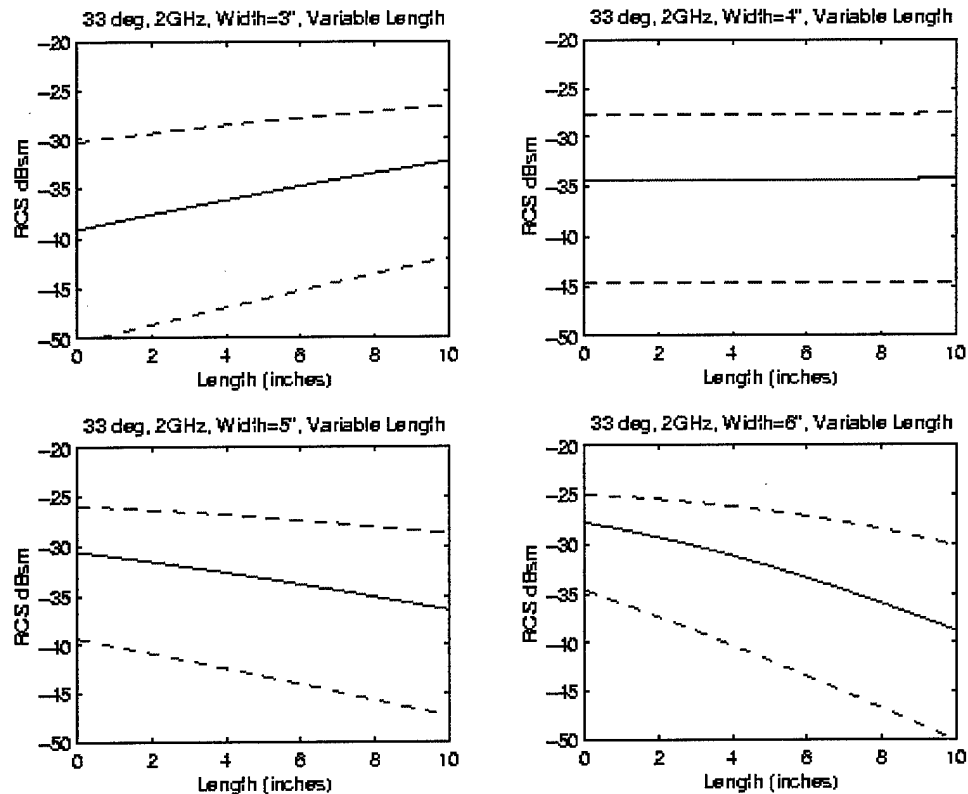


Figure 4-20 Predictive Capabilities Example by Varying Lengths and Widths (33°)

4.6 Bubble effects on a low RCS target

Demonstrating a perturbation of a low RCS, target's signature from a bubble is a secondary goal of this thesis. Without it, the impact of a bubble on a target is not fully appreciated. This section demonstrates the increase in a low RCS target's signature due to a bubble and the resulting increase in radar detection range. The low RCS target used for analysis is the NASA almond calculated with the XpatchF software. A series of RCS versus frequency plots facilitates visualizing the signature perturbation. Both the coherent and incoherent cases are examined. Following the plots, a calculation using the radar range equation quantifies the change in detection range for an L-band search radar.

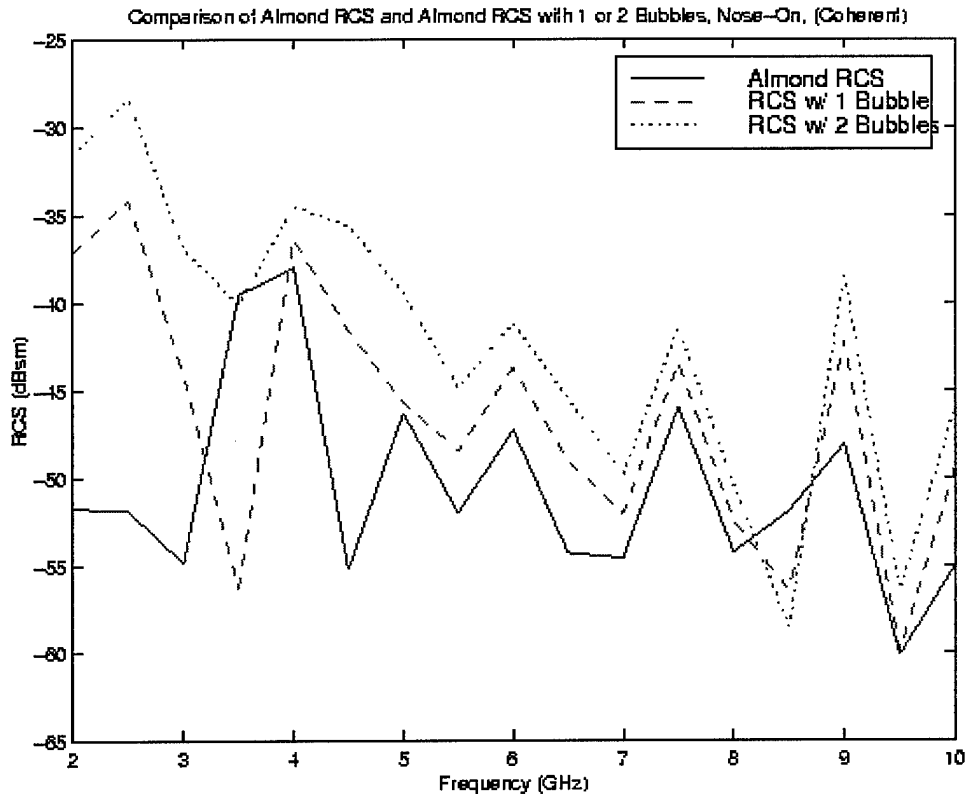


Figure 4-21 Comparisons of the Coherent RCS of an Almond with and without Bubbles

Figure 4-21 depicts the case of coherent addition of the RAM bubble E-fields to the almond's E-fields. Coherent addition accounts for both the magnitude and phase components of the E-fields and is the most accurate representation of the target. Therefore, if the E-fields are completely out of phase a deep null is obtained in the signature. Conversely, if the E-fields are completely in phase, a peak is produced.

Figure 4-21 compares the Almond RCS with and without bubbles. The RCS analysis of section 4.3 concluded that RAM bubbles have the highest RCS at low frequencies. Figure 4-21 validates the impact of that conclusion. The bubbles increase the almond's signature at the lower frequencies. One other point is the apparent increase in RCS at the higher frequencies. This increase is a result of adding the range noise +

clutter and is an artifact from the measurement. Therefore, one cannot draw any conclusions on the bubble impact at the higher frequencies.

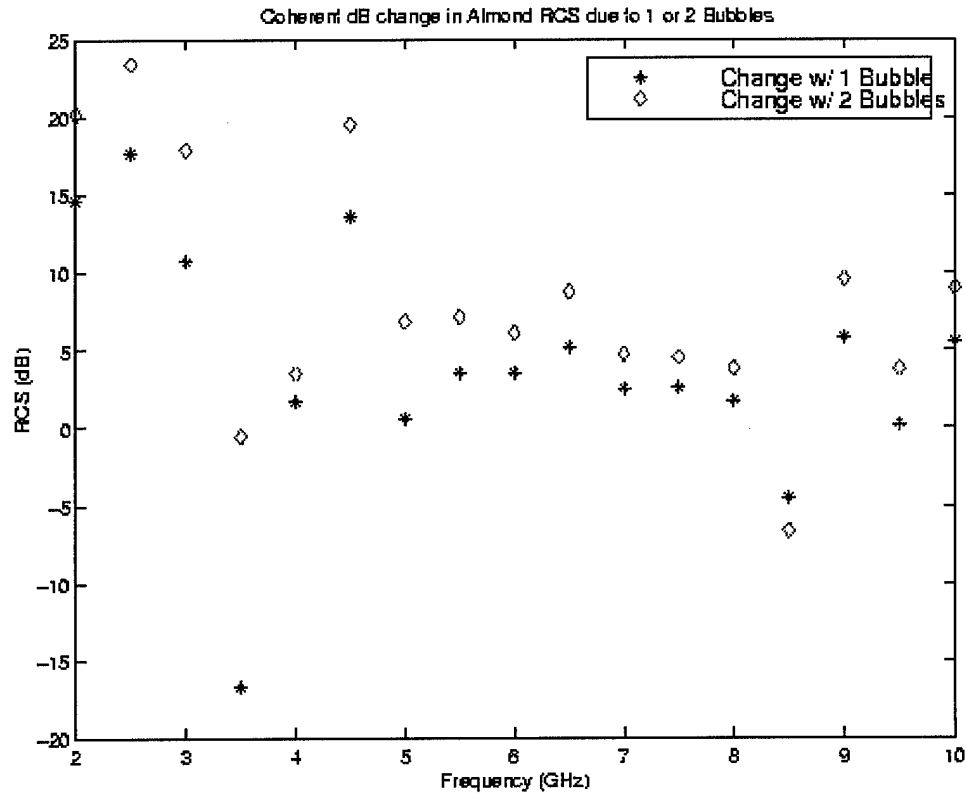


Figure 4-22 Coherent Changes in dB due to the Bubbles

Figure 4-22 depicts the coherent change in dB produced by the bubble and is another method for analyzing the bubble's impact. The plot was generated by subtracting the coherent almond's RCS in dBsm from the coherent almond with bubble's RCS in dBsm. At the low frequencies, the bubble changes the signature by approximately 15-20 dB. Again, the 1-5 dB increase at the higher frequencies is noise + clutter and is a distortion of the data.

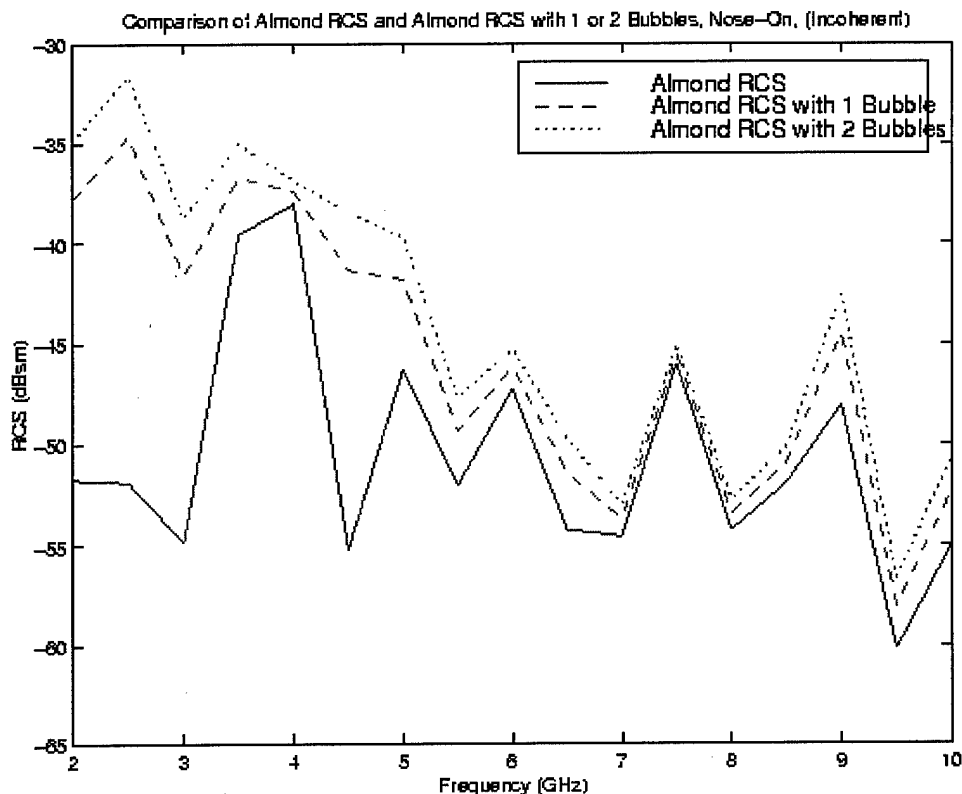


Figure 4-23 Comparisons of the Incoherent RCS of an Almond with and without Bubbles

Figure 4-23 and Figure 4-24 represents the case of the incoherent addition of the almond and bubble's E-fields. Incoherent addition only adds the magnitude of the E-fields. This shows what the signature looks like without accounting for the phase component and therefore the nulls in the pattern are only from the magnitude changes. The incoherent case is similar to the coherent case because it also shows the bubble has the strongest impact at lower frequencies. Again, the higher frequency increases are due to range noise + clutter in the measurement data and therefore are inconclusive.

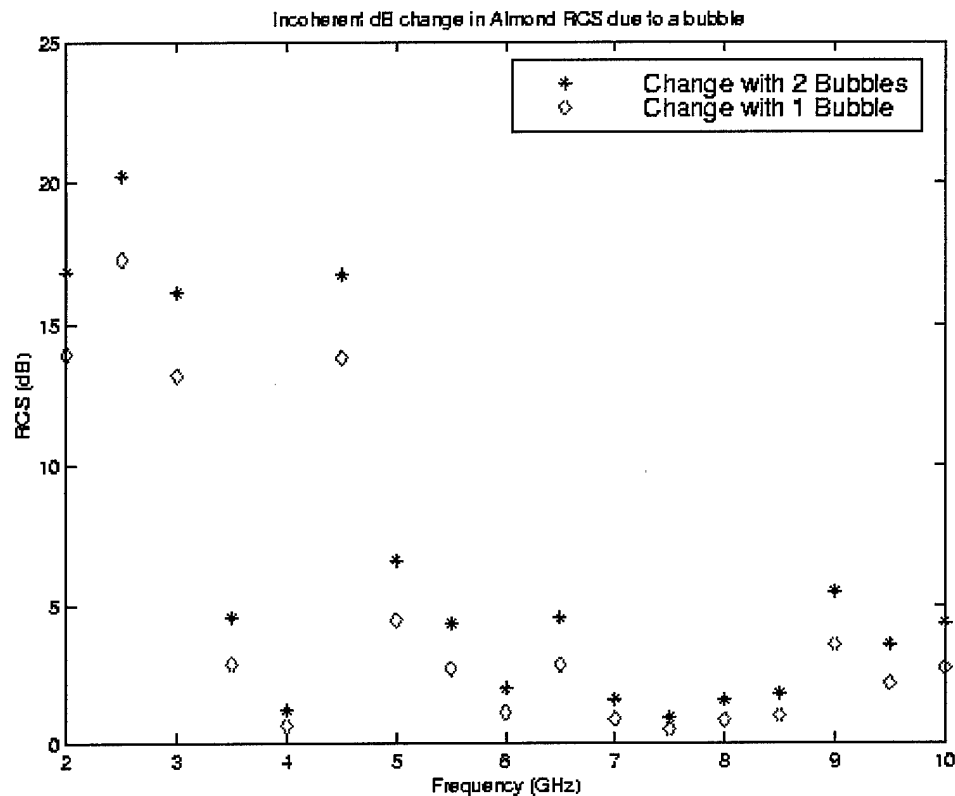


Figure 4-24 Incoherent Changes in dB due to the Bubbles

Figure 4-24 depicts the incoherent change in dB produced by the bubble and is another method for analyzing the bubble impact. The plot was generated by subtracting the incoherent almond's RCS in dBsm from the incoherent almond with bubble's RCS in dBsm. These results are similar to the coherent case except the coherent case is approximately 5 dB higher in the lower frequencies.

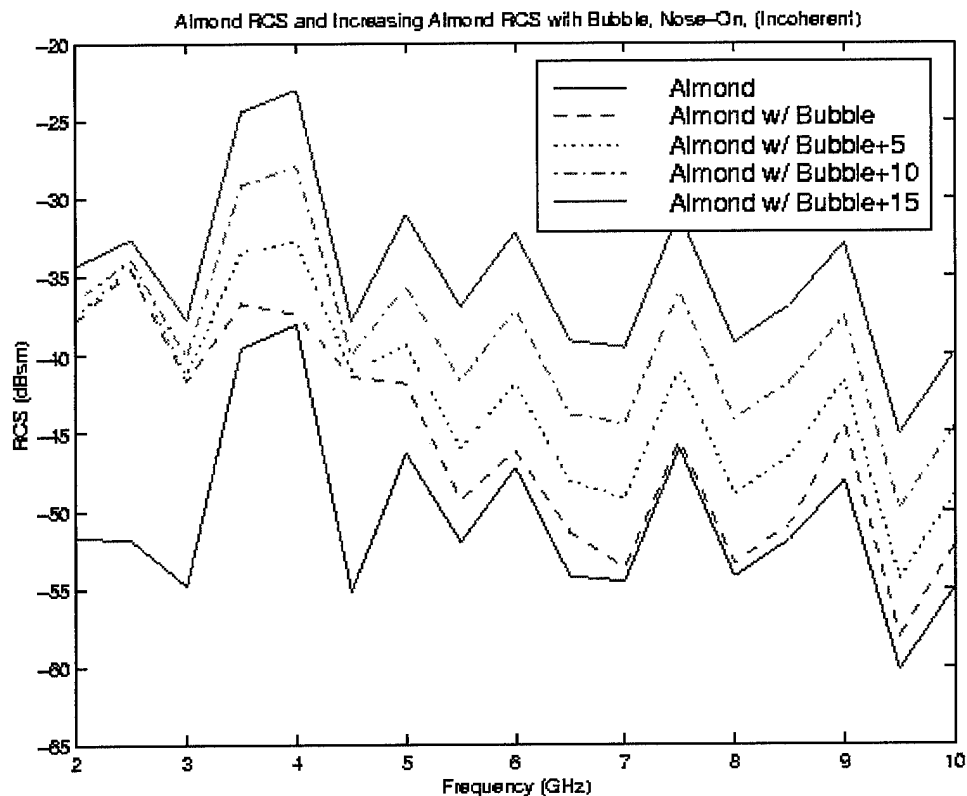


Figure 4-25 Effect of a Dominant Scatterer

The effect of a dominant scatterer is depicted in Figure 4-25. Adding 5, 10 and 15 dB of signal to the RCS of the almond and then incoherently adding the bubble E-field produced this plot. For 2-3GHz, the bubble is the dominant scatterer and increasing the almond RCS has little effect. Conversely, the almond's RCS dominates the signature in the higher frequencies and the range noise + clutter has little effect.

Possibly, the ultimate demonstration of the impact of a bubble on a low RCS target is to calculate a change in the target's detection range due to the bubble. Skolnik [21] gives specifications for an ASR-8 L-Band search radar (2.5 GHz operating frequency) and the proper version of the Radar Range equation that applies to search radars.

$$R = \left[\frac{P_t G^2 \lambda^2 \sigma_f \theta}{(4\pi)^3 SNR k T B F_w} \right]^{\frac{1}{4}} \quad (4.7)$$

R = Range	σ = RCS	T = Room Temperature
P _t = Peak Power	f _r = Pulse Repetition Freq	B = Noise Bandwidth
G = Antenna Gain	θ = 3 dB beamwidth	F = Noise Figure
λ = wavelength	k = Boltzmann's constant	ω = scan rate

The specifications for the ASR-8 radar are inserted into Equation (4.7) along with the almonds RCS with and without a bubble. Table 4-3 summarizes the change in detection range calculations. The detection range change is based on the assumption that no clutter is present. The increase in detection range due to the bubble is a clear indicator that bubbles can have a detrimental effect on the RCS of LO systems and therefore maintenance actions are necessary to preserve RCS signature integrity.

Table 4-3 Summary of Change in Detection Range

	RCS (dBsm)	Detection Range (km)
Almond	-51.86	10.961
Almond with one bubble	-34.17	30.346
Δ	-17.69	19.385

4.7 Summary

The primary objective of Chapter IV was to analyze the measured data and provide answers to the research goals posed in Chapter I. The research goals set out in Chapter I were to characterize the absolute RCS of RAM bubbles and use linear regression analysis to develop a prediction equation relating RCS to angle, frequency, and bubble geometry. Additionally, secondary goals of the thesis were assessing the viability of using simulated data to generate RCS data of RAM bubbles and also demonstrating the detrimental effects of a bubble on a low RCS targets signature.

The results from the absolute RCS measurement of the various sized RAM bubbles were discussed in terms of a frequency dependent increase in RCS. In the frequency band of interest, 2 –18GHz, a RAM bubble increases the RCS at all angles, from grazing incidence (0°) to 45° . From 10 -18GHz the RAM bubble does not cause an increase in RCS. The actual dB increase in RCS is highly dependent on angle, frequency and bubble size. In general, the highest RCS is at 2GHz and tapers down as frequency increases. Additionally, the RCS increases as the angle increases away from grazing incidence. At near grazing angles, the RCS increase due to the bubbles is 10-15dB. At the higher angles, the RCS increase due to the bubbles is 10-20dB. The RCS increase is relative to the noise plus clutter measurement of the range. Finally, the range of absolute RCS values for the various bubble sizes can range from -55 dBsm to -25 dBsm.

The result of the linear regression analysis is Equation (4.7). Equation (4.7) is the prediction equation that uses input parameters of angle, frequency, and bubble geometry to output a predicted RCS value for a RAM bubble. Subsequently, a demonstration of

the predictive capabilities of the equation discovered that bubble width is the dominant factor. Knowing this, one concludes that flightline RAM maintainers should fix long narrow bubbles before fixing wider more symmetric bubbles.

Analysis of the simulation results of JRMBOR revealed that the majority of the simulated points approximately match the measured points. This lends credibility to using JRMBOR as a tool for generating simulated data. However, further testing is recommended before using simulations as an actual data generation tool.

The final point made regarding RAM bubbles was the calculation the change in detection range of a low RCS target due to the bubble. Using the NASA almond as a target against an L-Band radar, assuming no clutter, the radar range equation showed that the almond's detection range is increased by 19.385 km. This represents a 176% increase in detection range. Mission planners could use this type of analysis for changing aircraft ingress and egress routes if maintainers do not have the option of repairing degraded RAM due to bubbles.

Chapter 5 Conclusions and Recommendations

5.1 Conclusions

In this thesis, a database of the measured RCS of RAM bubbles is generated. The database is used to characterize the absolute RCS of the RAM bubbles and develop a RAM bubble RCS prediction equation. The purpose of the characterization and prediction equation is to give engineers and maintainers insight into the detrimental effects of bubbles in RAM. Additionally, other avenues of research are pursued. Simulated RCS measurements of the RAM bubbles are accomplished to compare with the measured results. This comparison demonstrates the viability of using simulations as an alternative to measuring data.

The range of absolute RCS values for the various bubble sizes can range from -55 dBsm to -25 dBsm. The actual dB increase in RCS is highly dependent on angle, frequency and bubble size. In general the highest RCS of a RAM bubble is at 2GHz and tapers down as frequency increases. The RCS increase is relative to the noise plus clutter measurement of the range.

The result of the linear regression analysis is Equation (4.7). Equation (4.7) is the prediction equation that uses input parameters of angle, frequency, and bubble geometry to output a predicted RCS value for a RAM bubble. Subsequently, a demonstration of the predictive capabilities of the equation discovered that bubble width is the dominant factor.

Finally, a calculation of the change in detection range of a low RCS target is accomplished. Using the NASA almond as a target against an L-Band radar, assuming

no clutter, the radar range equation shows that the almond's detection range due to the bubble is increased by 19.385 km. This represents a 176% increase in detection range.

5.2 Recommendations

Based on the analysis and results of this thesis, it is recommended that future research continue in the following areas.

The first recommendation is to have a statistician trained in data mining thoroughly analyze the data. Insights gained through statistical inference can describe relationships in data that are otherwise difficult to see.

The second recommendation is to generate more measured RCS data on the RAM studied herein. The measurements needed are much smaller geometry bubbles (e.g. 2-3"x2-3"). These measurements could then be added to the database and a new prediction model could be refit. Additionally, it is recommended that the data be averaged to reduce variability from the noise or only fit the model in a 2-6 GHz frequency range.

The third recommendation is to generate measured RCS bubble data on several different types of RAM. These measurements could be added to the current database to generate a new model that includes the ϵ_r and μ_r as variables for input. Then possible relationships could be studied to try to find an ϵ_r and μ_r that produces RAM that, if degraded from bubbles, does not negatively effect the target's signature.

The last recommendation is to pursue generating the RAM bubble RCS measurements through simulations. If the simulations match the measurements, then simulations could serve as a data generation capability if measurement facilities are not available. Another idea is that simulations could serve as a complementary method, ensuring the measurements were performed properly. In addition, simulations could give

insight to what one might expect before measurements are performed. However, if JRMBOR or other low frequency software is used as a tool for generating large data sets, a much faster computer is needed to make the collection effort efficient.

Appendix A

This appendix is a compilation of the 3-D image plots for each configuration. The 3-D image plots identify scattering centers relative to downrange and crossrange.

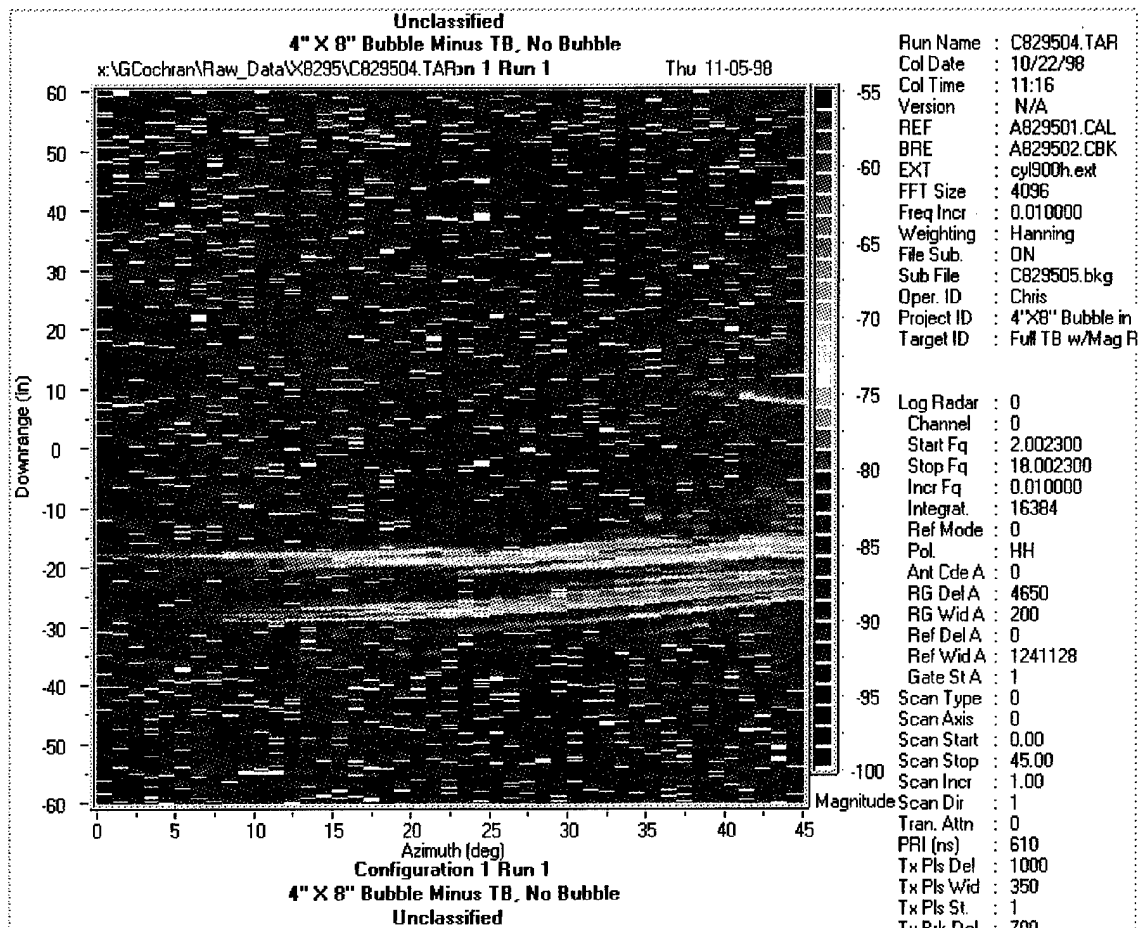


Figure A-1 Configuration 1 Run 1 (4"x 8" Bubble)

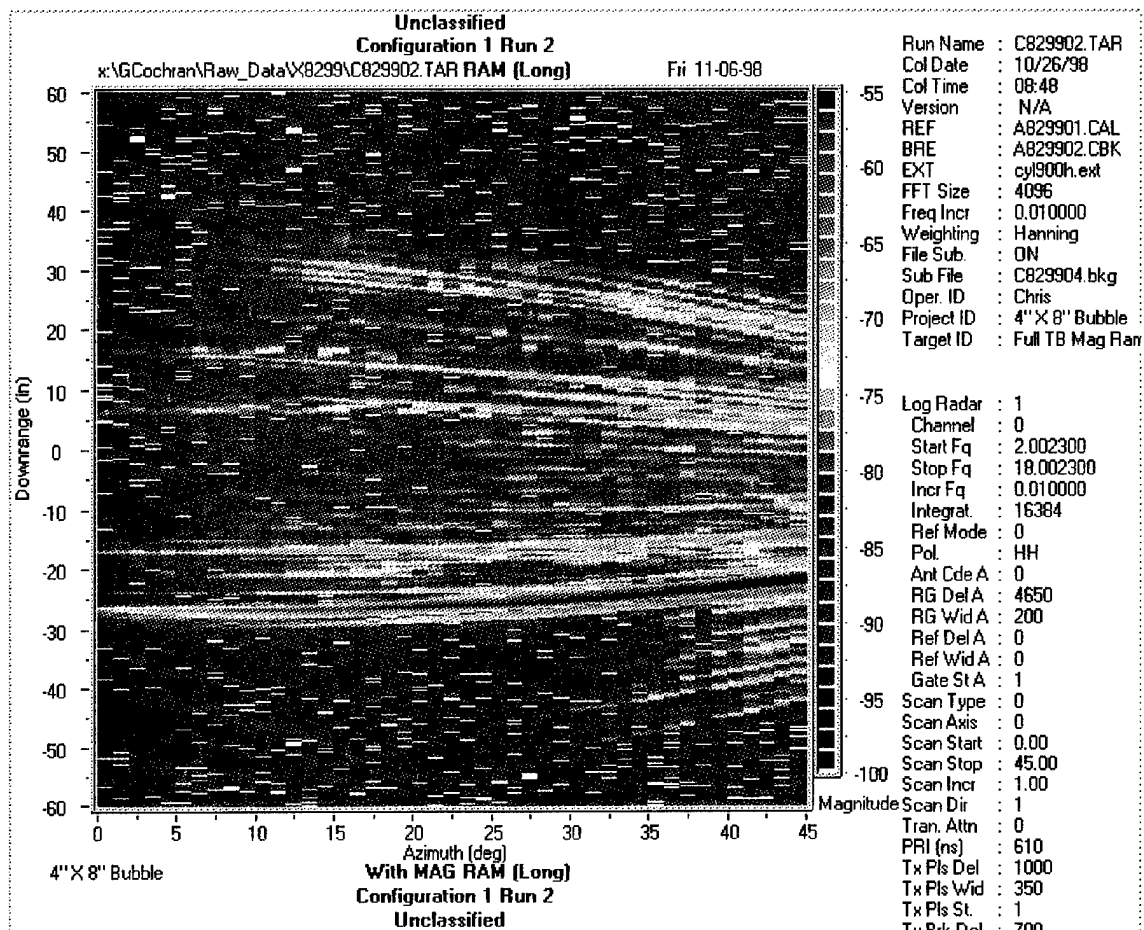


Figure A-2 Configuration 1 Run 2 (3.5" x 11" Bubble)

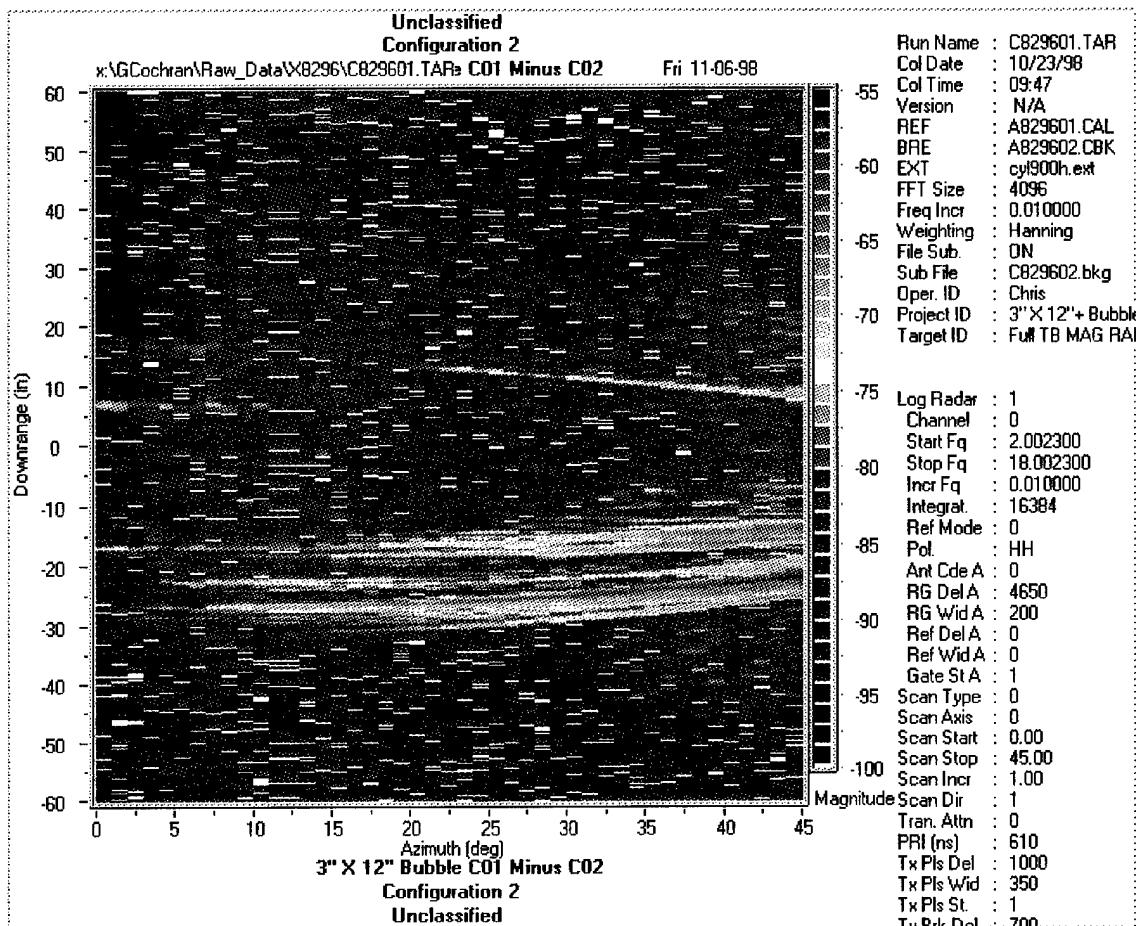


Figure A-3 Configuration 2 Run 1 (3.5" x 14.5")

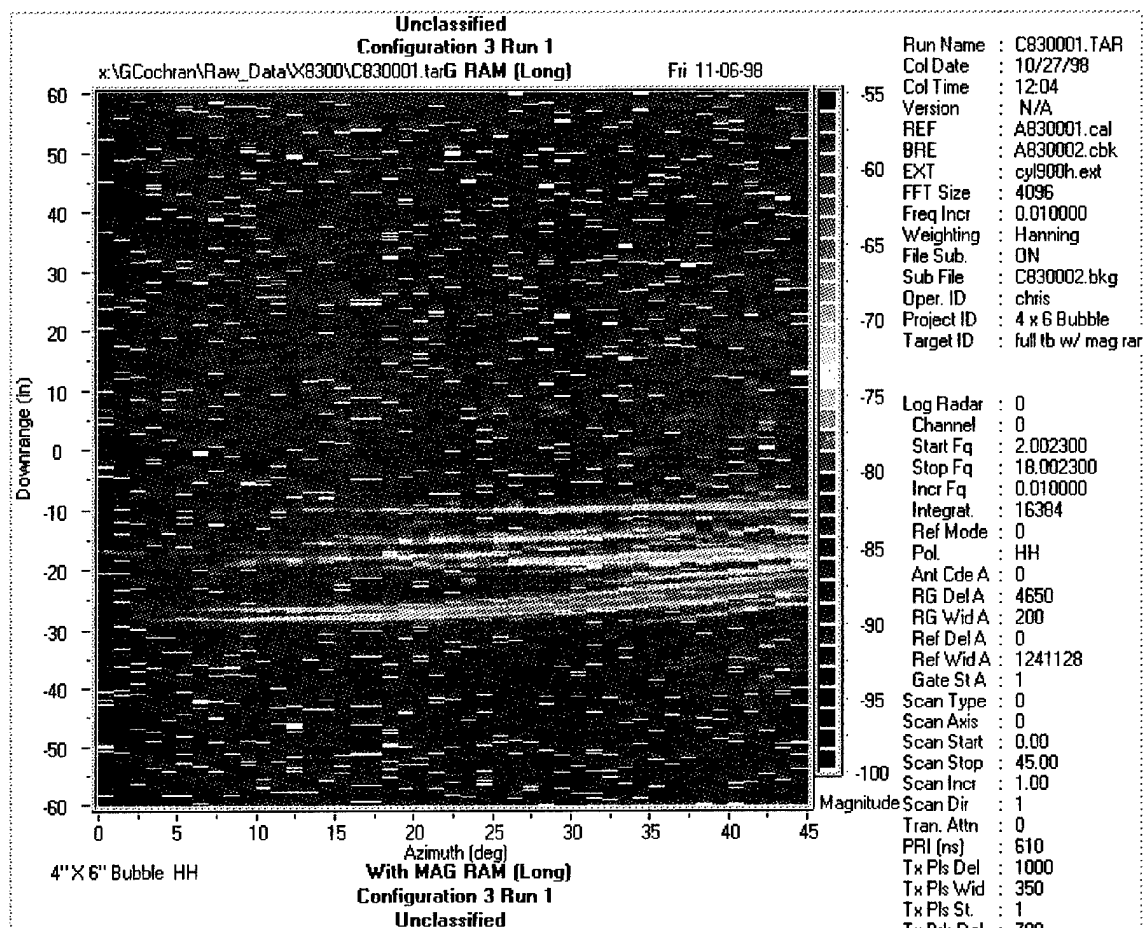


Figure A-4 Configuration 3 Run 1 (4" x 6")

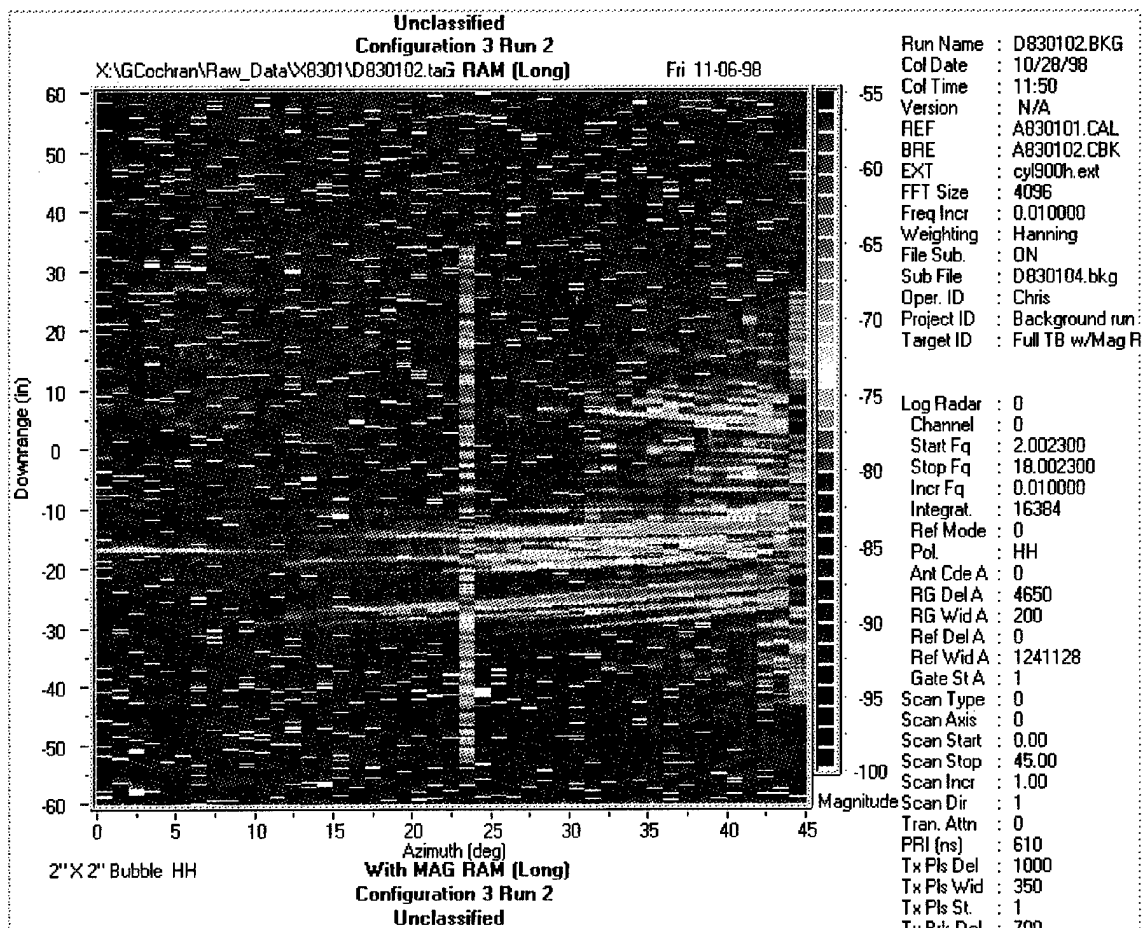


Figure A-5 Configuration 3 Run 2 (5" x 7")

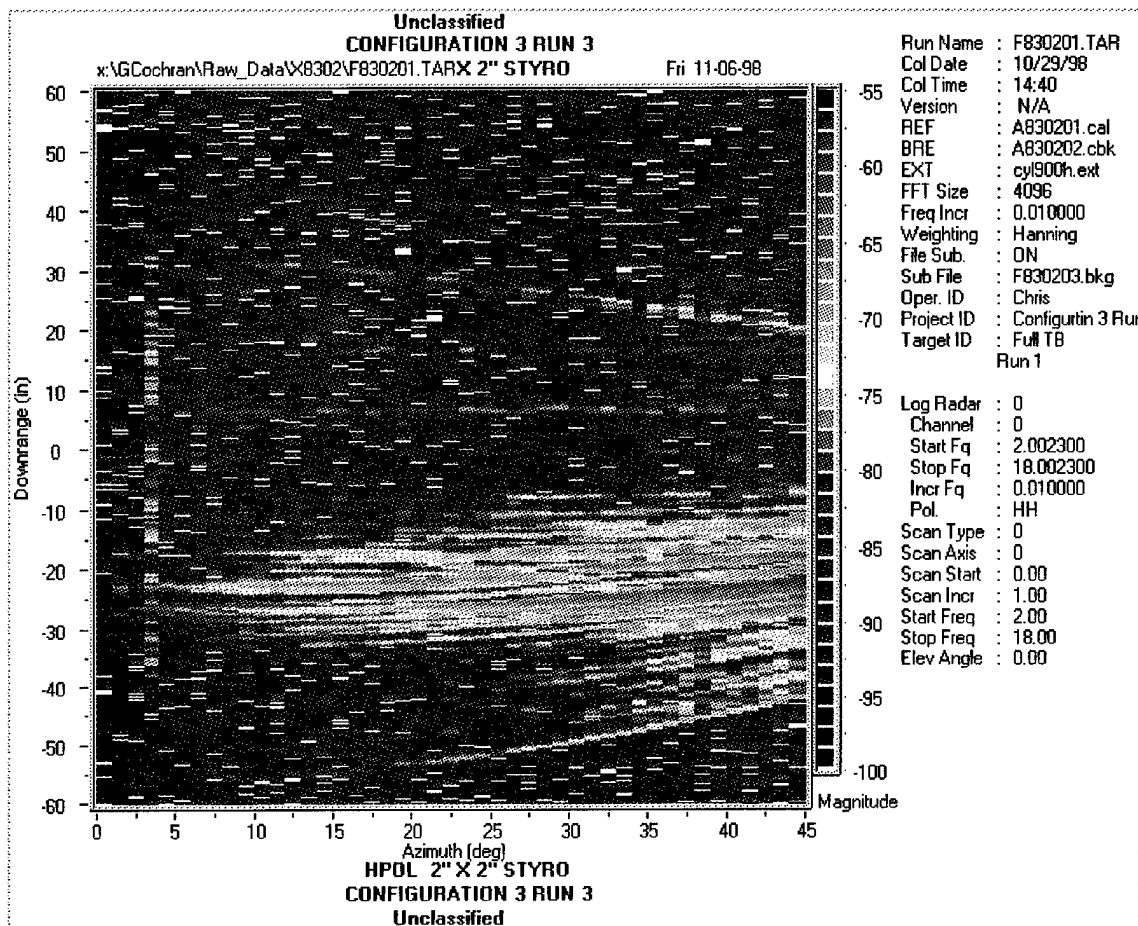


Figure A-6 Configuration 3 Run 3 (5" x 7")

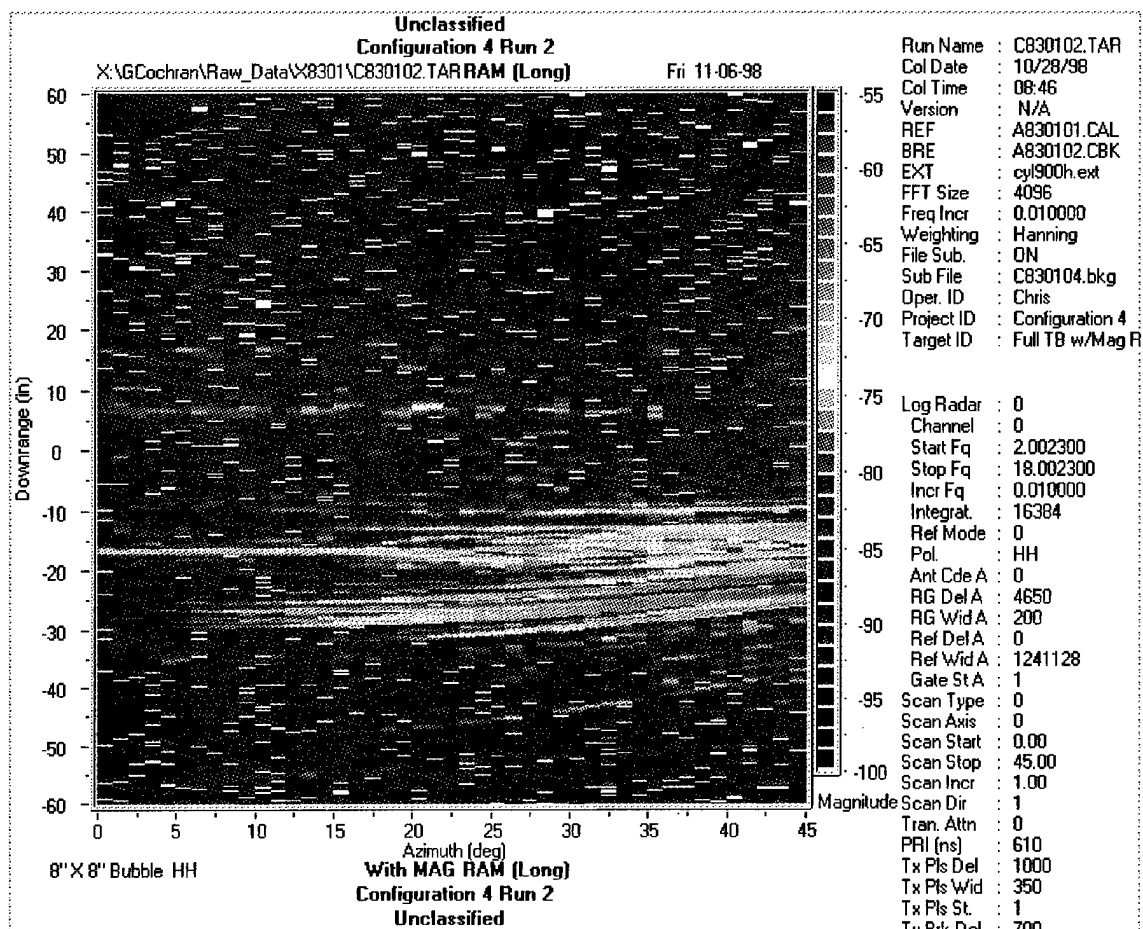


Figure A-7 Configuration 4 Run 1 (8" x 8")

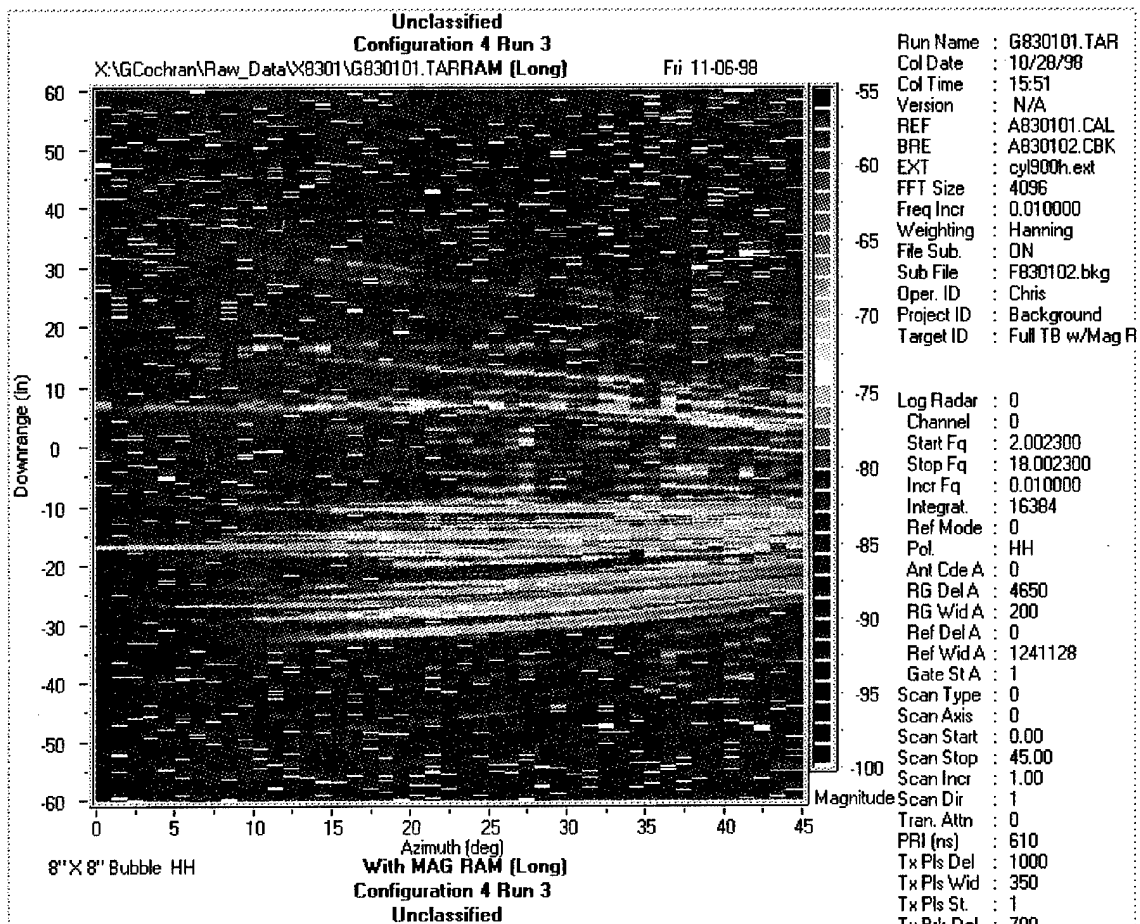


Figure A-8 Configuration 4 Run 2 (4" x 16")

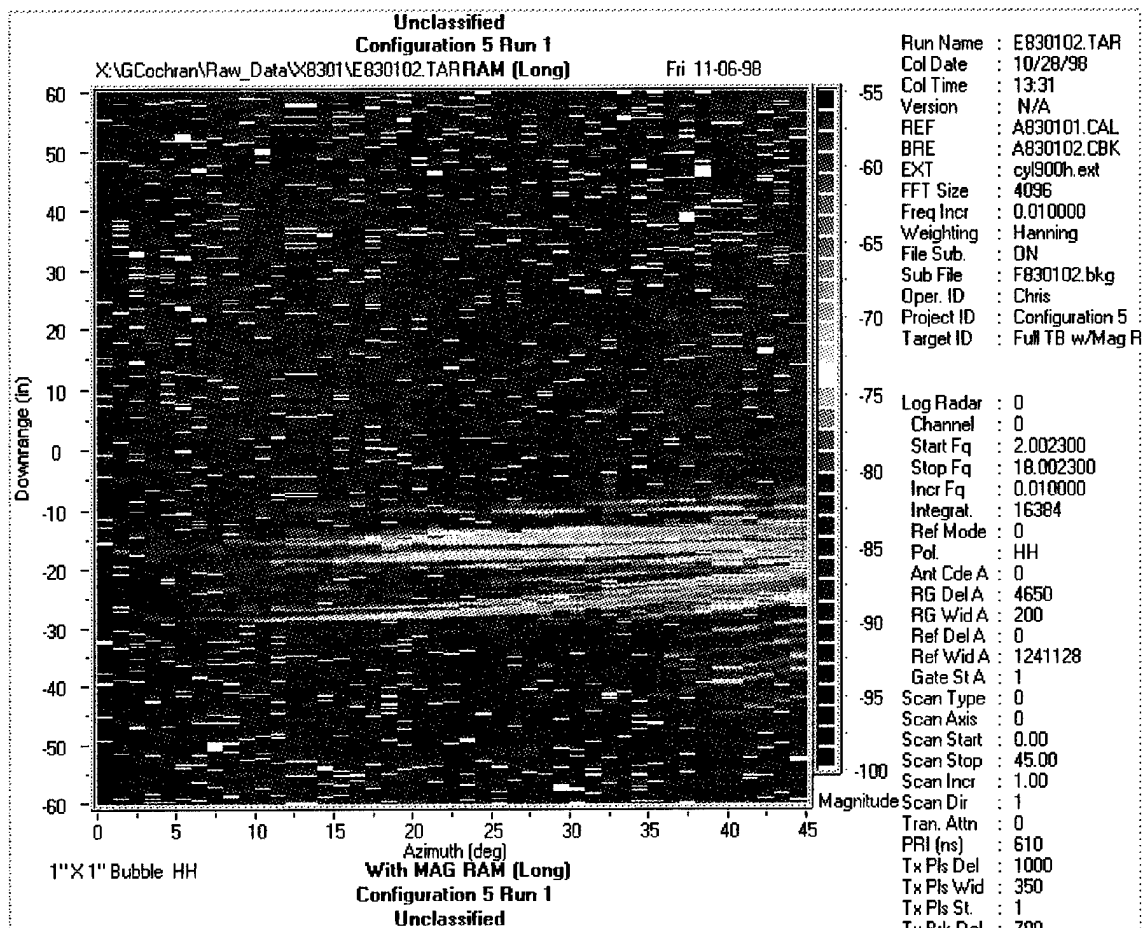


Figure A-9 Configuration 5 Run 1 (4" x 5")

Appendix B

This appendix is a compilation of the waterfall plots generated for the various bubble configurations. Each plot depicts the RCS in dBsm of one configuration for a frequency range of 2-18 GHz and angles of 0° to 45° in 5° increments.

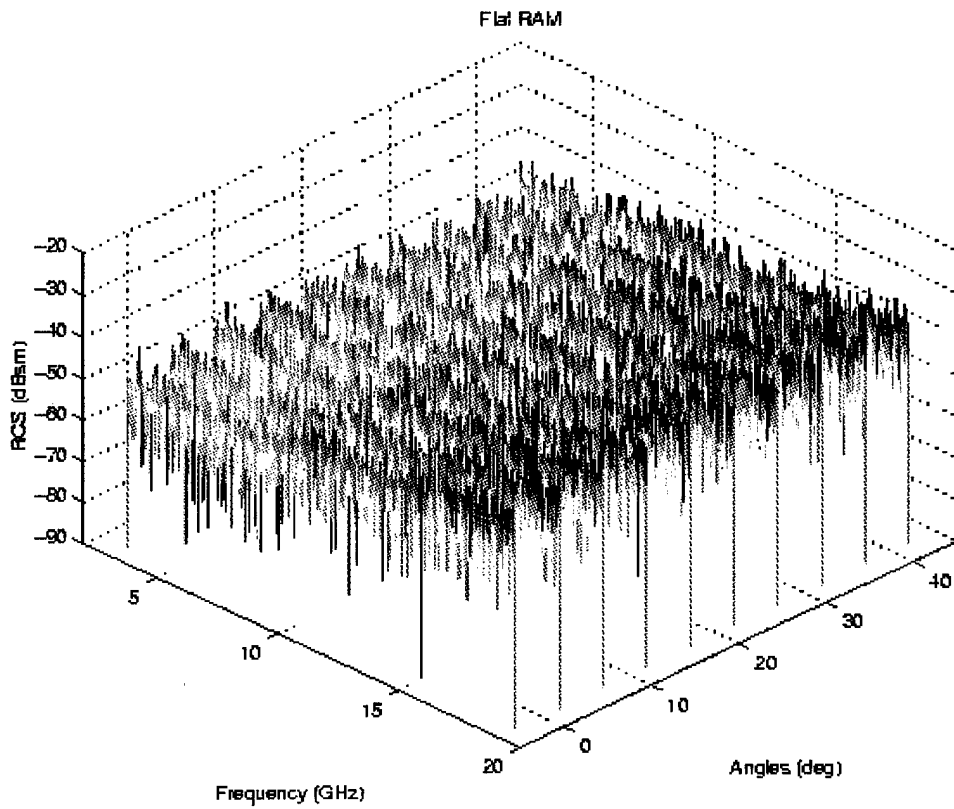


Figure B-1 Waterfall plot of Range Noise + Clutter

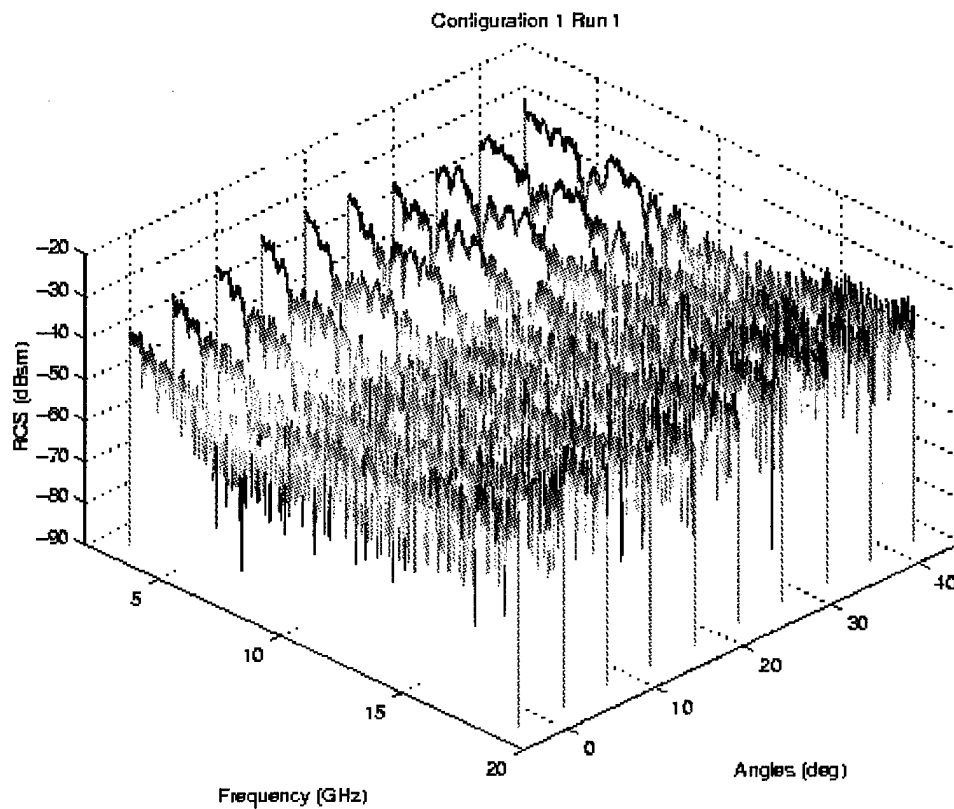


Figure B-2 Waterfall plot of Configuration 1 Run 1 (4"x8" bubble)

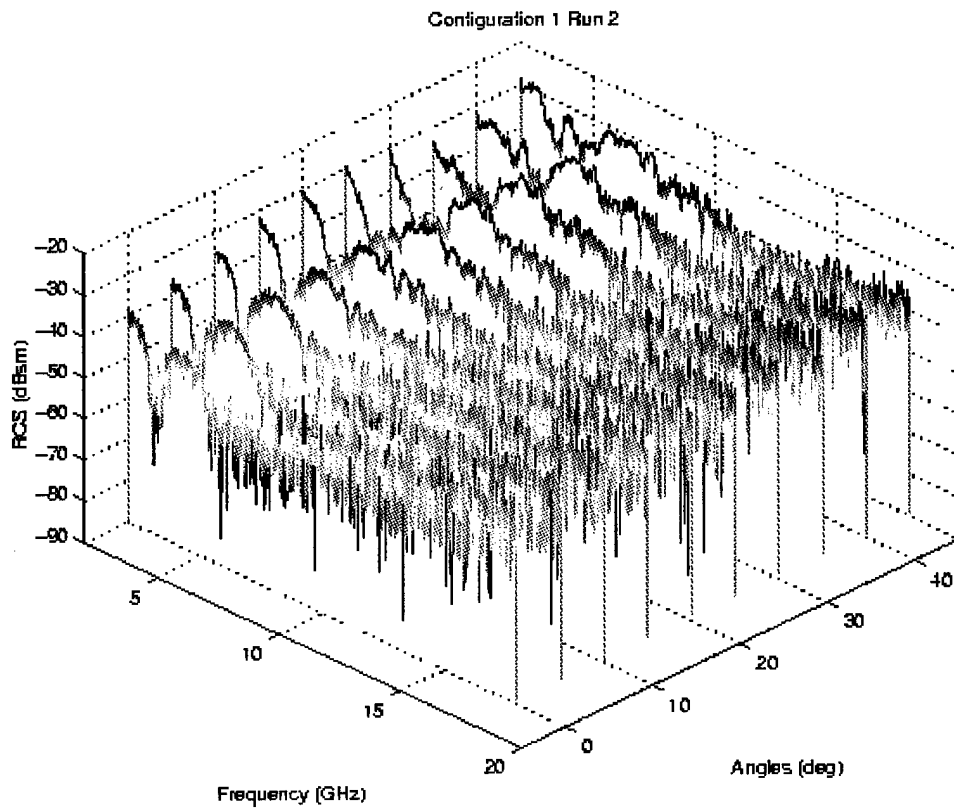


Figure B-3 Waterfall plot of Configuration 1 Run 2 (3.5"x11" bubble)

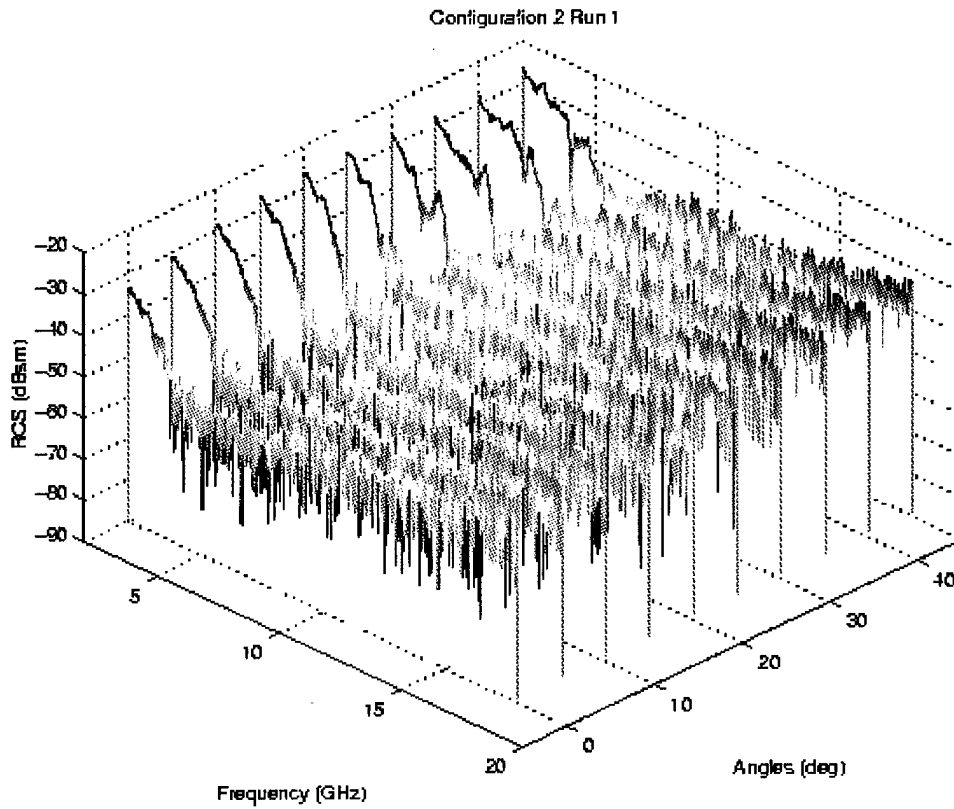


Figure B-4 Waterfall plot of Configuration 2 Run 1 (3.5"x14.5" bubble)

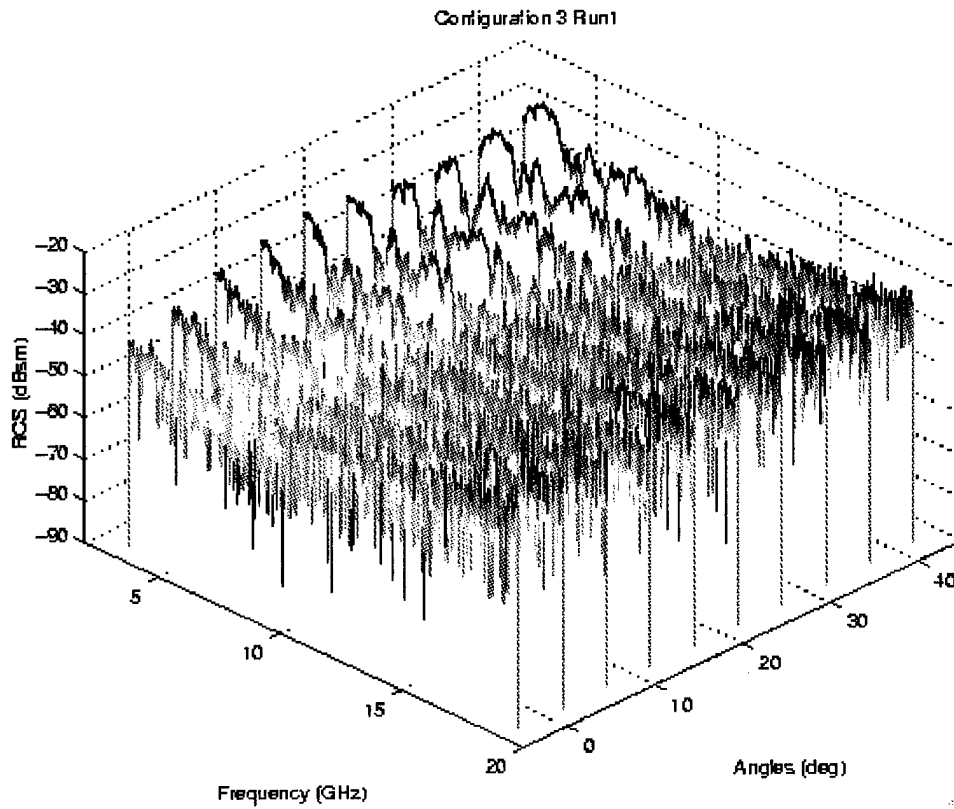


Figure B-5 Waterfall plot of Configuration 3 Run 1 (4"x6" bubble)

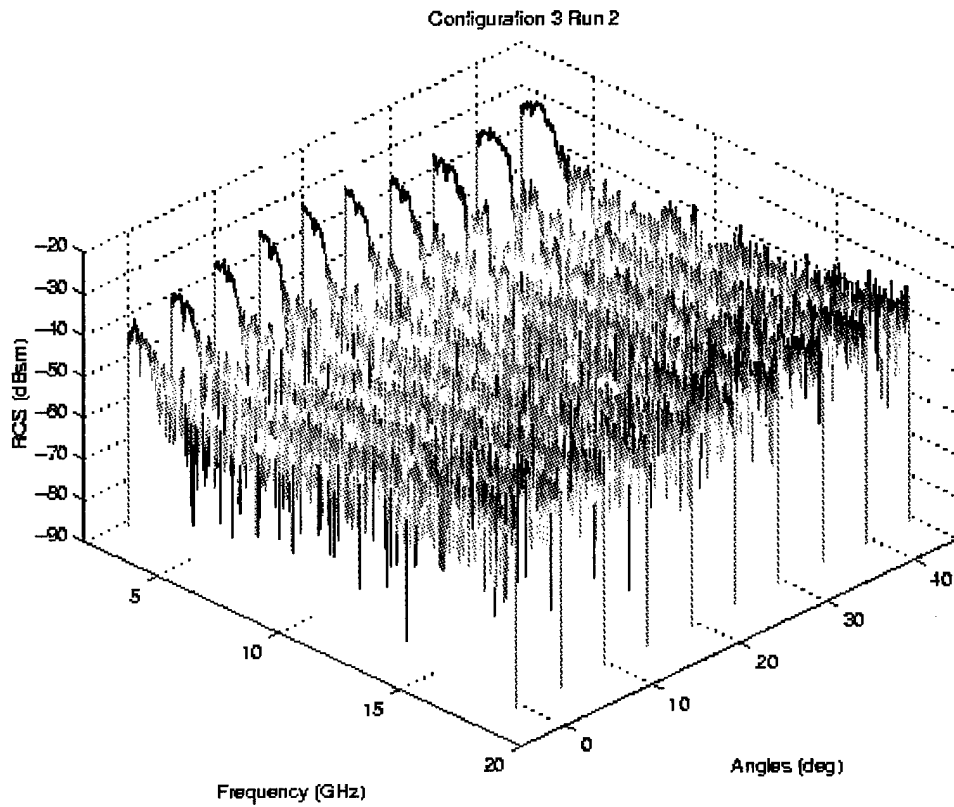


Figure B-6 Waterfall plot of Configuration 3 Run 2 (5"x7" bubble)

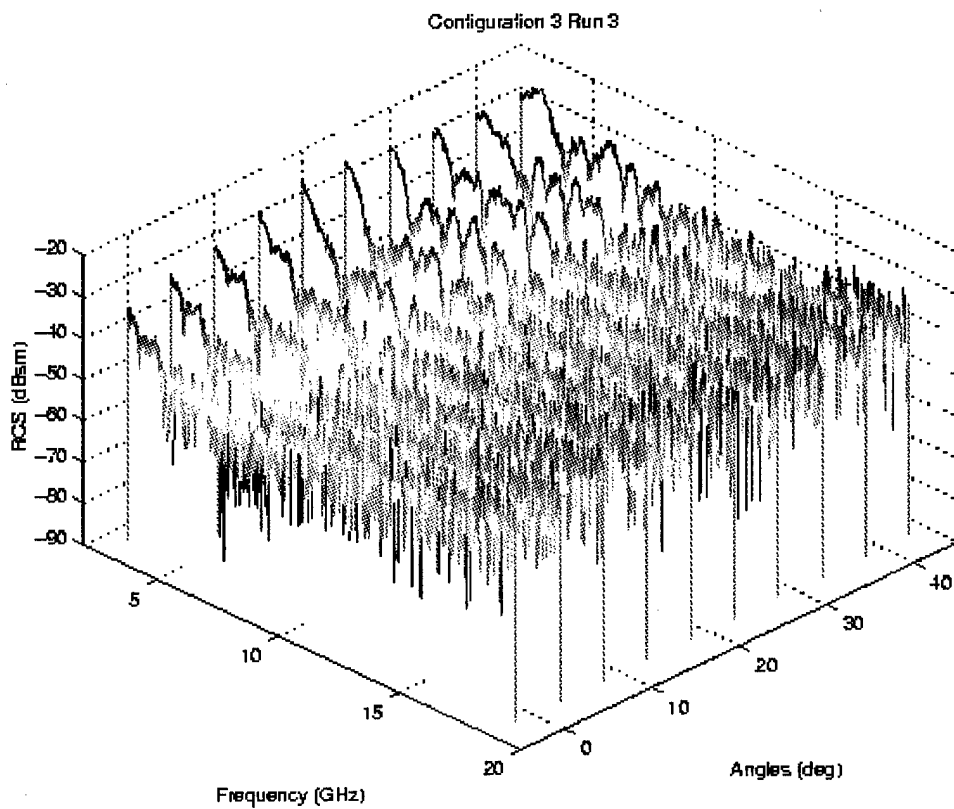


Figure B-7 Waterfall plot of Configuration 3 Run 3 (5"x7" bubble)

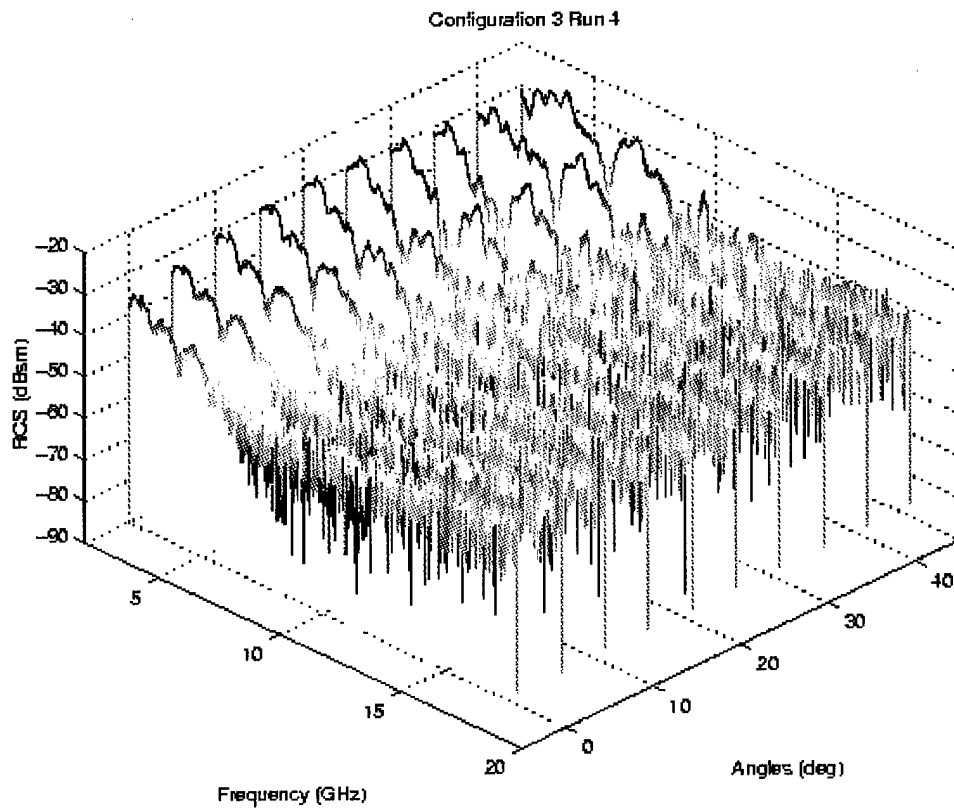


Figure B-8 Waterfall plot of Configuration 3 Run 4 (5"x7" bubble)

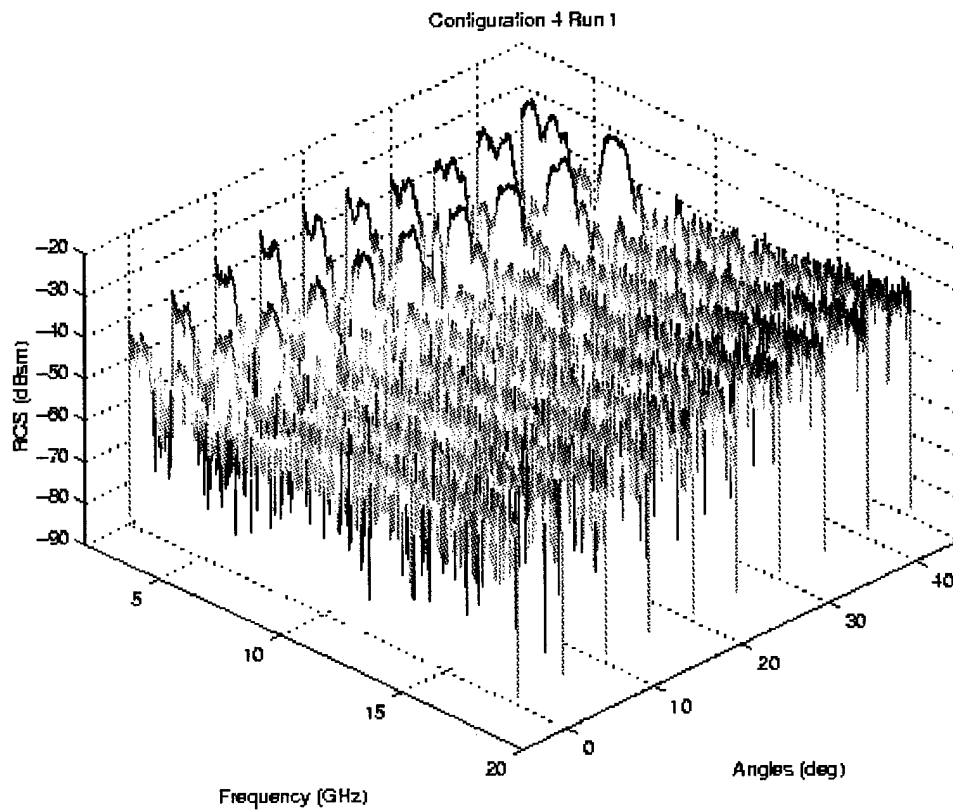


Figure B-9 Waterfall plot of Configuration 4 Run 1 (8"x8" bubble)

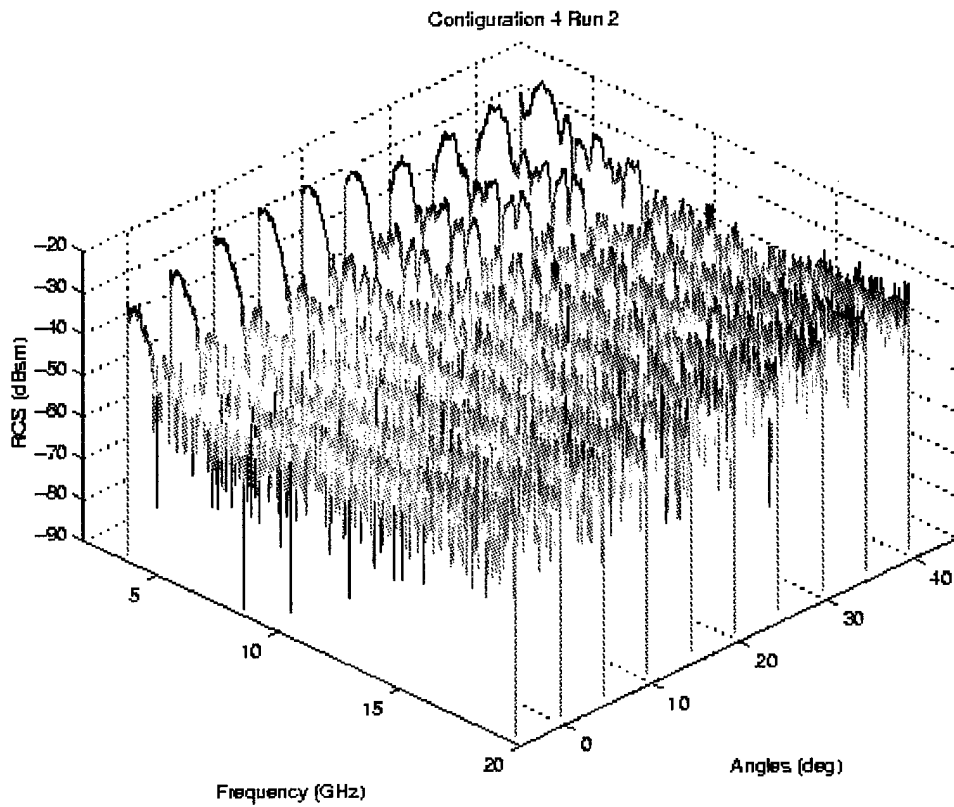


Figure B-10 Waterfall plot of Configuration 4 Run 2 (4"x16" bubble)

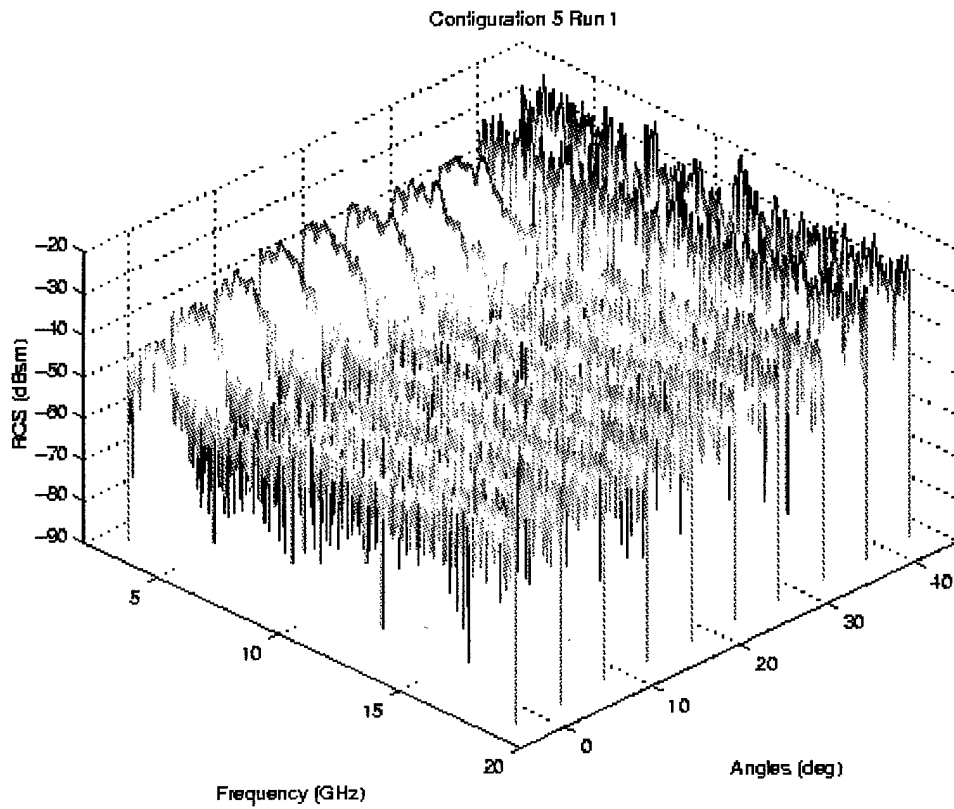


Figure B-11 Waterfall plot of Configuration 5 Run 1 (4"x5" bubble)

Appendix C

This appendix is a compilation of the waterfall plots generated for each angle from 0° to 45° in 5° increments. Each plot depicts the RCS in dBsm of one angle for a frequency range of 2-18 GHz and all configurations. The purpose of the waterfall plots is to demonstrate the uniqueness in RCS of each RAM bubble configuration. The uniqueness is a function of the non-uniformity and complexity of the bubble geometry and the inherent variability of RCS measurements. The configurations are plotted according to Table 3-1. For instance, on all the waterfall plots the return of configuration 1 corresponds to Bkg4 (the range noise + clutter) and configuration 10 corresponds to c5r1 (Configuration 5 Run 1).

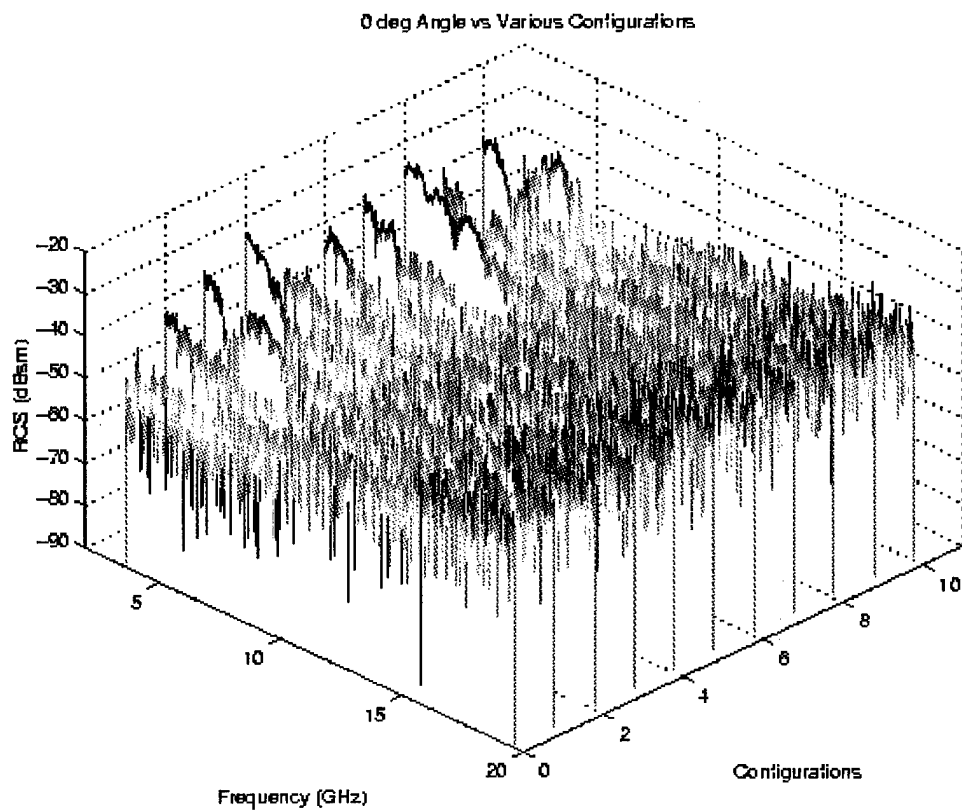


Figure C-1 Waterfall plot of the Various Configurations for 0 degrees

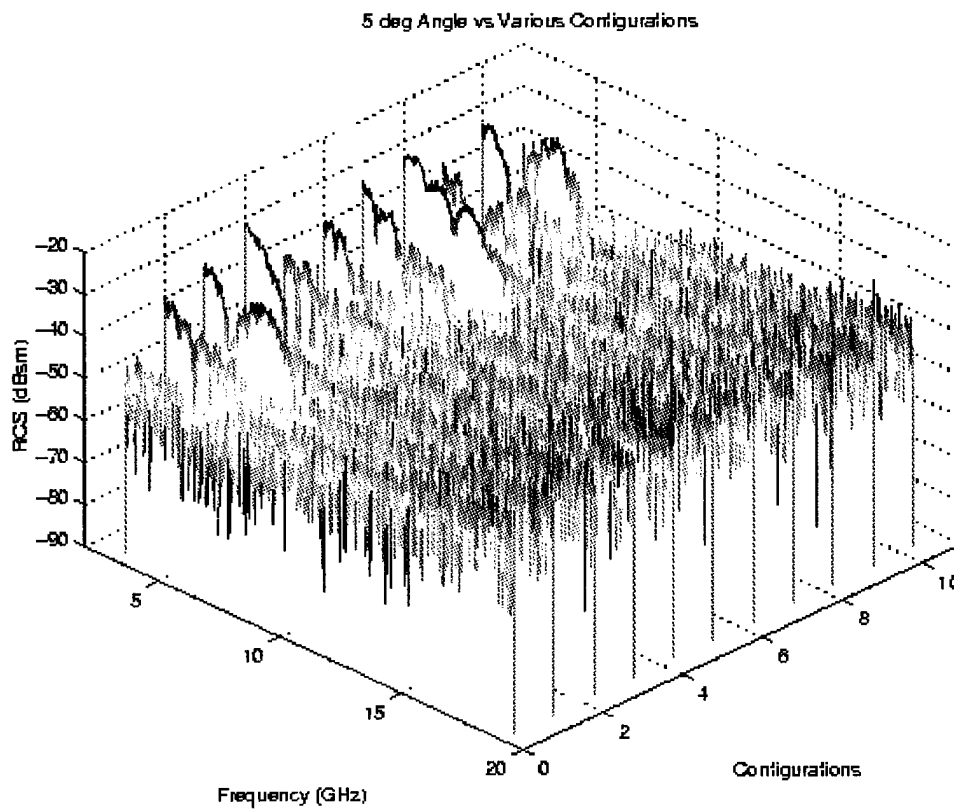


Figure C-2 Waterfall plot of the Various Configurations for 5 degrees

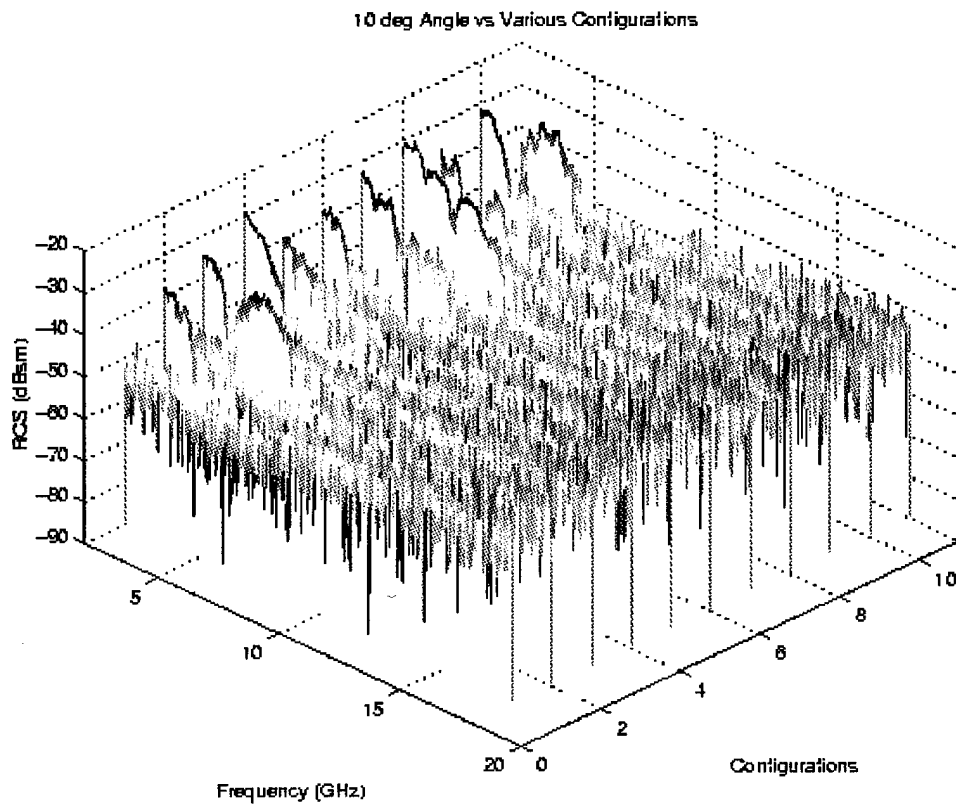


Figure C-3 Waterfall plot of the Various Configurations for 10 degrees

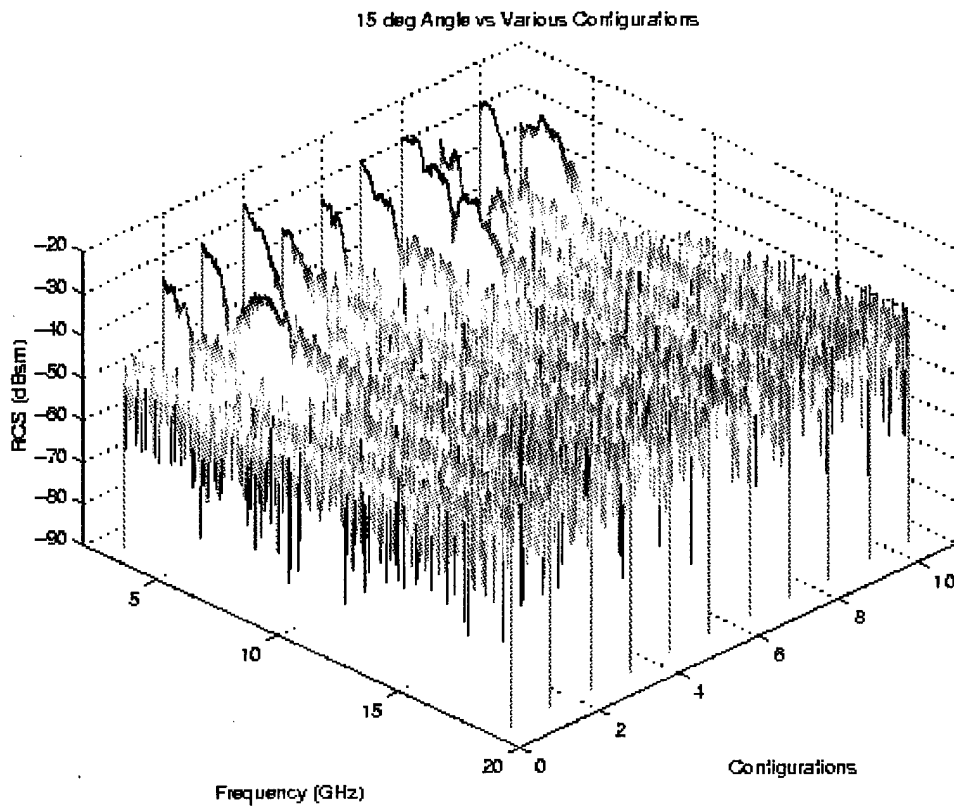


Figure C-4 Waterfall plot of the Various Configurations for 15 degrees

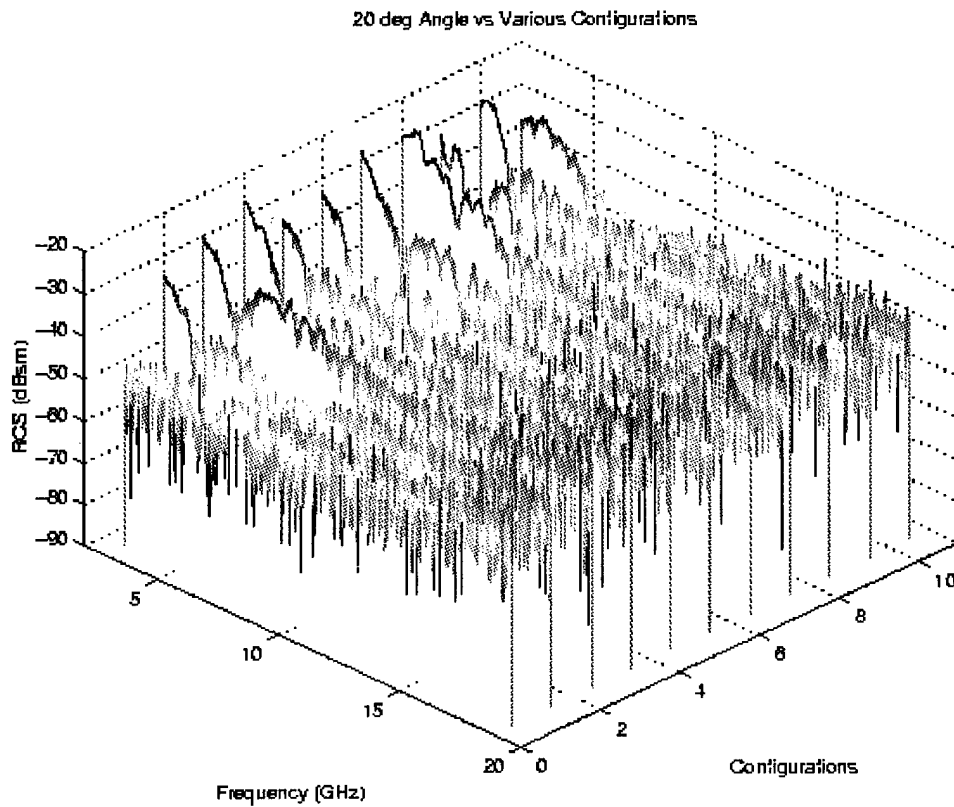


Figure C-5 Waterfall plot of the Various Configurations for 20 degrees

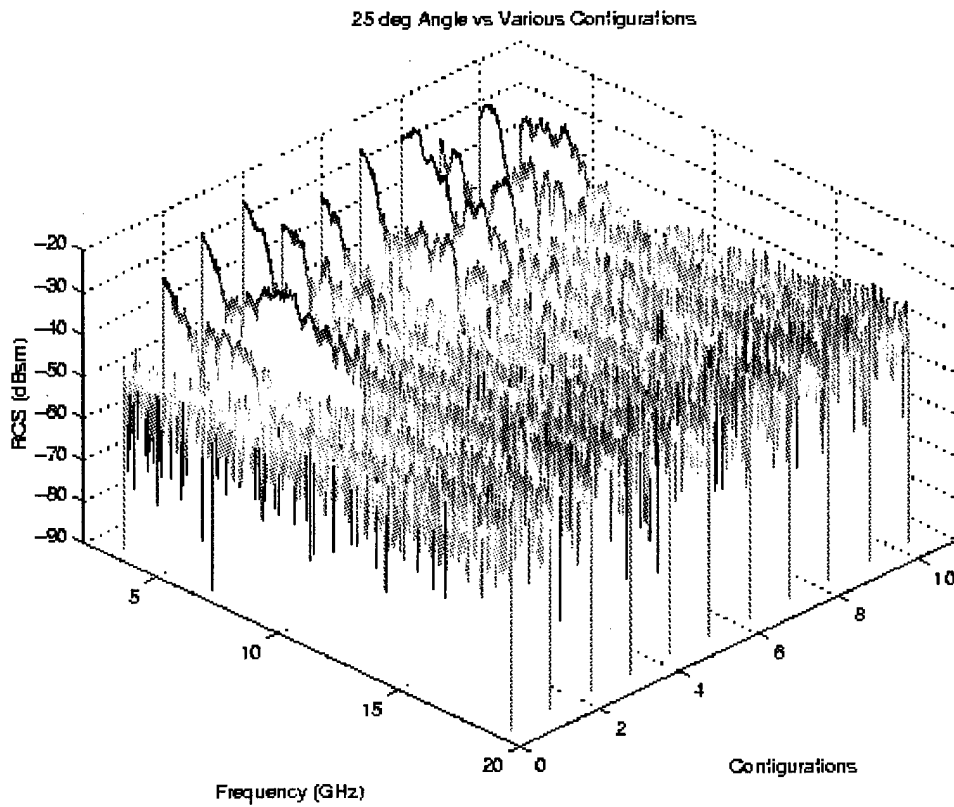


Figure C-6 Waterfall plot of the Various Configurations for 25 degrees

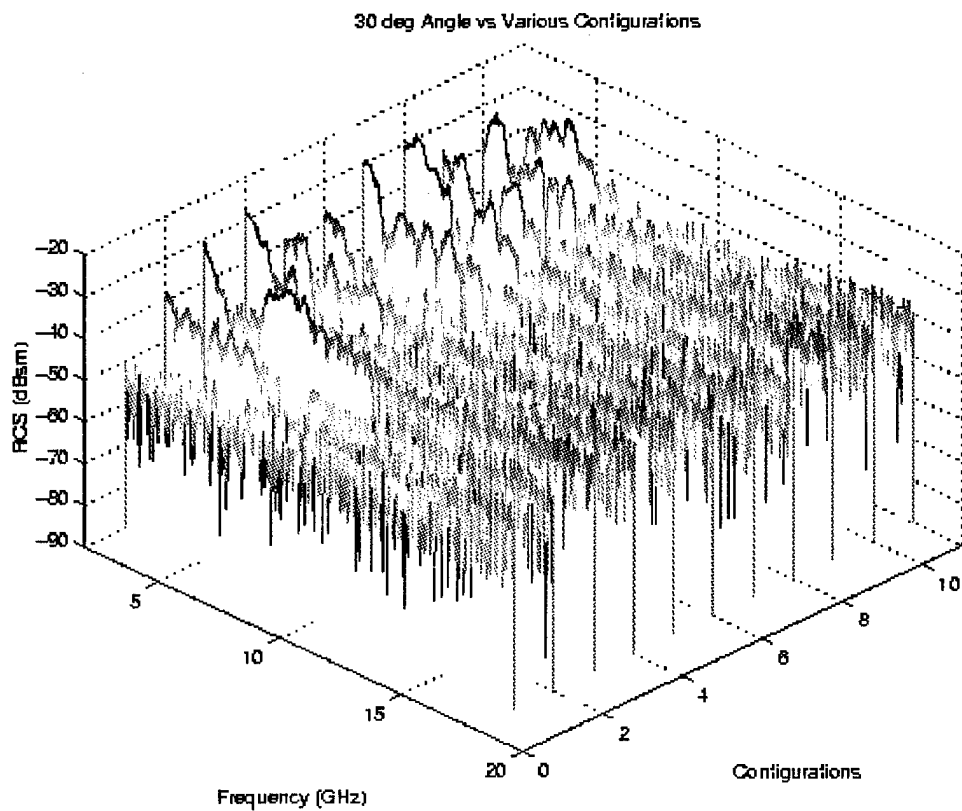


Figure C-7 Waterfall plot of the Various Configurations for 30 degrees

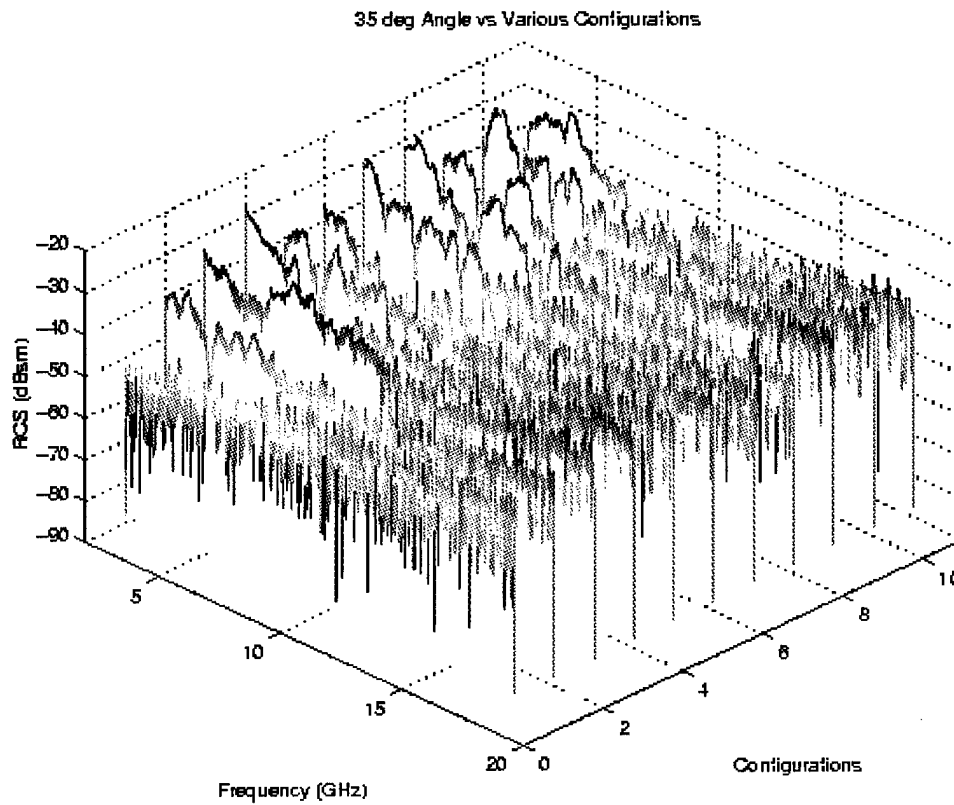


Figure C-8 Waterfall plot of the Various Configurations for 35 degrees

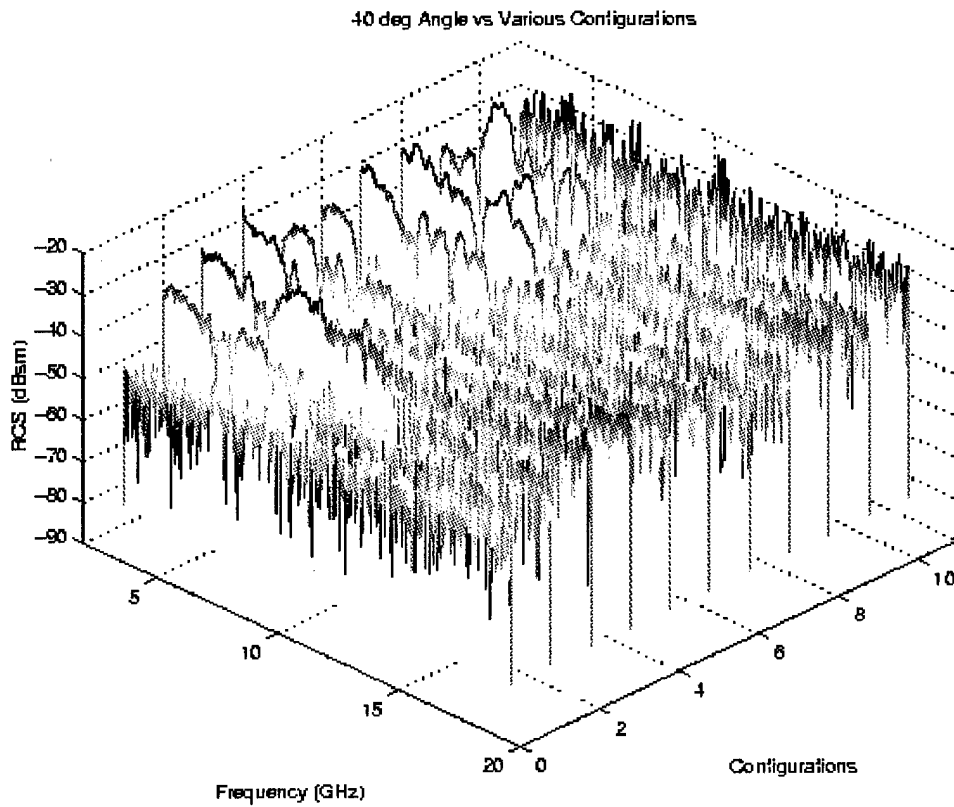


Figure C-9 Waterfall plot of the Various Configurations for 40 degrees

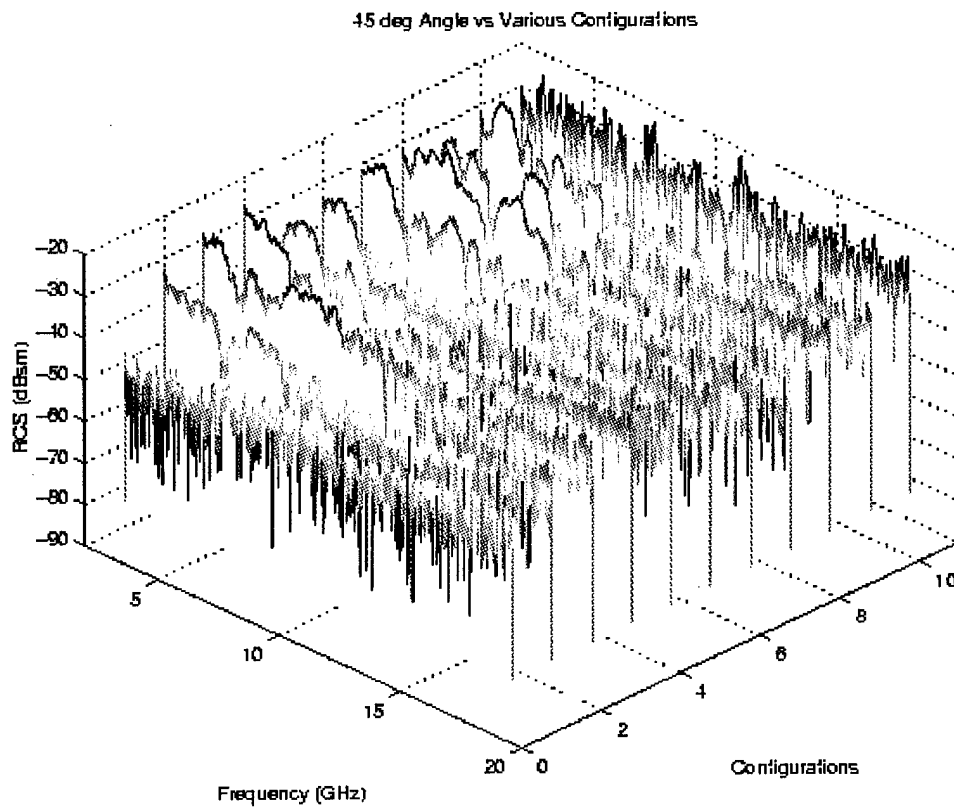


Figure C-10 Waterfall plot of the Various Configurations for 45 degrees

Bibliography

1. Senior, T.B.A. and J.L. Volakis. "Scattering by Cracks and Gaps," *IEEE Transactions on Antennas and Propagation*, 37:1102-1110 (June 1989).
2. Senior, T.B.A., K. Sarabandi and J.R. Natzke. "Scattering by a Narrow Gap," *IEEE Transactions on Antennas and Propagation*, 38:744-750 (July 1990).
3. Dominek, A.K., H.T. Shamansky and N. Wang. "Scattering from Three Dimensional Cracks," *IEEE Transactions on Antennas and Propagation*, 37:586-591 (May 1989).
4. Moore, J. and H. Ling. "Scattering by Gaps in Coated Structures," *Journal of Electromagnetic Waves and Applications*, 7:325-344 (July 1993).
5. Ling, H., J. Moore, D. Bouche and V. Saavedra. "Time-Frequency Analysis of Backscattered Data from a Coated Strip with a Gap," *IEEE Transactions on Antennas and Propagation*, 41:1147-1150 (August 1993).
6. Dominek, A., A. Park, and L. Peters, Jr. Material Parameter Determination from Scattering Measurements: Technical Report No. 719300-3. Grant No. NAG3-784. Cleveland OH: NASA Lewis Research Center, September 1988 (NASA-CR-183312).
7. Ryan, Patricia A. *TE Scattering From Short Bumps*. MS thesis, The Ohio State University, Columbus, OH, 1987.
8. Sweetman, Bill. *Stealth Aircraft*. Osceola, WI: Motorbooks International Publishers & Wholesalers, Inc., 1986.
9. Knott, Eugene F., et al. *Radar Cross Section*. Norwood, MA: Artech House, Inc., 1993.
10. Shultz, John. "Focused Beam Measurement System Users Manual." Unpublished Report. AFRL/XPN, Wright-Patterson AFB OH, 1998.
11. Afsar, M.N., J.R. Birch, and R.N. Clarke. "The Measurement of the Properties of Materials," *Proceedings of the IEEE*, 74:183-199 (January 1986).
12. Jay, F., (editor in chief), *IEEE Standard Dictionary of Electrical and Electronics Terms*. IEEE press, New York, NY, 1984.
13. Collins, Maj., Peter J. Class notes distributed in EENG 627: RCS Analysis, Measurement, and Reduction. Graduate School of Engineering, Air Force Institute of Technology, Wright-Patterson AFB OH, June 1998.
14. Mensa, Dean L. *High Resolution Radar RCS Imaging*. Artech House, Inc., Boston, MA, 1991

15. Gillespie, Andrew M. *The Limits of Validating Weapon System Absolute RCS Compliance Through the use of RCS Imaging Techniques*. MS thesis, AFIT/GE/ENG/93D-08, Air Force Institute of Technology, Wright-Patterson AFB OH, 1993.
16. Montgomery, Douglas C. and Elizabeth A. Peck. *Introduction to Linear Regression Analysis*. New York, NY: John Wiley & Sons, Inc., 1982.
17. Rogers, J. JRMBOR User's Guide: Technical Report JR-6. Greenbelt MD: Atlantic Aerospace Electronics Corporation, May 1997.
18. Lee, S.W. XpatchF User's Guide Volume 4 of 6. Champaign Ill: DEMACO, Inc., 1997.
19. Parks, Jeffrey M. *Scattering from Dielectric Bodies*. MS thesis, AFIT/ENG/GE/97D-13, Air Force Institute of Technology, Wright-Patterson AFB OH, 1997.
20. Chizever, Hirsh M., et al. "On Reducing Primary Calibration Errors in Radar Cross Section Measurements." *Antenna Measurements Techniques Association Symposium Proceedings*. 383-388. 1996.
21. Skolnik, Merrill I. *Introduction to Radar Systems*. New York, NY: McGraw-Hill, Inc., 1980.

Vita

Captain John Grayson Cochran was born December 16, 1970 in Spartanburg, S.C. He graduated from T.L. Hanna High School in Anderson S.C. in May 1989 and entered Georgia Tech in September 1989 on an AFROTC scholarship. In January 1990 he was initiated into Kappa Sigma. In December 1993 he finally "got out" of Georgia Tech with a Bachelor's Degree in Electrical Engineering (B.E.E). In March 1994 he entered active duty as a Second Lieutenant at Patrick AFB, FL. While at Patrick AFB he was assigned to the Air Force Technical Applications Center (AFTAC). His first job at AFTAC was as a Subsurface Project Engineer in the Logistics Directorate. Then in February 1996 he moved to the Plans and Programs Directorate where he was the Deputy Chief of the Programs Branch. In August 1997 he entered the Air Force Institute of Technology (AFIT) at Wright-Patterson AFB, OH to pursue a Master's Degree in Electrical Engineering. His follow on assignment is with the 46th Test Group, Radar Target Scattering Division (RATSCAT) at Holloman AFB, NM.

Permanent Address: 1200 Hanover Rd
Anderson, SC 29621

Appendix A

This appendix is a compilation of the 3-D image plots for each configuration. The 3-D image plots identify scattering centers relative to downrange and crossrange.

REPORT DOCUMENTATION PAGE			Form Approved OMB No. 0704-0188	
Public reporting burden for this collection of information is estimated to average 1 hour per response, including the time for reviewing instructions, searching existing data sources, gathering and maintaining the data needed, and completing and reviewing the collection of information. Send comments regarding this burden estimate or any other aspect of this collection of information, including suggestions for reducing this burden, to Washington Headquarters Services, Directorate for Information Operations and Reports, 1215 Jefferson Davis Highway, Suite 1204, Arlington, VA 22202-4302, and to the Office of Management and Budget, Paperwork Reduction Project (0704-0188), Washington, DC 20503.				
1. AGENCY USE ONLY (Leave blank)		2. REPORT DATE March 1999		3. REPORT TYPE AND DATES COVERED Masters Thesis
4. TITLE AND SUBTITLE TE Scattering From Bubbles in RAM			5. FUNDING NUMBERS	
6. AUTHOR(S) John G. Cochran, Captain, USAF				
7. PERFORMING ORGANIZATION NAME(S) AND ADDRESS(ES) Air Force Institute of Technology, WPAFB, OH, 45433			8. PERFORMING ORGANIZATION REPORT NUMBER	
9. SPONSORING/MONITORING AGENCY NAME(S) AND ADDRESS(ES) Mr. Enrique Mendez (ASC/ENAD) 2530 Loop Road West WPAFB, OH, 45433 937-255-8941			10. SPONSORING/MONITORING AGENCY REPORT NUMBER	
11. SUPPLEMENTARY NOTES Maj Peter Collins, 927-255-6565-4304				
12a. DISTRIBUTION AVAILABILITY STATEMENT Distribution Unlimited			12b. DISTRIBUTION CODE	
13. ABSTRACT (Maximum 200 words) This research looks at various bubble sizes in one particular magnetic RAM (MAGRAM) type, from grazing incidence (0°) to 45° and at a frequency range from 2-18 GHz, TE polarization. The results from the absolute RCS measurement of the various sized RAM bubbles are discussed in terms of a frequency dependent increase in RCS. In the frequency band of interest, 2 -18GHz, a RAM bubble increases the RCS at all angles, from grazing incidence (0°) to 45°. From 10 -18GHz the RAM bubble does not cause an increase in RCS. In general the highest RCS is at 2GHz and tapers down as frequency increases. At near grazing angles the RCS increase due to the bubbles is 10-15dB. At the higher angles, the RCS increase due to the bubbles is 10-20dB. The RCS increase is relative to the noise plus clutter measurement of the range. The range of absolute RCS values for the various bubble sizes can range from -55 dBsm to -25 dBsm. The results of these experiments are captured in a statistical model which provides an estimate of the bubble's dependence on frequency, angle, and size.				
14. SUBJECT TERMS Radar Cross Section, Radar Absorbing Material, TE Scattering, Bubbles			15. NUMBER OF PAGES 145	
			16. PRICE CODE	
17. SECURITY CLASSIFICATION OF REPORT UNCLASSIFIED	18. SECURITY CLASSIFICATION OF THIS PAGE UNCLASSIFIED	19. SECURITY CLASSIFICATION OF ABSTRACT UNCLASSIFIED	20. LIMITATION OF ABSTRACT UL	